Nucleation of recrystallization at selected sites in deformed fcc metals

Xu, Chaoling

Link to article, DOI:
10.11581/DTU:00000019

Publication date:
2016

Document Version
Publisher's PDF, also known as Version of record

Nucleation of Recrystallization at Selected Sites in Deformed fcc Metals

DTU Vindenergi
PhD Rapport 2017

Chaoling Xu

DTU Wind Energy PhD-0073 (EN)

December 2016

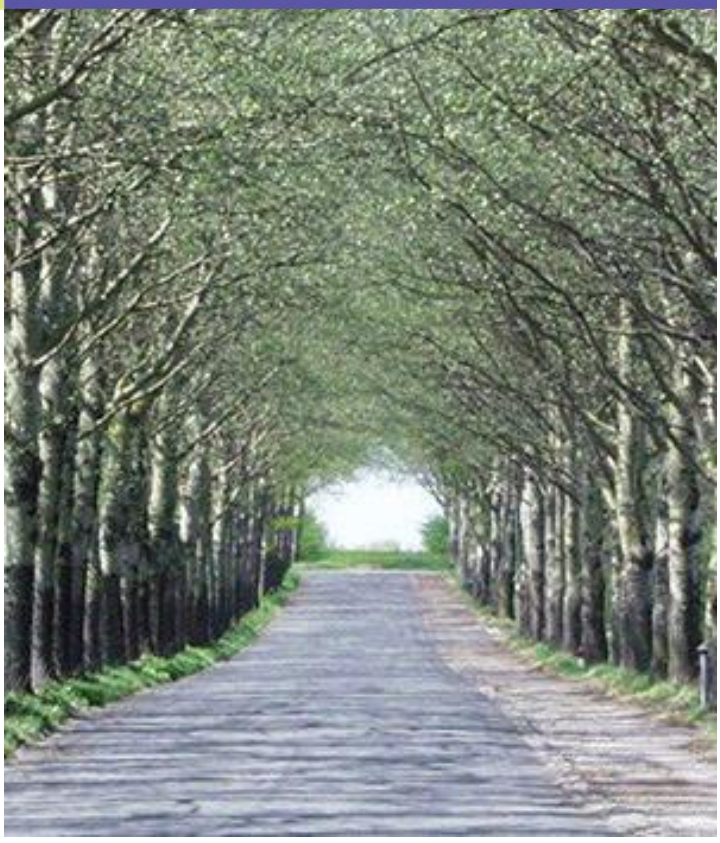

DTU Vindenergi
Institut for Vindenergi

Author: Chaoling Xu

Title: Nucleation of Recrystallization at Selected Sites in fcc Metals

Institute: Department of Wind Energy

Abstract:

The objective of this thesis is to explore nucleation of recrystallization at selected sites in selected face-centered-cubic (FCC) metals, namely cold rolled columnar-grained nickel and high purity aluminum further deformed by indenting. Various techniques, including, optical microscopy, electron backscattered diffraction (EBSD), electron channeling contrast (ECC) and synchrotron X-ray technique, differential-aperture X-ray microscopy (DAXM), were used to characterize the microstructures, to explore nucleation sites, orientation relationships between nuclei and deformed microstructures, and nucleation mechanisms.

In the cold rolled nickel samples, the preference of triple junctions (TJs) and grain boundaries (GBs) as nucleation sites is observed. The majorities of the nuclei have the same orientations as the surrounding matrix or are twin-related to a surrounding deformed grain. Only a few nuclei are observed with orientations different from the surrounding matrix. Hardness measurements at TJs in the deformed sample indicate a weak correlation between the difference in hardness among the three grains at the TJs and the potentials of the junctions to form nuclei: the higher the difference, the more likely is nucleation.

In the weakly rolled and indented aluminum samples, it is found that hardness indentations lead to large orientation rotations near indentation tips. In initial grains of different crystallographic orientations, the grains with higher stored energy (SE) in the rolled microstructures have higher average hardness values and higher nucleation probabilities. In general, indentations with higher hardness values have higher nucleation potentials. The orientations of the nuclei from different indentations in a given grain are observed not to be randomly distributed, but clustered in limited orientation spaces. The orientation spread observed near the indentation tips in the deformed state covers the orientations of the nuclei observed in the annealed state.

Whereas the above results are obtained by the EBSD technique and thus are 2D observation, the nucleation at hardness indentations is also investigated non-destructively by the DAXM technique. By first characterizing the deformation microstructure within a selected gauge volume near a hardness indentation, then annealing the sample and measuring the same volume again, nucleation is directly correlated to the deformation microstructures in the bulk of the sample. It is found that the nuclei evolve from embryonic volumes at areas of high SE below the surface and develop because of an advantage of fast migrating boundaries surrounding the initial embryonic volumes. All nuclei have crystallographic orientations as those present within the embryonic volumes in the deformed state. It is further suggested that boundaries between nuclei and the deformed matrix of less than 5° hinder subsequent growth of the nuclei.

For all the observed cases, it is suggested that the nucleation mechanism may be strain induced boundary migration (SIBM), but the boundaries are not those conventionally considered, namely original grain boundaries, but are strain induced dislocation boundaries.

DTU Wind Energy PhD-0073

December 2016

Project period:

2014.01-2016.12

Education:

Doctor of Philosophy

Supervisors:

Dorte Juul Jensen

Yubin Zhang

Qing Liu

Guilin Wu

Sponsorship:

Danish National Research Foundation

Chinese Scholarship Council

Pages: 128

References: 154

Danmarks Tekniske Universitet
DTU Vindenergi
Nils Koppels Allé
Bygning 403
2800 Kgs. Lyngby

www.vindenergi.dtu.dk

Nucleation of Recrystallization at Selected Sites in Deformed fcc Metals

Chaoling Xu

Supervised by Dorte Juul Jensen, Yubin Zhang,

Qing Liu and Guilin Wu

Materials Science and Advanced Characterization Section

Department of Wind Energy

Technical University of Denmark

December 2016

Contents

Preface

This thesis is submitted in partial fulfillment of the requirements for the PhD degree at the Technical University of Denmark (DTU). The project was a joint-degree PhD project of DTU and Chongqing University (CQU), and was carried out within the section for Materials Science and Advanced Characterization (MAC), Department of Wind Energy, DTU, and within the College of Materials Science and Engineering, CQU, under the supervision of Professor Dorte Juul Jensen, Dr. Yubin Zhang, Professor Qing Liu and Dr. Guilin Wu.

I am grateful to my supervisors Dorte Juul Jensen, Qing Liu, Yubin Zhang and Guilin Wu, who were instructing, enlightening, encouraging and providing me with constant support and many useful discussions. I would like to thank Professors Xiaoxu Huang, Andy Godfrey, Drs. Fengxiang Lin, Xuehao Zheng for inspiring discussions. Lars Lorentzen, Preben Olesen, Steen Bang, Gitte Christiansen and Ove Rasmussen are acknowledged for their skillful work preparing samples and more. I am thankful to Helle Hemmingsen, who helped me with plenty of office matters. I would also like to thank Drs. Niels Hansen, Oleg Mishin, Tianbo Yu, Chuanshi Hong, Søren Fæster, Xiaodan Zhang, Linus Daniel Leonhard Duchstein, and all the other colleagues at DTU and at Chongqing University who have helped me a lot.

The differential-aperture X-ray microscopy experiment was carried out at the Advanced Photo Source, Argonne National Laboratory, USA. I am grateful to Drs Jonathan Tischler, Wenjun Liu and Ruqing Xu at the beamline 34-ID-E.

Finally, I would like to thank my family and my boyfriend, Jun Sun, for supporting me throughout the years.

List of publications

A. **Xu, C. L.**, Huang, S., Zhang, Y. B., Wu, G. L., Liu, Q. & Juul Jensen, D. 2015 Orientations of recrystallization nuclei developed in columnar-grained Ni at triple junctions. *17th International Conference on Textures of Materials, IOP Conf. Ser. Mater. Sci. Eng.,* **82,** 012044.

B. **Xu, C. L.**, Zhang, Y. B., Wu, G. L., Liu, Q. & Juul Jensen, D. 2015 Nucleation at hardness indentations in cold rolled Al. *36th Risø Symposium on effects of deformation induced structural variations on annealing mechanisms, IOP Conf. Ser. Mater. Sci. Eng.,* **89,** 012054.

C. **Xu, C. L.**, Zhang, Y. B., Lin, F. X., Wu, G. L., Liu, Q. & Juul Jensen, D. 2016 Crystallographic analysis of nucleation at hardness indentations in high purity aluminum. *Metal. Mater. Trans. A,* 47, 5863-5870.

D. **Xu, C. L.**, Zhang, Y. B., Godfrey A., Wu, G. L., Liu, W. J., Tischler, J. Z., Liu, Q. & Juul Jensen, D. 2016 Direct observation of nucleation in the bulk of an opaque sample. *Sci. Rep.* 7, 42508; doi:10.1038/srep42508.

Chapter 1
Introduction

When metals are plastically deformed, point defects and dislocations are introduced and stored in the material. The content of defects and thus the stored energy (SE) is reduced by annealing. The basic processes taking place during the annealing of deformed metals are recovery, recrystallization and grain growth.

Recrystallization is practically used in almost all metal forming processes. During recrystallization both the microstructure and texture change significantly, and the deformed metals' properties can be optimized. The mechanical properties of metals such as strength, ductility, fatigue, corrosion and formability, are strongly dependent on the microstructures. A solid understanding of microstructures, for example, how they evolve during annealing, is very important for the design of materials with desired mechanical properties.

Recrystallization of deformed metals is a process, during which new, small and almost strain-free grains, termed nuclei, form and grow into the deformed matrix by boundary migration until the entire matrix is replaced by the new grains [1]. The driving force for recrystallization is the energy stored in the deformed matrix [2, 3]. The formation process of nuclei in the deformation microstructures is termed nucleation, which is of central importance for the microstructural evolution, as the orientations and nucleation sites to a large extend determine the grain sizes, grain shapes and textures of the fully recrystallized microstructure.

One of the key questions in understanding nucleation is: what orientations do the nuclei form with? This is critical for recrystallization modeling in which proper nucleation mechanisms are rarely included and it is generally assumed that the nuclei have random orientations or orientations as those in the

deformed microstructures [4]. This is because accepted nucleation theories propose that the orientations of the nuclei must already be present in the deformed state before annealing. The nuclei could form by mechanisms such as strain induced boundary migration (SIBM) [5, 6], subgrain growth [7, 9] and subgrain coalescence [10, 11]. Indeed, the nucleation of grains with orientations within the spread of the deformed matrix is commonly observed [3]. Recently, however, several publications have reported observations of nuclei with orientations different from the orientations in the deformed matrix from which they originated [12, 13], which conflicts with the classical nucleation mechanisms.

It is, well documented that original grain boundaries (GBs), triple junctions (TJs) are preferential nucleation sites [14] and the nucleation mechanism here may be SIBM [5, 6]. However, it is still difficult to know where exactly the nuclei will form on the long GBs or at which of those TJs [14]. Large second phase particles are also known to stimulate nucleation [15, 16], but difficulties here are that not all the particles stimulate nucleation and it is not known which one will stimulate nucleation [17, 18]. Additionally, scratches and hardness indentations are known to stimulate nucleation, which is usually in an uncontrolled manner, particularly for scratches [19, 20].

Nucleation is difficult to study as nuclei are small and few. To find a nucleus is thus like a ‘find the needle in the haystack problem’. A big problem when studying nucleation is thus the lack of suitable experimental techniques. Nuclei form in a so-far unpredictable way at sites in the bulk away from sample surfaces, and their formation can thus not be observed directly in-situ by light or electron microscopy. Static, ‘after the fact’ observations on the other hand, do not help to pinpoint nucleation mechanisms, as the deformed matrix leading to nucleation is consumed — a problem often referred to as that of ‘lost evidence’ [21].

In the present work, samples are chosen with some control of potential nucleation sites, namely cold rolled columnar-grained nickel and lightly cold

rolled aluminum further deformed locally by hardness indentations. The focus will be on where and how the nuclei form in the deformed microstructures and with what orientations. The columnar-grained nickel samples where the columnar grains extend through the entire sample thickness with no hidden grains underneath the surfaces are chosen to avoid nucleation from 'below-the-surface deformed grains'. Additionally, several nominally identical specimens can be obtained, i.e. the same condition can be studied for several sub-samples, which facilitates finding potential nucleation sites by ex-situ experiments. The indentations in aluminum are chosen to emphasize the control over the sample volume in which nucleation is expected to occur, and thus to facilitate ex-situ bulk experiments. Aluminum is chosen to avoid an excessive number of annealing twins that would complicate the analysis of the nucleation mechanism. Other important reasons for choosing columnar nickel and indented aluminum for the present work are that they are of industrial interest and that a great deal of information has already been obtained on their deformation microstructures [22-24].

In the present work, not only 2D characterization methods, such as electron backscattered diffraction (EBSD) and electron channeling contrast (ECC), but also a 4D (x, y, z plus time) characterization method, differential-aperture X-ray microscopy (DAXM) [25] is used for studying nucleation in the opaque sample.

The aim of the present work is to advance the current understanding of nucleation of recrystallization. This ambitious goal is approached by ① choosing model samples for which some knowledge exists on potential nucleation sites, ② using a wide range of characterization techniques including 2D and 3D [25] that incorporate both ex-situ and in-situ measurements, as well as ③ relating to the deformation microstructures that can lead to nucleation at the preferential nucleation sites in the present samples.

The results will provide answers to the fundamental questions on active nucleation sites leading to viable nuclei which can grow during further annealing. The results have important implications for modeling nucleation of

recrystallization [26-28], for hardness indentation dislocation theories [24, 29] and for understanding dislocation interactions [30] that occur when an embryonic volume becomes a nucleus.

This chapter provides the theoretical and experimental background for the present study. A brief introduction of deformation microstructures is first given, focusing on the deformation microstructures in which nucleation preferentially occur, such as GBs and TJs, regions near large second phase particles and hardness indentations. The deformation microstructures affect the process of recrystallization to a large extent. So this type of information is needed for interpreting nucleation and subsequent nuclei growth into deformed materials. Next, fundamental knowledge and a literature review related to nucleation are introduced, including classical nucleation theories, the theory of oriented nucleation, the prevalence of GBs, particles and hardness indentations as nucleation sites. Finally, the overall layout of the thesis is given.

1.1 Deformation microstructures

During cold deformation processes, a large fraction of the work is released as heat and about 10% is retained as energy stored inside the metal [31]. Metals with medium-to-high stacking fault energies, such as aluminum, copper, nickel and α-iron, deform mainly by slip [32, 35]. The number and selection of simultaneously active slip systems may be different in neighboring volume elements of individual grains [32, 33]. Any volume element can deform relatively homogeneously on less than the five slip systems [34, 35] required by Taylor model [36], while a group of volume elements may collectively fulfill the Taylor criterion.

1.1.1 The evolution of deformation microstructures

At low strains, the microstructure in cell forming metals develops with increasing strain from a tangled dislocation structure to a structure consisting of equiaxed cells separated by incidental dislocation boundaries (IDBs) (see (a)-(d) in figure 1.1) [35, 37-42]. The cells are organized into cell blocks delineated by geometrically necessary boundaries (GNBs) (see A-H in figure 1.1) including

dense dislocation walls (DDWs), microbands and cell-band walls. GNBs can accommodate the lattice misorientations between cell blocks resulting from different active slip systems in neighboring volume elements [43]. The misorientations across GNBs are higher than the misorientations across IDBs.

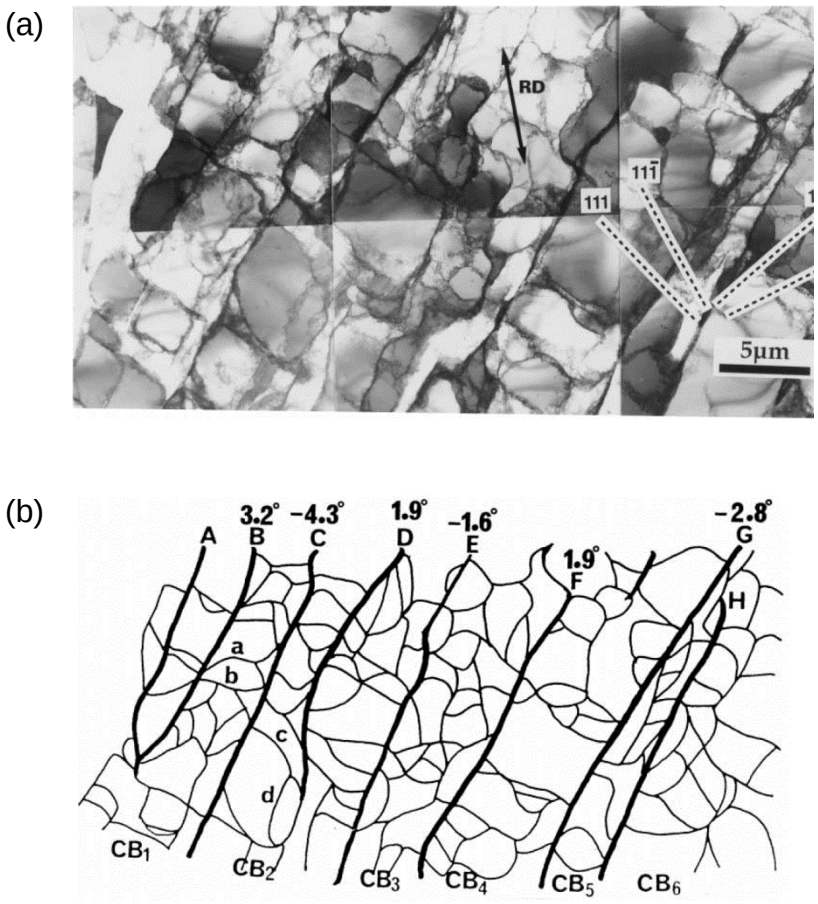

Figure 1.1: (a) Transmission electron microscopy (TEM) image of a cell-block structure in a grain of 10% cold-rolled aluminum (99.996% purity) viewed in the longitudinal plane, where RD is the rolling direction. One set of non-crystallographic geometrically necessary boundaries (GNBs) is formed in the grain. (b) A sketch of the same area showing the traces of boundaries and the misorientation angles between adjacent cell blocks (CBs). Cell block boundaries are marked as A, B, C, *etc.* and cell boundaries are marked as a, b, c, and d. Reproduced from [47].

At low-to-medium strains, most of GNBs have a macroscopic orientation with an angle between 25° and 55° to the rolling direction (RD) in the longitudinal plane [37, 44, 46]. With increasing strain, the cell block structure evolves. Note

that the sizes of the cell blocks and of the cells decrease and the spacings of GNBs also decrease (see table 1.1) [47]. The misorientations across the boundaries increase with increasing strain (see figure 1.2) [48].

At large strains, the GNBs become more closely aligned with the rolling plane and the boundary spacing of GNBs still decreases with the increase of strain [37, 45, 49]. As to the misorientation angles for both GNBs and IDBs, the trend is a continuous increase with increasing strain, as shown in table 1.1.

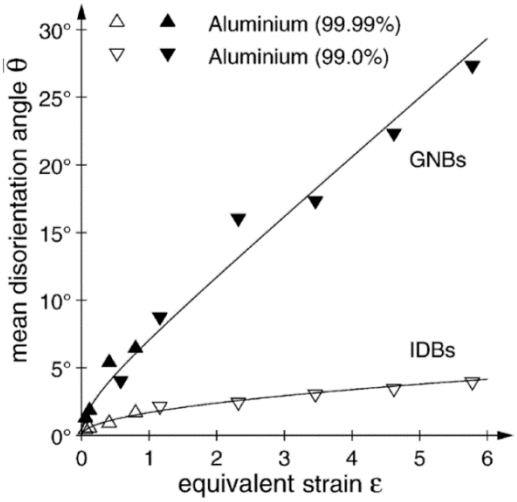

Figure 1.2: Evolution of the average misorientation angle across different types of boundaries (IDBs and GNBs) in aluminum during cold rolling. The triangles are the measured data in [50] and the full lines are fits of Eq. (12) in [48] to the experimental data from [50] for aluminum of two different purities (99.99%, 99.0%). Reproduced from [48].

Table 1.1: Average values of microstructural parameters as a function of strain for commercial purity aluminum (AA 1200). Reproduced from [51].

True thickness strain	Reduction %	Von Mises strain	Misorientation angle (Deg.)		Boundary spacing (μm)	
			IDBs	GNBs	IDBs	GNBs
1.0	63.2	1.16	2.1	8.7	Approx. 1.0	0.60
2.0	86.4	2.32	2.4	16.0		0.43
3.0	95.0	3.46	3.0	17.3		0.37
4.0	98.2	4.62	3.4	22.3		0.33
5.0	99.3	5.78	3.9	27.3		0.30

The arrangement of dislocations tends to approach the lowest possible energy per unit length of dislocation line and form low energy dislocation structure (LEDS), in which neighboring dislocations screen each other's stress fields such that the total dislocation energy density W is

$$W = \rho \frac{Gb^2 f(v)}{4\pi} ln \frac{R}{b} \tag{1.1}$$

where G, v and b are the shear modulus, the Poisson's ratio and the Burgers vector, respectively [52]. $f(v)$ is related to dislocation types, edge dislocations and screw dislocations, and it approximately equals $(1 - v/2)/(1 - v)$ [53]. *R* is approximately equal to the average dislocation spacing,

$$R \approx \frac{1}{\sqrt{\rho}} \tag{1.2}$$

where ρ is the dislocation density [54]. The energy of LEDS is smallest and the structure is most stable relative to other dislocation structures.

1.1.2 The orientation dependence of deformation microstructures

The evolution of deformation microstructures are related to the interaction of dislocations during plastic deformation. The grain orientation determines the selection of active slip systems and thus has a significant effect on the development of dislocation structures during plastic deformation. Therefore, there are correlations between crystallographic orientations and the microstructures. As the present investigation mainly deal with cold rolled aluminum, the deformation microstructure of cold rolled aluminum is in focus here and the following summarizes results from a previous investigation [47] (see figure 1.3):

Type A1: The grains are subdivided by long and straight GNBs on crystallographic {111} plane.

Type A2: The grains are subdivided as for Type A1, but the GNBs are less straight compared with those in type A1 so that the GNBs are roughly on {111} planes but with deviations of a few degrees.

Type B: The grains are subdivided by non-crystallographic GNBs which are not on {111} planes and are much more curved compared with type A1 and A2.

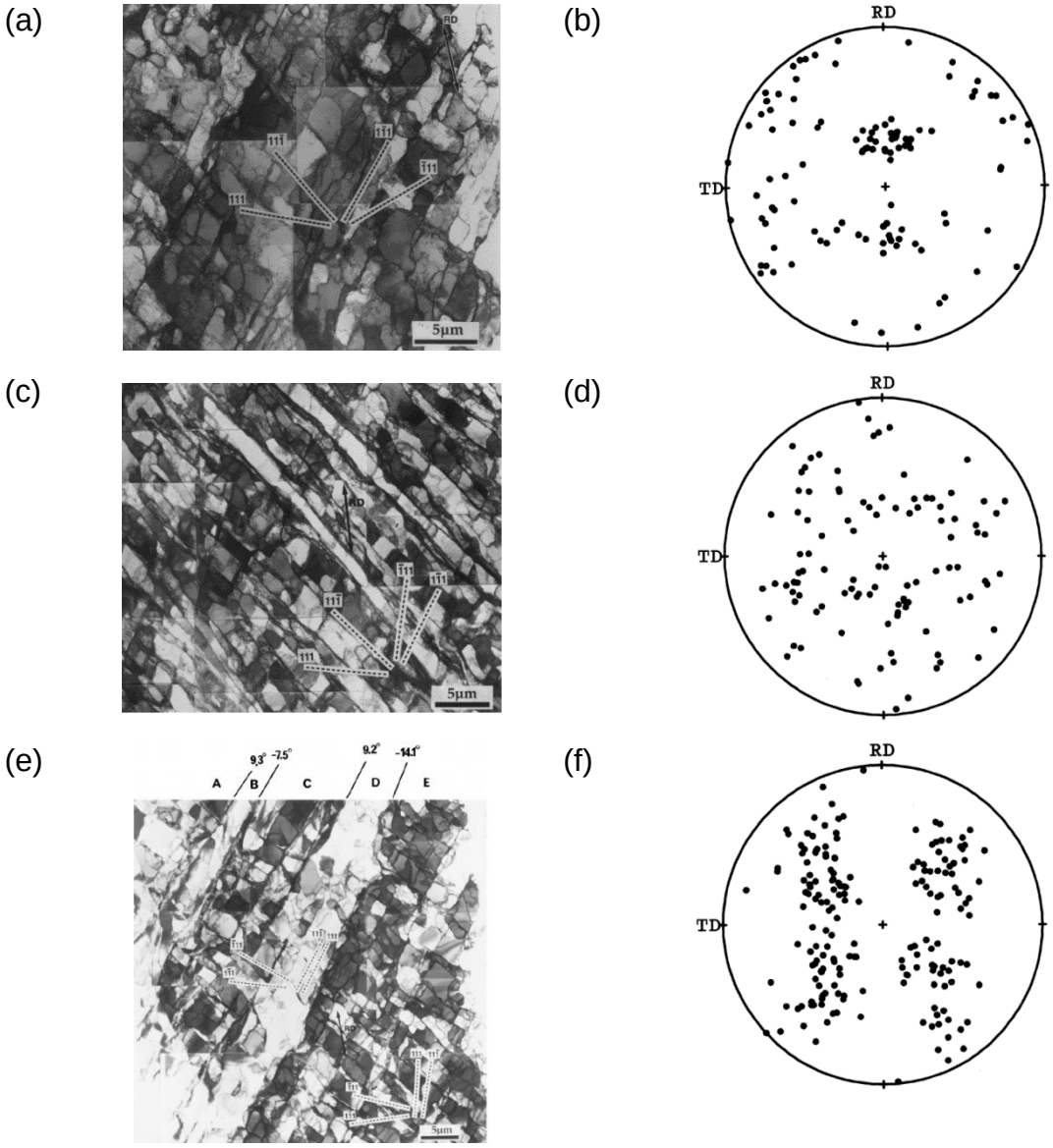

Figure 1.3: TEM images and {111} pole figures to show type A1 (a, b), type A2 (c, d) and type B (e, f) deformation microstructures in the longitudinal plane view and corresponding grain orientations in Al samples cold rolled to 30% reduction. In (a), two sets of geometrically necessary boundaries (GNBs) which are on (11-1) and (1-11) have developed. In (b), one set of GNBs, which is on (11-1) and less straight and uniform than that in (a), has developed. In (c), a complex cell block structure with non-crystallographic GNBs has developed, in which regions A, C and E have similar average orientations, and regions B and D have similar average orientations. Reproduced from [47].

1.1.3 Effects of GBs and TJs on deformation microstructures

As mentioned above, GBs and TJs influence the evolution of deformation microstructures. In most cases, the deformation microstructures, such as, cells and cell blocks, directly extend from the grain interior all the way to GBs and there is no obvious difference in the microstructure morphology between the interior and the GB region (e.g. [63-65]).

However, in some cases, the effects of GBs and TJs on deformation microstructures are pronounced, resulting in a difference in microstructure morphology near GBs and TJs from that in the grain interior. Such difference has been observed on surface relief microstructures by scanning electron microscopy (SEM) and optical microscopy, and on thin foil microstructures by transmission electron microscopy (TEM) near GBs (see figure 1.4) [66]. Local deformation patterns near GBs and TJs have also been investigated in terms of orientation perturbations (orientation variation as a function of distance from a GB) in cold rolled polycrystalline aluminum by Randle *et al.* [67]. In that investigation, it was found that considerable perturbations are present at TJs but not near GBs in samples deformed to 5% reduction, while more perturbations are at GBs in the samples deformed to 30% reduction [67]. In Al samples compressed to 40%, a complex deformation microstructure is observed at TJs, where the dislocation boundaries have much higher misorientation angles than those within the grain interior [68]. In cold rolled aluminum with grain sizes in the range of 20 μm to 400 μm, Bay [40] observed that lots of CBs exist near GBs and the size of cell blocks near GBs is smaller than within the grain interior, indicating that the strain and active slip systems near GBs and within grains are different. The results are in good agreement with Ralph and Hansen's observations [69] in tensile deformed fine-grained copper where the cell structures near GBs have a smaller average size and a wider variation in size than within the grain interior.

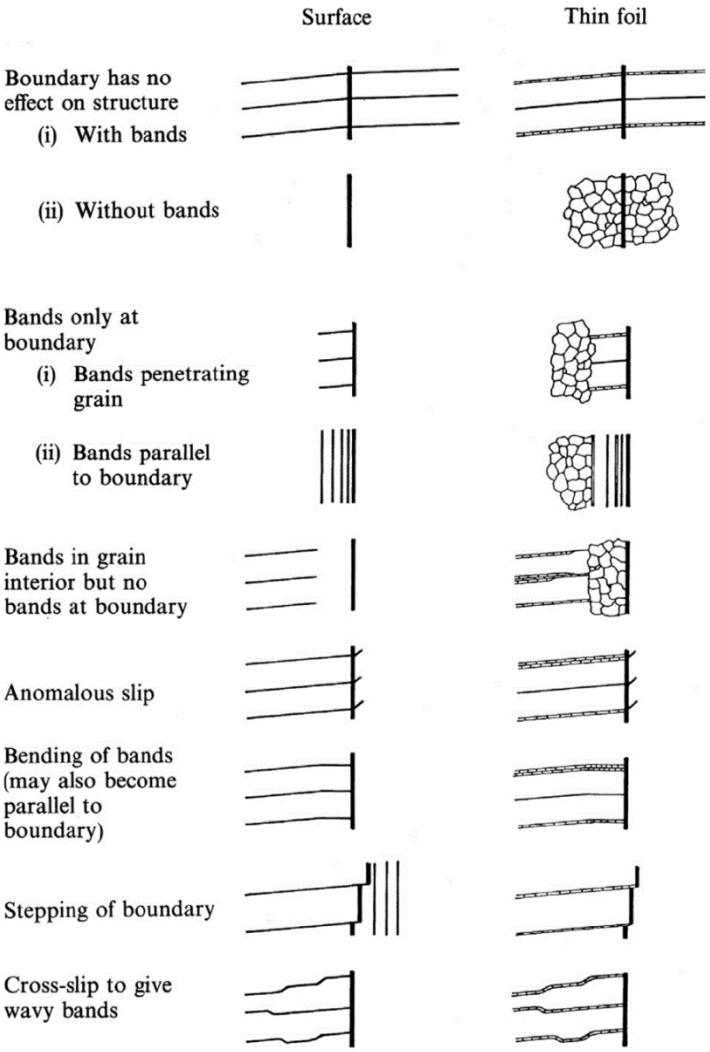

Figure 1.4: Classification of structures at grain boundaries in aluminum samples cold rolled to 15% reduction in thickness. The thick black lines represent the grain boundaries. The left column shows the surface structures observed by SEM or optical microscopy, while the right column displays the thin foil structures observed in TEM. Reproduced from [66].

1.1.4 Effects of second-phase particles on deformation microstructures

Second-phase particles are often present in metals and they affect the evolution of microstructure during deformation. If the particles are deformable, the shape and size of the particles changes during deformation [1]. Kamma and Hornbogen [70] found that Fe_3C particles in steel deformed, leading to the formation of shear bands at low strains, while at high strains, the bands broadened and slip became homogeneous. Nourbakhsh and Nutting [71] found

that in Al-Cu alloys containing large particles, the deformation was initially inhomogeneous as the particles deformed. At strains above 1, the particles disintegrated to give small particles, leading to a more homogeneous slip distribution.

If the particles are large and non-deformable, dislocations tend to tangle and accumulate at the particles (see figure 1.5) [72, 73]. It has been suggested that large non-deformable particles can cause a small portion of the crystal to rotate in a ‘wrong’ sense relative to the matrix and thus a local deformation zone with other orientation components forms around the particle [74, 75]. Investigations of tensile strained, rolled and compressed samples containing particles have shown similar results [74, 79]. The amount of rotation is dependent both on particle size and strain. As shown in figure 1.6, for particles of diameter less than 0.1 µm, local rotated zones near particles are generally not formed; at larger non-deformable particles, local lattice rotations occur at a strain above 0.08. For a given strain, the misorientation of the region close to the particles with respect to the matrix decreases with decreasing particle size [80]. The maximum rotation (θ_{max}) decreases with distance from the particle and is similar to that of the matrix at distances of the order of the particles diameter (see figure 1.7a) [80]. For a particle in the size range 0.5 to 2 µm, θ_{max} is a function of both strain and particle size, while θ_{max} is found to be a function of mainly strain for particles larger than 3 µm, as shown in figure 1.7b [80].

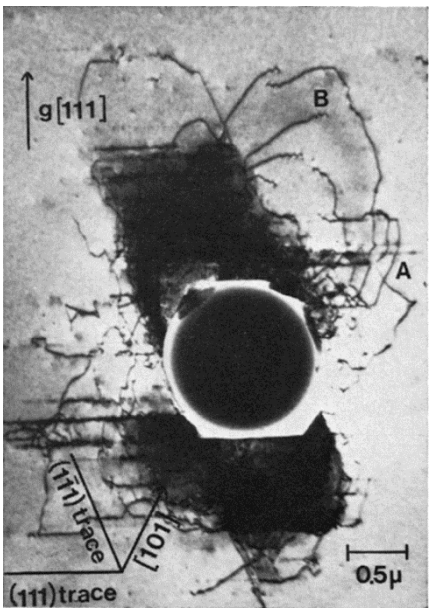

Figure 1.5: Deformation zones around a silica particle in a tensile strained Cu-20%Zn-SiO_2 crystal (ε= 0.16). Reproduced from [73].

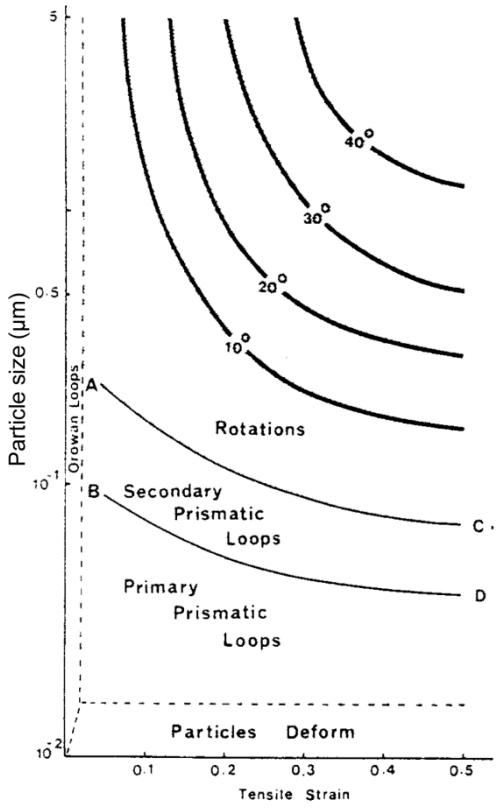

Figure 1.6: Semi-quantitative representation of the effect of strain and particle size on the deformation mechanisms around particles in particle containing aluminum crystals. Reproduced from [80].

(a) (b)

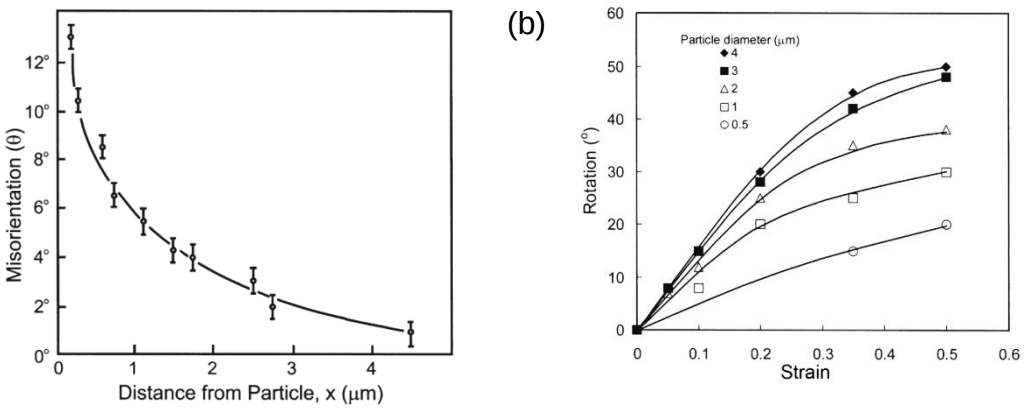

Figure 1.7: (a) Lattice misorientation at a 3 μm silicon particle in a tensile strained aluminum crystal (ε=0.1) as a function of distance from the interface; (b) the maximum misorientation at particles as a function of strain and particles size in particle-containing aluminum crystals. Reproduced from [80].

1.1.5 Deformation microstructures near hardness indentations

Hardness indentations are known to cause crystallographic lattice rotation and a high local dislocation density around the indentations. Fleck [81], Nix, Gao [82] and Swadener [83] have studied the indentation size effect for crystalline materials by connecting it with geometrically necessary dislocations. For an indenter with a smooth axisymmetric profile which applies for pyramidal and conical indenters, it is found that, at the position r away from the central axis of the indentation, the dislocation spacing can be expressed approximately as

$$s(r) = \frac{ab}{(a-r)tan\theta}, \tag{1.3}$$

where b is the Burger's vector, a is the contact radius and θ is the angle between the indenter and the surface [82]. This leads to the highest density of geometrically necessary dislocations at the center of the indent.

With EBSD technique, it is not possible to measure microstructures and orientation changes directly in the bulk underneath indentations but only at the rims of the indentations [84]. By combining SEM, focus ion beam (FIB) and EBSD techniques, the 3D microstructures underneath indentations have been characterized destructively [24, 29, 85, 88], from which the rotation patterns

around indentations are directly observed. The 3D microstructures show that the deformation and thus the geometrically necessary dislocation density peaks at the tip in agreement with equation (1.3) and changes in orientation are highly localized at the sides of the indentations and beneath the tips (see figure 1.8) [24, 85, 87].

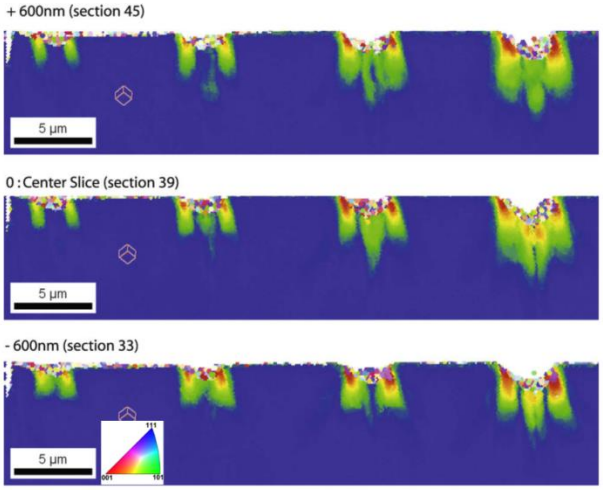

Figure 1.8: The orientation distribution below and around 4 indentations of different depth in a Cu single crystal, the center section and two equally distant outer sections. Color code: crystal axis along the direction of indentation. Reproduced from [86].

1.2 Recrystallization nucleation of deformed metals

By nucleation of recrystallization, small nearly perfect crystals form, and are then able to grow in at least one direction into the deformed materials [89]. Several nucleation mechanisms have been reported in literature, such as SIBM [5, 6], subgrain growth by boundary migration [7, 9] and coalescence [10, 11], which are summarized briefly in the following. It should be noted that in the present study, the areas surrounded by IDBs in deformation microstructures are named as cells, while the areas surrounded by LABs formed by polygonization during recovery are named as subgrains.

1.2.1 Strain induced boundary migration

The mechanism of SIBM was first found and proposed by Beck and Sperry in high purity aluminum [90]. The process of SIBM starts by bugling out of an original GB in the deformation microstructures. As shown in figure 1.9, the boundary migrates from position 1 to position 2 driven by the energy difference ΔE ($\Delta E = E_2 - E_1$, $E_1$and E_2 are the SEs of grain A and grain B respectively), resulting in a nearly strain-free region with an orientation almost identical with the orientation of the relevant part of the deformed grain A. The strain-free area is bounded by the original GB (the moving boundary) on one side and borders the deformed grain A on the other side. Thus SIBM may be considered as coarsening of a region already present in the deformed matrix. SIBM is observed to be a dominant recrystallization mechanism for reductions less than 20% [91]. Investigations of recrystallization of deformed metals with reductions above 20% (nickel, copper and silver) also suggest that the nucleation process occurred by SIBM [92].

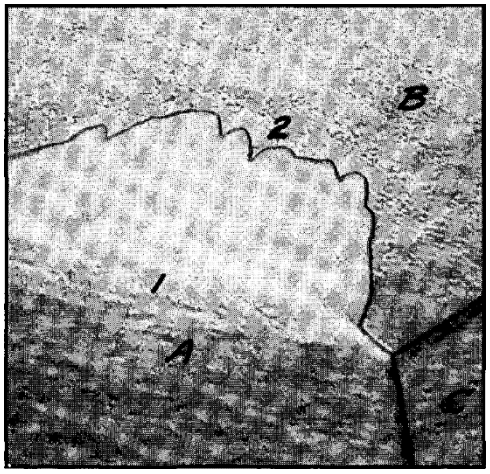

Figure 1.9: Strain induced boundary migration (SIBM) in high purity aluminum. Orientation in the area swept by migrating boundary is almost identical to that of deformed parent grain A. Magnification 75×. Reproduced from [90].

1.2.2 Subgrain growth by boundary migration

The mechanism that subgrains grow by low angle boundary (LAB) migration and eventually become nuclei was suggested independently by Cahn [7] and

Beck [93] and later developed further by Cottrell [9]. This mechanism is based on the process of polygonization, by which deformed regions may transform into nearly strain-free subgrains. By a process of LAB migration to sweep up dislocations, some polygonized subgrains tend to grow into the regions that have not yet undergone polygonization [93]. In a microstructure with an orientation gradient, the misorientations across subgrain boundaries increase through LAB migration causing an increase in mobility of the subgrain boundaries. The process proceeds until the misorientations across the subgrain boundaries approach a value at which individual dislocations within them start to lose their identity and high angle boundaries (HABs) form. Gleiter [94] observed subgrain coarsening by LAB migration by the movement of facets as shown in figure 1.10. More experimental proofs based on electron microscopy observations were presented by many authors, e.g. Fujita [95], Walter *et al.* [97], Varma [96], Ferry *et al.* [98], Huang *et al.* [99, 100].

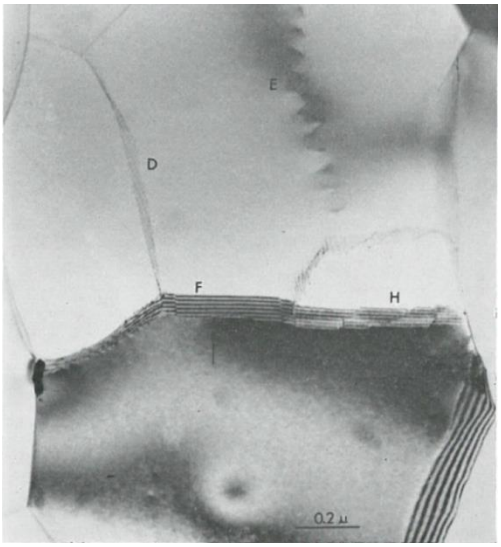

Figure 1.10: Subgrain boundaries of different dislocation densities. In the boundaries F and H several steps are visible. In the neighborhood of the facets contrast effects were observed which indicate that there exists a strain field near a step. Reproduced from [94].

1.2.3 Subgrain growth by coalescence

The mechanism suggesting that the initial stage of nucleation of recrystallization may proceed by the coalescence of subgrains was proposed by Hu [101]. During annealing of thin cold rolled Fe-3%Si single crystal samples in the TEM, he observed that the nucleation of recrystallization proceed by coalescence of subgrains. As shown in figure 1.11, the boundaries between subgrains gradually faded away, which was explained by the moving out of dislocations from the disappearing subgrain boundaries to the connecting or intersecting boundaries, and the contrast between coalesced subgrains became smaller with time. The misorientation across the connecting or intersecting boundaries might become larger as more subgrains coalesce with one another. The coalesced subgrains can grow by boundary migration only when the boundaries become HABs. With in-situ annealing experiments, Bay [102] in cold rolled aluminum and Estulin *et al.* [103] in deformed molybdenum also observed the gradual disappearance of subgrain boundaries.

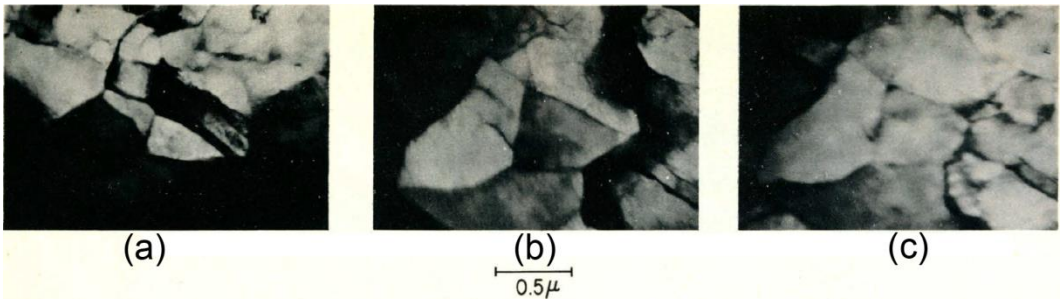

Figure 1.11: Coalescence of subgrains in Fe-3%Si alloy cold rolled to 70% seen by the gradual disappearance of some of the subgrain boundaries, and a gradual reduction in the relative contrast between the coalesced subgrains during annealing at 730 °C after (a) 30 sec, (b) 2 min, (c) 3 min. Reproduced from [101].

A more clear and direct observation of the disappearance of subgrain boundaries was achieved by Jones *et al.*, who observed that the dislocation spacing within the subgrain boundary increased near the intersecting HABs [104], as shown in figure 1.12. This change might result from the absorption of dislocations at the HAB, which leads to the gradually

disappearance of the subgrain boundary. This observation supported the investigation of Doherty [89, 106] and Li [105] who indicated that subgrain coalescence preferentially occurred at HABs. Transition bands located between deformation bands and were characterized by a high cumulative misorientation across them. In the review by Doherty [107], this mechanism was compared with other nucleation mechanisms and it is concluded that if the deformation microstructures were consisted of subgrains of similar sizes without size advantage, the mechanism of subgrain coalescence did play a vital role.

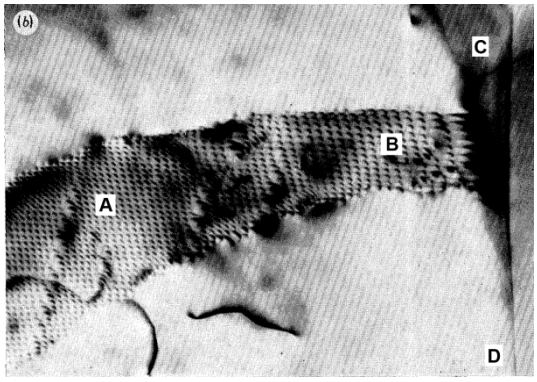

Figure 1.12: A bright field micrograph of a low angle twist boundary (A-B) which is linked to a high angle boundary (C-D). The dislocation spacing within the net of the low angle boundary is found to increase from 27 nm near A to 33 nm in the vicinity of B and the spacing of the dislocation net is even larger in the immediate vicinity of the high angle boundary. Mag. ×67000. Reproduced from [104].

1.2.4 The theory of oriented nucleation

The oriented nucleation theory for recrystallization texture formation suggests that the number of nuclei of a given orientation (e.g. cube) is higher than expected and determines the recrystallization texture. This theory was first proposed by Burgers and Louwerse in 1931 [108]. It was used to explain the orientation relationship between the recrystallized grains and the deformation matrix of a compressed aluminum sample. Burgers and Louwerse observed that as a result of competition between the nucleation rates of potential nuclei, small cube oriented regions existing in the deformed materials, preferentially grew into surrounding regions to become nuclei and grew to determine the

texture in the recrystallized state. Such nucleation of cube-oriented regions was directly observed by Ridha [109] and Duggan [110] in copper and Weiland [17] in an aluminum-manganese alloy.

1.2.5 Nucleation sites at GBs and TJs

It is well established that prior GBs and TJs are preferential nucleation sites at low to medium strains (< 40%). In moderately deformed metals, misorientations large enough for nucleation exist at such original boundaries. Vandermeer [14] found that in 99.99% aluminum cold rolled to 40% in thickness, nuclei formed as strings along GBs and also that nucleation occurred only at a small fraction of the GBs. In coarse grained aluminum alloys compressed to 20% reduction in thickness, Bellier and Doherty [91] found that nucleation only occurred at original GBs by one nucleus forming on one side of the boundary and growing into the adjacent deformed grains. At the same time, Inokuti and Doherty [111] also found that annealing the deformed iron led to nucleation predominantly at original GBs by SIBM.

Also, many scientists [14, 112, 113] observed that many nuclei formed at TJs, which are favorable for nucleation. In aluminum cold rolled to 30%-40% reduction, Vandermeer and Gordon [14] found nucleation at 6% of TJs, West *et al.* [114] found 20% of TJs had nuclei after annealing, and Sabin *et al.* [113] found nucleation at more than half of all TJs. By comparing the results with the TJ geometries in their investigations, it was suggested that there was a strong influence of the TJ geometries on nucleation of the TJs: irregular TJs gave more nucleation than well-annealed TJs with near 120° angles between the 3 boundaries. More observations on nucleation at GBs and TJs were presented by other authors, e.g. Beck *et al.* [93], Wu *et al.* [13], *etc.*

1.2.6 Nucleation sites at particles

As mentioned in section 1.1.4, zones of high SE with highly misoriented microstructures are formed around large hard particles during deformation. Lesile *et al.* [15] were the first to find that these zones are preferred sites for the nucleation and Humphreys and Ferry [121] found nucleation at particles

occurred with the formation of a nucleus at least partially surrounded by HABs. Therefore the misorientation within the deformation zone must be large enough to form HABs to the matrix or HABs must form after recovery in the deformed matrix. The occurrence of nucleation is thus related to both the particle size and the strain. As shown in figure 1.13, the critical size for particle stimulating nucleation (PSN) increase as the deformation is decreased [16].

Turnbull and Burke developed an explanation for the nucleation at particles, concluding that new grains could arise from undeformed metal embedded in micro-cavities in particles (see figure 1.14) [122]. This is similar to Lesile's assumption that the function of second phase particles was to provide regions in which the lattice was relatively undeformed and in close conjunction with regions of highly deformed regions [15]. In an in-situ annealing experiment, Humphreys directly observed that nucleation originates within a zone at the particles of high dislocation density and large lattice misorientations with respect to the matrix and proceeds by a rapid process of polygonization and subgrain boundary migration [16]. Once the subgrain boundary becomes a HAB, a nucleus is considered to have formed and can grow into the deformed matrix by HAB migration. Generally, only one nucleus was observed to form at particles of size range 1-5 μm [16], while multiple nuclei were likely to form at the particles larger than 10 μm [123].

It is found that the influence of fine particles with diameter less than 0.1 μm on nucleation is related to particle spacing. During deformation, fine and closely spaced particles produce more homogeneous dislocation structures with a lower mean misorientation between adjacent subgrains, and they pin subgrain boundaries during annealing and thus inhibit nucleation [124, 126]. Fine and widely spaced particles are found to have limited effects on nucleation since the microstructures are unaffected by the particles during deformation [127].

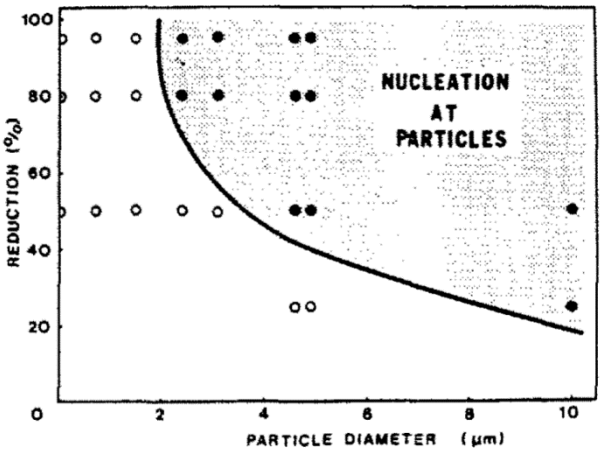

Figure 1.13: The conditions of deformation and particle size for which nucleation is observed to occur at particles of Si in rolled Al crystals. Reproduced from [16].

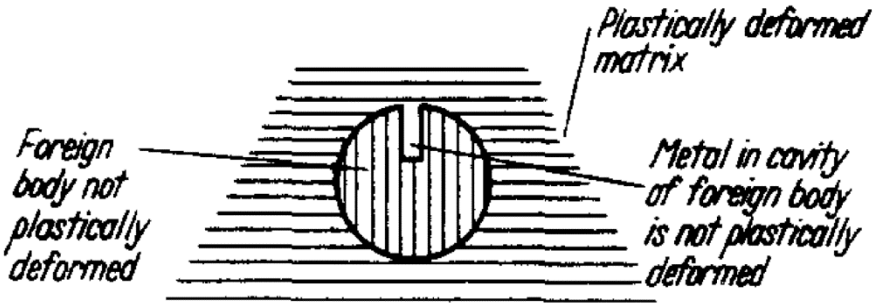

Figure 1.14: Unstrained part of metal retained in a cavity of a hard inclusion. Reproduced from [122].

1.2.7 Nucleation sites at hardness indentations

Surface imperfections such as scratches and hardness indentations can stimulate nucleation [19, 20]. As mentioned in 1.1.5, hardness indentations provide extra driving force for nucleation and subsequent growth during recrystallization. Several investigations have been done to study nucleation at hardness indentations. At Vickers hardness indentations in aluminum samples, big subgrains preferably formed at the position with the most severe deformation [128]. Cahn thought the nucleation was based on the process of polygonization [129]. In 1969, Eylon also did work on nucleation at hardness indentations indented both with sharp and ball indenters, with observation that

the shape of the indenter influenced the nucleation potentials: a sharp indenter led to more nucleation than a ball shaped one and the overlapping region of two indentations also gave higher nucleation probabilities [19]. In his experiments, only one nucleus was observed around each indentation, while other investigations showed that several nuclei formed at one indentation [130, 131]. Furthermore, Xie [130] and Zambaldi [131] observed that the size, shape and depth of the recrystallization regions around hardness indentations were different for different crystallographic orientations in the deformation zones. The size of the recrystallized grains far from the indentation tips was observed always to be larger than those near the indentation tips, which might be due to the larger number of nucleation sites at indentation tips than in the matrix [130]. Additionally, the recrystallization below indentations was affected by annealing temperature: at higher annealing temperature, fewer nuclei were observed to form because fast migration of the boundaries surrounding the nuclei at high temperatures might quickly consume volumes in the deformation zone which otherwise could have initiated more nuclei [131].

1.2.8 Orientation relationships between nuclei and deformed matrix

The nucleation mechanisms described above propose that the orientations of the nuclei must already be present in the deformed state before annealing. As mentioned in 1.2.1, SIBM can be considered as recrystallization without the formation of nuclei with new orientations, i.e. with orientations different from the deformed matrix. Subgrain growth involve the merging of multiple subgrains of similar orientations either by rotation (subgrain growth by coalescence, see section 1.2.3) or by migration of the LABs (subgrain growth by LAB migration, see section 1.2.2). The orientations of the nuclei are therefore closely related to the deformed matrix where they form, which is expected to result in a recrystallization texture closely related to the deformation texture. Nuclei with orientations the same as the deformed matrix were observed in many investigations, e.g. Humphreys *et al.* [16, 80, 132], Jack *et al.* [133], Ardakani *et al.* [134], Xu *et al.* [135] *etc.*

However, nuclei with new orientations different from the deformed matrix were also observed in a number of investigations [136, 137]; typically nuclei with orientations rotated about a pole close to <111> relative to a deformed grain [74, 113, 138, 139]. For example, in a partially recrystallized Al-Si alloy, Skjervold and Ryum [112] found that 25% of nuclei in materials deformed to ε=0.2 and 54% of nuclei in materials deformed to ε=0.4 had one <111> axis in common with the surrounding matrix. The rotation angle about a <111> axis of nuclei relative to the surrounding matrix was in the range 35°-45° for about 50% of these cases [112]. Additionally, a number of nuclei with random orientations different from the surrounding matrix were also observed [112]. Recently, Miszczyk and Paul observed nuclei related to the deformed crystals by misorientation angles in the ranges of 25°- 35° and 45°- 55° around axes near <111> in deformed copper and nickel [140]. Concerning these observations, it is debated if the nuclei come from pre-existing regions that have not been characterized due to limitations in the characterization method: (1) the initial regions may be so small that they are below the spatial resolution limit of characterization technique (~20 nm); (2) the nucleation takes place in a section lying either below or above the characterized surface [114].

1.2.9 Twinning

It should be noted that twining is not considered above. Although twinning is not a nucleation mechanism, it is a well-accepted mechanism for the development of grains with new orientations that are not present in the deformed microstructures [117-119]. Moreover, the new orientations generated by twinning were often observed to have more favorable orientations for subsequent growth than the original recrystallization nuclei, so it was proposed that twinning was an important factor in determining recrystallization textures [1-2]. Annealing twins were frequently observed in fcc metals of low or medium stacking fault energy, such as nickel and copper [13, 118], while they were comparatively rare in high stacking fault energy metals such as aluminum. Gottingen *et al.* [120] and Humphreys *et al.* [117] found that annealing twins

were more frequently formed at high energy interfaces, i.e. more frequently at free surfaces than in the specimen interior.

1.3 Overview of the thesis

The objective of this study is to explore nucleation of recrystallization in selected model samples, in which we have some control over where nucleation is likely to happen. The selected model samples are deformed columnar-grained nickel and high purity aluminum with hardness indentations. The outline of the thesis is as follows:

Chaper 2 describes the different experimental techniques applied: Vickers hardness, optical microscopy, SEM, EBSD and DAXM. DAXM will be presented in much detail as it is not a widely known method and the description will include the set-up, diffraction theory, and the data collecting and processing methods.

Chaper 3 describes 2D experiments and results of nucleation at TJs in columnar-grained nickel. The potentials of TJs as nucleation sites and the orientation relationships between nuclei and the surrounding matrix are presented. A possible correlation between the difference in hardness of the grains at the TJs and the nucleation potentials is suggested.

Chaper 4 describes 2D experiments and results on nucleation at hardness indentations in coarse grained high purity aluminum. Nucleation at grains of different initial orientations is discussed first, in particular to clarify if many indentations in one grain can lead to nuclei of many different orientations or of similar orientations, and to quantify if grains of different orientations have different nucleation probabilities. Then potential nucleation sites and the effect of annealing temperatures and time on nucleation are also presented. Finally, the influence of deformation amount on nucleation is discussed.

Chapter 5 reports the details of the synchrotron DAXM experiment followed by the processing and analysis of the synchrotron data. By mapping the same volume before and after annealing, nuclei are observed and the nucleation sites

are pinpointed in the deformed volume. Furthermore, the nucleation and subsequent growth are directly correlated to the local microstructures in the deformed matrix, and effects hereof are described.

Chapter 6 contains a summary of the main results as well as the conclusions. An outlook is also presented in this chapter.

Chapter 2

Experimental techniques

This chapter provides an introduction of the experimental techniques used in this work, namely Vickers hardness, electron backscattered diffraction (EBSD), electron channeling contrast (ECC) and differential aperture X-ray microscopy (DAXM).

2.1 Vickers hardness test

In this study, a Vickers hardness tester of Struers DuraScan was used. The indenter is a diamond indenter with pyramidal shape, with a square base and an angle of 136° between opposite faces. The indenter is pressed into the samples with a specified load. The Vickers hardness value (Kgf/mm^2) is determined as

$$HV = 2Fsin\frac{136°/2}{((d_1+d_2)/2)^2} \quad (2.1)$$

where F is the indenting load an d_1 and d_2 are the length of the two diagonal lines of the indentation. In the present work, the dwelling time was 10 s. The minimum load 10 g was used for columnar-grained nickel samples in order to measure the hardness close to TJs. Two loads of 500 g and 2000 g were used for aluminum samples, in order to investigate the influence of indenting load on local misorientations and SE distributions as well as on nucleation during a subsequent annealing.

2.2 Electron backscattered diffraction (EBSD)

EBSD provides simultaneously microstructural and crystallographic information of crystalline materials. With EBSD, the grain size, grain boundary spacing, texture, local grain orientation and phase identity can be determined.

The microscope setting for EBSD measurements is illustrated in figure 2.1(a). A sample with flat surfaces is inclined at an angle 70° to the incident electron

beam. The accelerating voltage is typically 10-30 kV with an incident beam current of 1-50 nA. With a stationary electron beam hitting the sample surface, backscattered electrons are diffracted at crystal lattice planes according to Bragg's law (see figure 2.1(b)). Based on the diffraction pattern the crystallographic orientation of the selected sample point is determined. The nominal angular resolution is about 1.5°, which is related to the resolution of the EBSD detector and its position with respect to the sample. The spatial resolution is 20 nm for nickel and 30 nm for aluminum [141- 143].

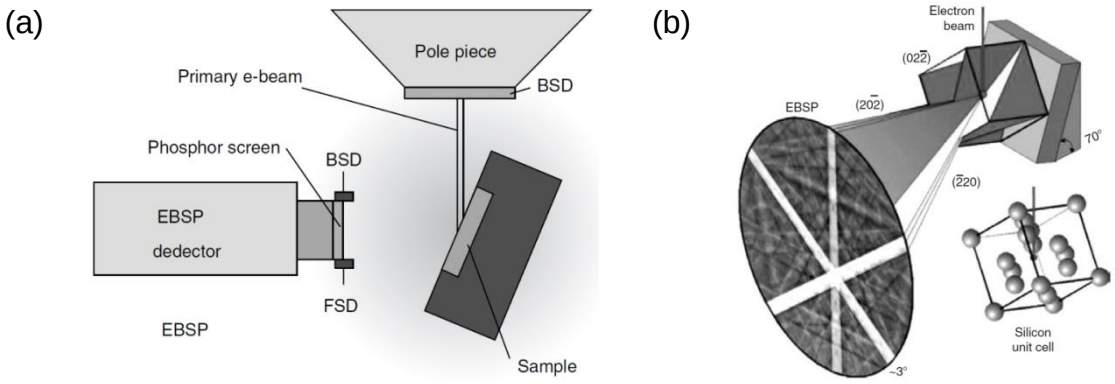

Figure 2.1: (a) Schematic arrangement of the EBSD set-up in the SEM. (b) Electron interaction with silicon. Reproduced from [144].

In the present study, a Zeiss Supra-35 FEG SEM equipped with an HKL Channel 5 EBSD system was used for orientation mapping. The accelerating voltage was 20 kV. Samples for EBSD measurements were ground to 4000# SiC paper followed by electron polishing or mechanical polishing using 3 µm, 1 µm and 40 nm oxide polishing suspension subsequently. The sample surface polishing and the step size used when acquiring the EBSD patterns were different for different samples and will be described where relevant. The HKL Channel 5 software was used to process the EBSD data. In the EBSD maps, LABs are defined as boundaries with misorientation between 2° and 15°, and HABs as boundaries with misorientation higher than 15°. Recrystallized grains were identified from the EBSD data obeying the following criteria: 1) be a continuum consisting of pixels with a pixel-to-pixel misorientation smaller than

2°; 2) be larger than a critical size, 3 µm; 3) be surrounded at least partly by HABs.

2.3 Electron channeling contrast (ECC)

When an electron beam hits a sample surface, backscattered electrons (BSEs) are generated due to interactions between the incident electrons and the samples [146]. The BSEs are affected by the following factors.

(1) Atomic number: the higher the atomic number, the more BSEs are generated and hence the signal is stronger, i.e. brighter resulting images. This is so-called Atomic Number Contrast.

(2) Topography: if the angle between the sample surface and the incident beam changes, both the penetration depth and scattering angles change and consequently the images will have different brightness. Topography effectively changes the angle between sample surface and incident beam locally, which can be used to detect subtle topography differences. This is Topography Contrast.

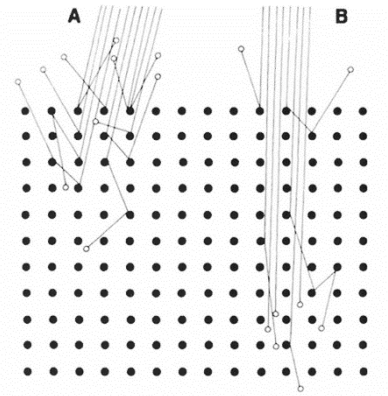

Figure 2.2: Particle model of electron channeling contrast imaging as the incident beam changes its angle relative to a crystal lattice. (A): Back scattering is strong when the beam has a large angle to a set of atomic planes. (B) Back scattering is reduced if the beam is almost parallel to a set of atomic planes. Reproduced from [145].

(3) Crystallographic orientations: the intensity of BSEs is related to the angle between the incident beam and the crystal lattice plane, so changes in both the crystallographic orientation and the direction of incident beam can cause changes in BSEs intensity and thus changes in the brightness of the images. This mechanism is illustrated in figure 2.2.

2.4 Differential-aperture X-ray microscopy (DAXM)

2.4.1 The Laue method

According to Bragg's theory, the atom planes are considered to behave as reflecting planes. Constructive interference occurs when the path difference between reflections from successive planes in a plane family is equal to integer multiples of wavelengths:

$$n\lambda = 2d_{hkl}sin\theta \tag{2.2}$$

where λ is the wavelength, n is the order of the reflection, d_{hkl} is the lattice plane spacing and θ is the angle of incidence to the planes.

X-ray techniques characterizing crystals mainly include the Laue method, oscillation, rotation and precession methods. DAXM is based on the Laue method. The Laue method utilizes white (polychromatic) X-rays. The white X-rays contain a range of wavelengths which leads to a set of Ewald reflecting spheres of different diameters when the white X-rays are reflected by crystallographic planes. As shown in figure 2.3, these spheres closely pack together and are tangent at point O, the origin of the reciprocal lattice. The radii of two Ewald spheres OA (for the X-ray with maximum wavelength) and OB (for the X-ray with minimum wavelength) can be determined as $|\mathbf{OA}| = 1/\lambda_{max}$ and $|\mathbf{OB}| = 1/\lambda_{min}$. Any plane with reciprocal lattice point within the region between the two Ewald spheres (the shaded region) will fulfill Bragg law for one particular wavelength and Bragg diffraction will occur.

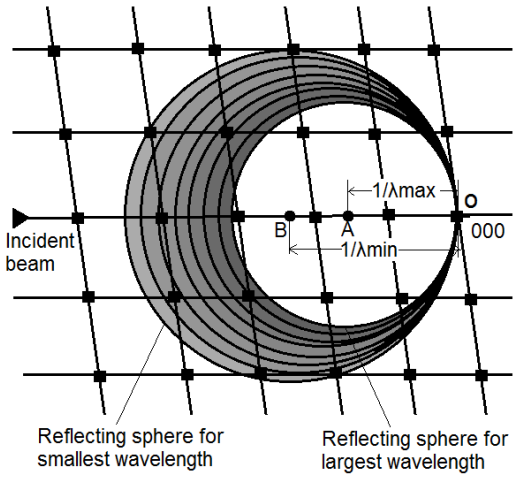

Figure 2.3: The Ewald reflecting sphere construction for the zero section of a reciprocal lattice of a crystal for white X-rays. A range of wavelengths from the smallest (largest sphere) to the largest (smallest sphere) gives rise to a set of spheres packed closely. The reciprocal lattice points lying within the shaded region satisfy Bragg's law.

2.4.2 DAXM set-up

The DAXM technique introduced here is only available at Advanced Photon Source (APS), Argonne National Laboratory. The setup for DAXM is sketched in figure 2.4. An undulator white X-ray beam enters from the right. Kirkpatric-Baez (K-B) mirrors are designed to focus the incident beam to provide an X-ray microbeam of ~0.5 µm [147]. The sample is mounted on a sample holder at a 45° incidence angle to the incident focused microbeam. The Laue diffraction pattern from the gauge volume exposed to the incident microbeam is recorded on a charge-coupled device (CCD) X-ray area detector mounted in a 90° reflection geometry, above the sample, ensuring high angular acceptance. To resolve the diffraction pattern from each grain at different depths, a Pt-wire of 50 µm diameter is used as a differential aperture and scanned along the sample surface at a distance of ~100 µm from the sample surface.

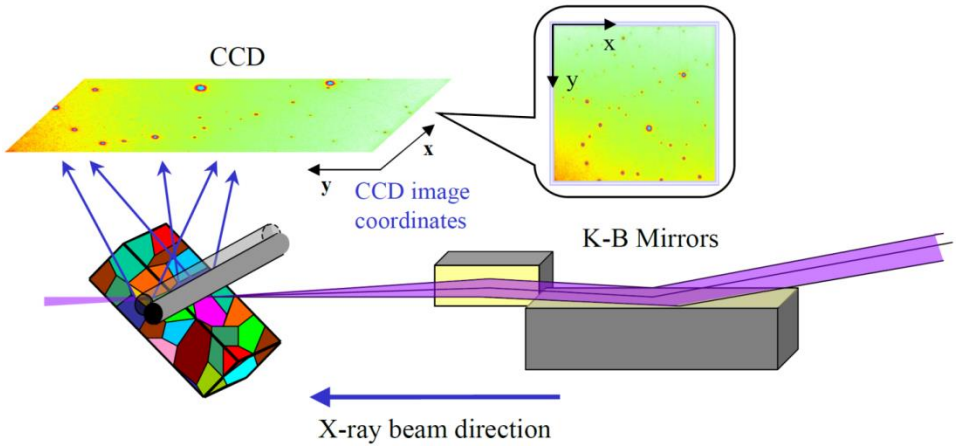

Figure 2.4: Schematic depiction of the differential-aperture X-ray microscopy layout, where the K-B mirrors focus the incident beams to ~0.5 µm diameter, the Pt wire is used as a diffracted beam profiler and a CCD area detector collects white beam Laue diffraction patterns. Reproduced from [148].

Figure 2.5 illustrates this method for obtaining depth-resolved Laue patterns from bulk samples. A CCD image is collected when the platinum wire is at position (n). Then the wire is stepped to position (n+1) where a second CCD image is collected. According to the positions of the incident beam, the wire and the individual CCD pixels, the differential intensity [I(n)-I(n+1)] in each pixel of the detector can be assigned to the voxels along the microbeam. By stepping the wire across the diffraction pattern, the intensity of the (h'k'l') and (h''k''l'') reflections are generated. The pixel positions, the geometrical error, the step size, step direction and the circular shape of the Pt wire are taken into account. It is necessary that $D_{XR} \ll D_{CCD}$ (see figure 2.5) in order to ensure that the error correction due to CCD pixel size is small and that the spatial resolution of the reconstructed diffraction patterns is determined mainly by the step size of the Pt wire differential aperture.

By assigning the differential intensity of each pixel of the detector to the corresponding voxels by the LaueGo software available at the APS beamline 34-ID-E [149], the complete Laue diffraction patterns are extracted as a function of depth along the incident direction of the polychromatic beam. The crystallographic orientations are then indexed based on the depth-resolved

Laue patterns also using LaueGo software. The orientation resolution obtained is about 0.01° [25]. The output 3D orientation data is post processed using Matlab codes, i.e. detecting nuclei, extracting deformed matrix consumed by the nuclei, finding nucleation sites and calculating SE. The methods will be described in section 4.5. Dream3D, Paraview and ImageJ are used to visualize the data.

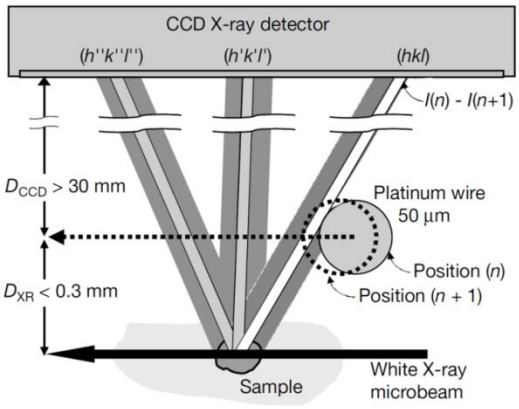

Figure 2.5: Differential-aperture X-ray microscopy depth-resolving method. Schematic view of a white microbeam hitting a sample and diffracting onto a CCD area detector. Bragg diffraction for the (hkl), (h'k'l') and (h''k''l'') Laue reflections is depicted for a small voxel within the sample. A Pt wire is at position (n) and the dashed circle indicates the next (n+1) position of the wire. Reproduced from [25].

Chapter 3
Nucleation in columnar-grained nickel at triple junctions

This chapter reports results for nucleation of recrystallization at TJs in columnar-grained nickel cold rolled to 50% reduction in thickness. First a description of the columnar-grained nickel samples is given followed by experimental methods used. The nucleation at TJs was investigated in detail in three samples. Effects of hardness of the grains at TJs as well as the hardness difference between the grains at the TJs on nucleation were evaluated. Nucleation sites and orientation relationships between the nuclei and the surrounding matrix were analyzed.

3.1 Materials and experimental details

High purity columnar-grained nickel was prepared by directional solidification. A center layer of size 4×10×30 mm^3 was cut from the ingot (see figure 3.1(a)). The growth direction was <100>, as shown in figure 3.1(b). When looking perpendicular to the growth direction, the material has a coarse grain structure with an average grain diameter of 600 µm. By optical microscopy of the section parallel to the growth direction (see figure 3.2), it can be noticed that the grains have an almost perfect columnar shape as all the grain boundaries (GBs) are nearly vertical. An important motivation for choosing columnar grained sample for the present work is that nucleation from ‘below-the-surface deformed grains’ is avoided.

Then the sample was cold rolled to 50% reduction in two passes. For each pass, the geometric parameter l/h, where l was the contact length between the roller and sample and h was the average sample thickness before and after each pass, was around 2.0, therefore the deformation was expected to be relatively

homogenous [150]. During rolling, the grain growth direction was parallel to the normal direction (ND) of the sample (see figure 3.1(a)). Three samples (named S-1, S-2 and S-3) were cut from the rolled sheet (see figure 3.1(a)). Then each sample was cut perpendicularly to the growth direction into two identical pieces, the upper pieces for annealing experiments and the lower pieces for hardness tests. All the pieces were ground and electro polished. Extreme care was taken to get rid of surface imperfections, especially scratches, to avoid nucleation from such sites.

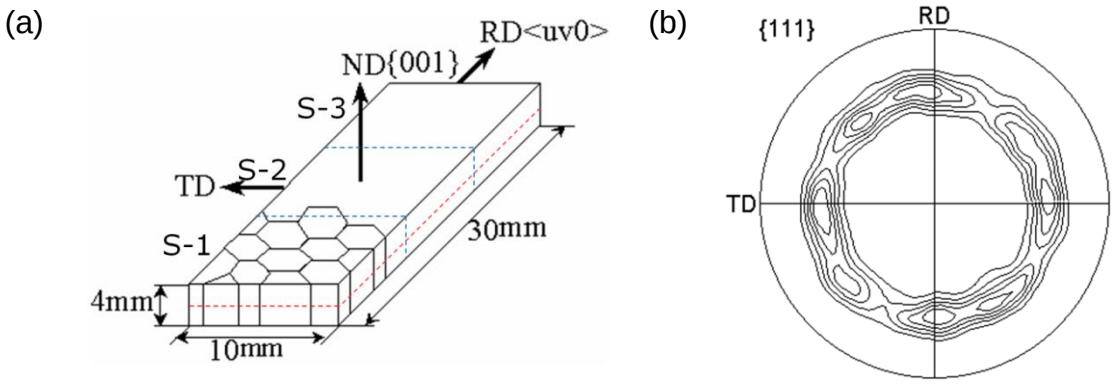

Figure 3.1: (a) A sketch of the columnar-grained sample illustrating the cold rolling and the sectioning at the sample. Along the blue dashed lines, the sample was cut into three samples and then each sample was cut into two pieces along the red dashed line. (b) A {111} pole figure of the texture of the initial columnar-grained Ni before cold rolling.

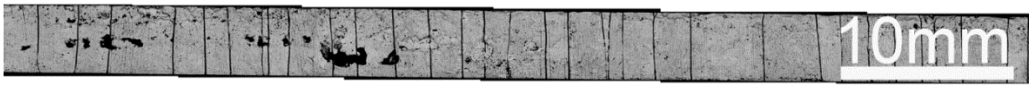

Figure 3.2: The longitudinal view of the columnar-grained Ni.

The three upper pieces of the samples were first characterized in the RD/TD planes by optical microscopy to record the positions of GBs and TJs. Then they were annealed at 350 °C for 1 h to recover the deformed microstructure, and then at 420 °C, 400 °C, 395 °C for 1 h for sample S-1, S-2 and S-3, respectively. Three different annealing temperatures are applied to enhance nucleation probability. After annealing, optical microscopy was used to reveal nucleation sites one the six RD/TD planes (two RD/TD planes for each sample). On one of

the RD/TD plane of each sample, EBSD mapping was then performed at those TJs where nuclei were observed, to determine the orientations of the nuclei and the microstructures around the nuclei. Hardness tests were conducted using a force of 10 g around the relevant TJs on the identical lower pieces, which were deformed but not annealed.

3.2 Nucleation sites

A montage of the optical micrographs is made for each sample to show the GB structure. Figure 3.3 is such a montage for sample S-1. After annealing, nuclei are identified and the nucleation sites are marked by red circles and numbered in the montage of deformed state as shown in figure 3.3. In total, 47 nucleation sites are observed in the three samples with 35 (74.5%) right at TJs (e.g. nucleation site 1-6 in figure 3.3 and a nucleus in figure 3.4(a)), 12 (22.5%) at GBs (e.g. nucleation site 7 in figure 3.3 and nucleation in figure 3.4(b)) and none within grain interiors.

This result clearly shows the prevalence of TJs as the nucleation sites, which is in general agreement with previous investigations [14, 113, 114]. It should be noted that all the nuclei formed at GBs are actually very close to the TJs, within 50 μm. Figure 3.4(b) is an example. Although the GBs are almost perpendicular to the RD/TD plane, there are of course some small variations (see figure 3.2). So the nuclei observed at GBs may well be formed closer to the TJs at a lower section.

3.3 Orientation relationship between nuclei and the surrounding matrix

Conducting EBSD characterization on a RD/TD plane of a sample damaged the one of the two RD/TD planes of each sample, so the microstructures around only 33 nucleation sites out of the total 47 were characterized using EBSD after detecting nuclei using optical microscopy, including 22 at TJs and 11 at GBs. The misorientations between each nucleus and all the neighboring pixels in the

recovered matrix were measured. The pixel with the smallest misorientation was determined.

Based on the minimum misorientations between the nuclei and their surrounding deformed matrix, the nuclei are categorized into three groups: ① Nuclei with minimum misorientation to the deformed matrix smaller than 15°. These are referred to as parent type; ② Nuclei forming ∑3 boundaries (following the Brandon criteria, i.e. within 8.66° deviation from ideal 60°<111> relationship). These are referred to as twin type; ③ Nuclei that do not belong to any of the above two types. These are referred to as new type.

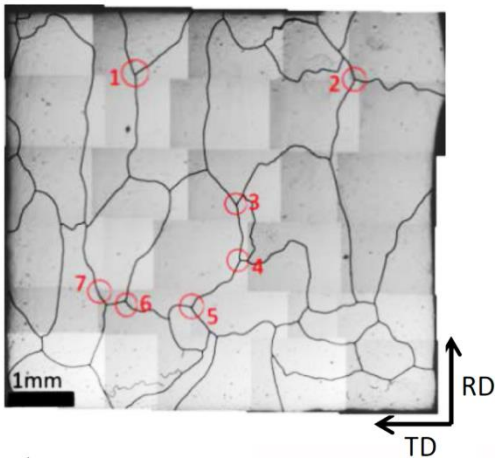

Figure 3.3: A montage of optical micrographs showing the grain boundary structure of the deformed upper piece of sample S-1. Numbers and red circles are used to identify nucleation sites of this sample after annealing. Reproduced from article A.

(a)

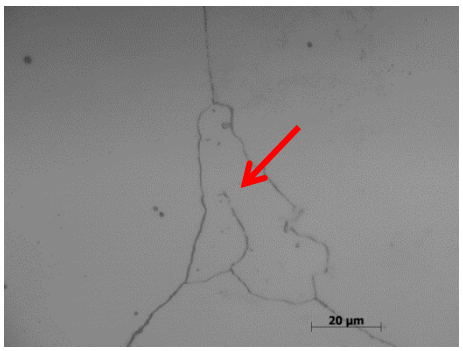

(b)

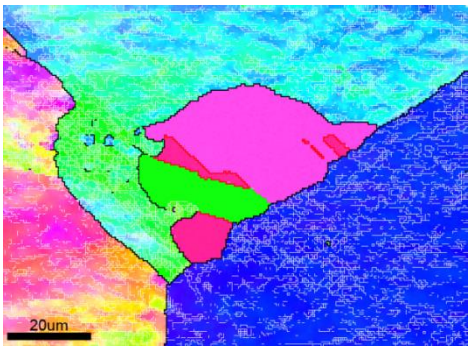

Figure 3.4: (a) Optical micrograph of a nucleus (marked by an arrow) formed at a triple junction and (b) orientation map of nuclei formed at grain boundaries

very close to another triple junction.

At a few TJs, a series of nuclei are observed. These nuclei are often twin or double twin-related to each other. For such cases the nuclei are classified as parent type and twin type if they are parent or twin-related to any of the deformed grains, respectively.

3.3.1 Nuclei of parent type

One example of nuclei of parent type is shown in figure 3.5, where a nucleus and 3 deformed grains at the TJ are marked and numbered as N1 and G*j* (*j* = 1-3), respectively. As seen in figure 3.5, the nucleus N1 forms a low angle boundaries (LABs) to the deformed grain G1, and N1's orientation lies at the outskirts of the orientation cloud for grain G1 (see figure 3.5b). The nucleus N1 is therefore considered to originate from the deformed grain G1.

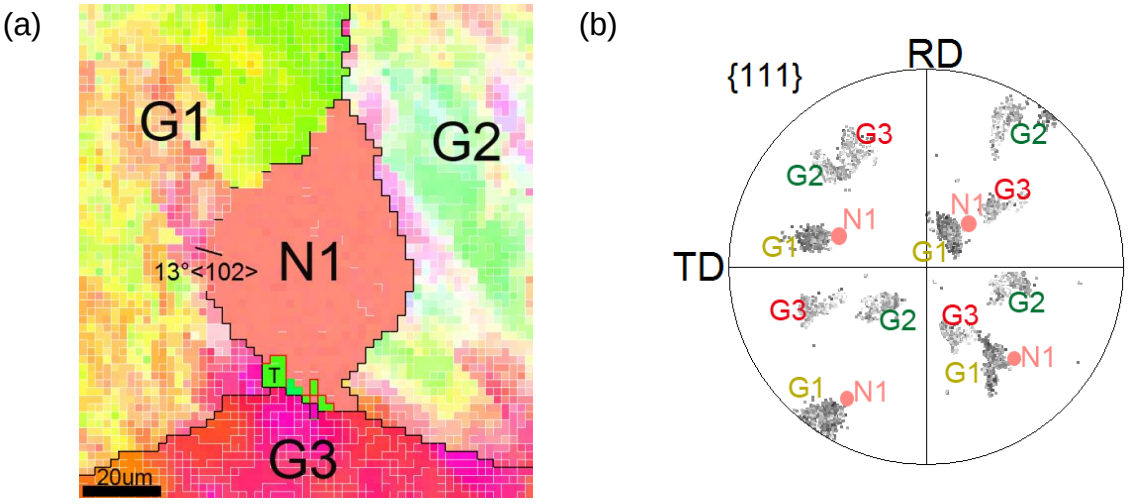

Figure 3.5: (a) EBSD orientation map and (b) {111} pole figure to show the orientations of the 3 deformed grains and the nucleus. Fine white lines show low angle boundaries (>= 2° and <15°), coarse black lines high angle boundaries (>=15°), and red lines 60°<111> twin boundaries in figure (a). Reproduced from article A.

A small grain, named T1, is also seen in figure 3.5, which has a twin relationship with the nucleus N1. The grain T1 has a smaller size than nucleus

N1 and is therefore considered to develop by twinning during the growth of N1, and will not be considered as a new nucleus. It could also be T1 that forms first and then twins into N1. But as N1 has a parent orientation and T1 does not, it is here considered most likely that N1 has formed first. In total parent type nucleation is found at 10 (30.3%) nucleation sites, including 8 at TJs and 2 at GBs. For these nuclei, subgrain growth or SIBM can be the active nucleation mechanisms.

3.3.2 Nuclei of twin type

Nineteen nuclei (57.6%) are observed to be twin-related to one of the neighboring deformed grains. Sixteen of the 19 nuclei have the exact twin relationship. For the other three twin-related nuclei, their misorientation are a few degrees off the exactly twin relationship in angles and/or in axes. As there are relatively large orientation variations in the deformation microstructure before annealing (see the pole figure in figure 3.5 and 3.6), these 3 nuclei might develop with the exact twin relationship, at the site where it formed. Once the nucleus has grown, a small change of the boundary misorientation is expected. Therefore, it is reasonable to believe that the near (but not exact) twin relationship of the nuclei is an effect of growth. These nuclei are therefore included as twin type. For example, in figure 3.6, the misorientation between the nucleus N2 and the deformed grain G6 is around 56°<443>, which is about 8.1° away from the ideal 60°<111>. The nucleus N2 is therefore considered to originate from grain G6 through twinning.

(a)

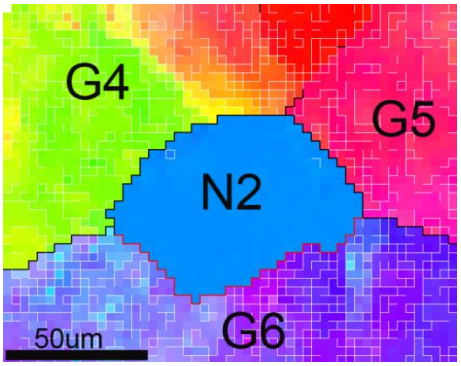

(b)

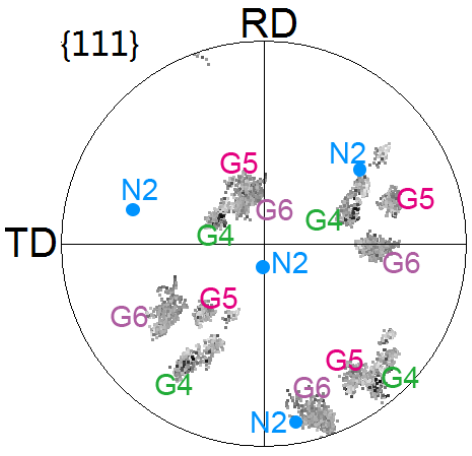

Figure 3.6: (a) EBSD orientation map and (b) {111} pole figure to show the orientations of deformed grains and nuclei. The boundaries are defined as figure 3.5. Reproduced from article A.

Annealing twins in aluminum is rare compared to other fcc metals of low or medium stacking fault energy. Therefore, little attention was devoted to annealing twins in aluminum until research on the origin of recrystallization textures suggested extensive twin formation during the early stages of recrystallization of several fcc metals including aluminum [115, 116]. Twinning generates new orientations that are not present in the deformed microstructures, which are often observed to have more favorable orientations for growth and thus twinning is suggested as an important factor in determining recrystallization textures [117]. In the present experiment, it cannot be concluded whether the nucleus is formed by twinning directly from a given grain, or nucleus of parent type first forms below the surface and a new nucleus then forms by twinning during growth of the underlying nucleus.

3.3.3 Nuclei of new type

There are 4 cases (12.1%) where the nuclei do not have orientation belonging to the above two types. The nuclei do not form Σ1, Σ3 or Σ9 boundaries to any of the surrounding deformed grains. This result agrees with reference [112, 13], in which some of the recrystallized grains have new orientations. Compared with the results in [13], the present investigation shows less nuclei with new orientations. This might be related to the recovery process occurring during the initial low temperature annealing in the present experiment. As the deformation microstructures coarsen, and the dislocations and thus the SE are reduced during the recovery, the formation of nuclei with new orientation may be less likely because there are no enough dislocations to form the new HABs.

Mechanism responsible for the formation of nuclei with new orientation are discussed in [13, 114, 140], but because of the limited number of nuclei with new orientations in the present work, these mechanism cannot be evaluated.

3.4 Hardness tests

After annealing at a certain temperature, not all TJs stimulate nucleation. In the present work, only about 16% have developed nuclei upon annealing. Vandermeer and Gordon [14] observed nucleation at 6% of TJs and Sabin *et al.* [113] observed nucleation at more than half of the examined TJs. In order to learn more about which TJs stimulate nucleation, microhardness around 21 TJs is measured, including 13 TJs where nuclei are found at the same TJs in the identical upper sample pieces, defined as Group A TJs and 8 TJs where no nuclei are found in the identical annealed pieces, defined as Group B TJs. Figure 3.7 is an example of microhardness measurements at a TJ.

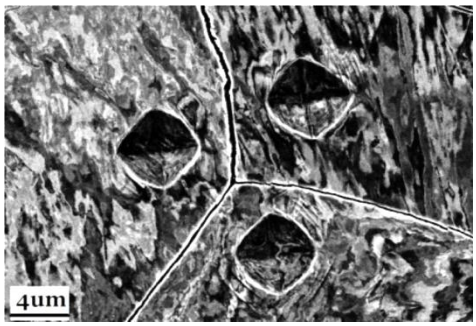

Figure 3.7: Example showing the microhardness tests around a triple junction. Reproduced from article A.

The Hardness distributions of all three microhardness values around TJs within both Group A and B TJs are shown in figure 3.8. It can be seen that the hardness distribution of Group A spans a wider range than that of Group B. On average, however, the hardness values for Group A and B are the same, namely 20.7 Kgf/mm^2. Combining the hardness values and the nucleation information at each TJ, it is found that the nuclei seem to originate both from crystals with either the lowest or the highest hardness values for the three grains in Group A TJs. The hardness values of the grains at a TJ therefore seem not to be very useful for the TJ which will stimulate nucleation.

The wider distribution of hardness of Group A TJs than of Group B TJs may indicate that a larger difference in hardness between the grains at a TJ may

lead to nucleation. To test this hypothesis, the hardness difference, equal to the difference between the maximum and the minimum hardness (see figure 3.9(a)), is thus calculated for each TJ (see figure 3.9(b)). It can be seen that Group A TJs have a larger hardness difference than Group B TJs.

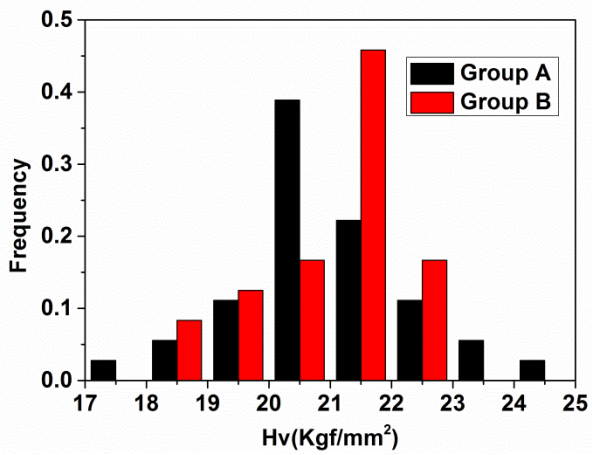

Figure 3.8: Distribution of microhardness of all 3 grains at Group A and Group B triple junctions. Reproduced from article A.

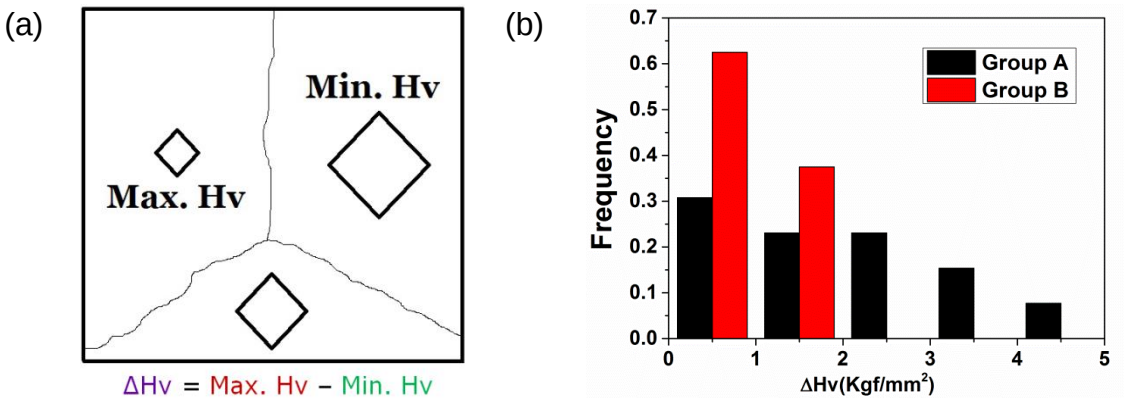

Figure 3.9: (a) Sketch showing the calculation of the microhardness difference at triple junctions. (b) The distribution of the microhardness difference between the maximum and minimum hardness at Group A and Group B triple junctions. (b) is reproduced from article A.

Nucleation by subgrain growth or SIBM would be facilitated by a difference in SE (here taken proportional to the hardness), which will drive the boundary towards the higher SE. It thus makes sense that more nucleation is seen when

the hardness difference is large as it is predominately the case for Group A TJs. It has, however, to be noticed that there are also Group A junctions with low hardness difference and that the statistics of the present investigation is rather poor. Also, it is not clear whether the initial recovery may affect the result. The hardness values are measured in the deformed samples prior to recovery. It however seems reasonable that a large hardness difference facilitates nucleation and it would be of interest to further substantiate this suggestion by measurement at more TJs.

3.5 Summary

In a cold rolled columnar-grained pure Ni sample it is found that all nuclei form at TJs (74.5%) and at original GBs (25.5%) near TJs (within 50 μm). The vast majority of the nuclei has orientations similar to the orientations of the surrounding grains or is twin-related to one of the surrounding recovered grains. Only at 4 nucleation sites, nuclei are formed with new orientations. This is lower than that observed in a previous investigation and may be due to an effect of the initial recovery of the sample in the present investigation. Active nucleation mechanism may be SIBM, subgrain growth and subgrain coalescence *etc*.

Hardness measurements at TJs in the initial deformed sample indicate a weak correlation between the difference in hardness of the grains at the TJs, ΔHv, and the potentials of the junction to form nuclei; the higher the difference in hardness, the more likely is nucleation. Further studies are needed to test this hypothesis.

Chapter 4
Nucleation at hardness indentations in high purity aluminum – 2D

This chapter deals with nucleation in weakly rolled aluminum further deformed locally by well-distributed hardness indentations. The investigations are by 2D-EBSD/ECC measurements. The main aims of the 2D investigations are: ① to study the fundamental aspects of nucleation at hardness indentations, such as where and how the nuclei form and what orientations the nuclei have; ② to investigate effects of the deformation amount on nucleation, such as rolling reductions and indenting loads; ③ to explore effects of initial grain orientations on nucleation at hardness indentations, and ④ to obtain statistical results preparing for the 3D synchrotron experiment (see Chapter 5).

4.1 Materials and general experiments

High purity (99.996%) aluminum was used. The initial material had a coarse and inhomogeneous microstructure with an average grain size of 300 μm. This grain size was not large enough for the planned experiment in which several hardness indentations had to be done within each selected grain. Therefore, all surfaces were ground using 4000# SiC paper and electro polished to prevent nucleation at surface scratches and then the samples were subsequently annealed at 590 °C for 7 days. After this annealing, grains with sizes ranging from 500 μm to 20 mm were obtained, which was ideal for the present experiment. The deformation was done in two steps: cold rolling, which provided driving force for nuclei growth, and hardness indentations, which provided extra driving force to stimulate nucleation. One sample was cold rolled to 12% reduction (named 12%-sample) and the other was cold rolled to 20% reduction (named 20%-sample) in thickness in two passes, each with the geometric parameter l/h around 2, where l was the contact length between the

rollers and the sample and h was the average sample thickness before and after each pass. With the specified rolling setup, the deformation was expected to be relatively homogeneous through the sample thickness [150].

All samples used in this chapter were cut from either the 12%-sample or 20%-sample, and were then carefully ground and electro polished. It was difficult to observe the grain boundaries (GBs) directly by optical microscopy. Therefore, EBSD measurements using large step sizes were performed to find the GBs, as shown in figure 4.1(a). Hardness indentations were then done on RD-TD planes of all the samples using a Vickers diamond indenter of pyramidal shape. Pyramidal shape is chosen to produce a highly inhomogeneous deformation microstructures, which would facilitate nucleation. All indentations were far away from GBs, as illustrated in figure 4.1(b). The distance between indentations was larger than *3d*, where *d* was the length of the diagonal lines of the indentations, thereby avoiding overlapping of deformation zones.

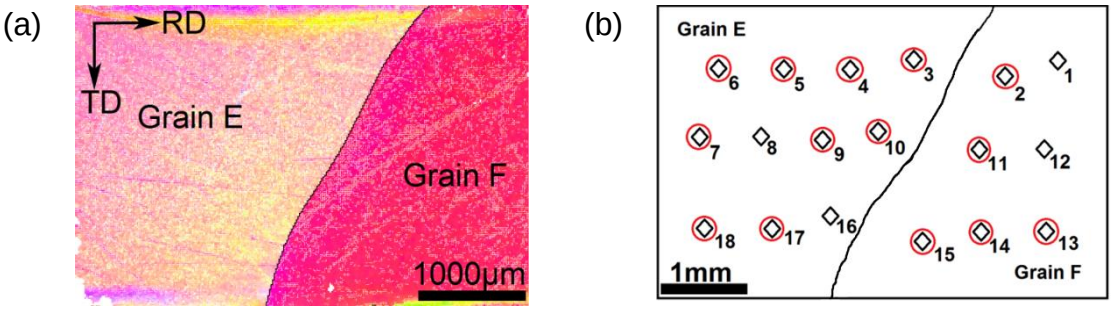

Figure 4.1: (a) EBSD map showing the grain boundary between Grain E and Grain F. (b) Sketch of the hardness indentations in the sample containing Grain E and Grain F. The diamonds in (b) indicate the indentations and the indentations that are found to stimulate nucleation are marked with red circles.

All samples were kept in a freezer when not in use. Also, all samples were wrapped in baking papers before annealing to avoid damages during the sample handling. All the annealed samples were characterized using ECC/EBSD to detect nuclei and by EBSD to measure the orientations of the nuclei and their surrounding matrix. Only some pixels can be indexed by EBSD within the indentations because of the difference in surface height. For the

indentations for which the EBSD data were not sufficient, ECC was used to check if nucleation occurred at the indentations. ECC was also used to measure the length of the diagonal lines of the indentations to calculate the hardness values according to equation 2.1.

It should be noted that twins within a nucleus are not counted as separate nuclei here. If two neighboring nuclei are twin related to each other and one of them has special relationships, such as misorientation angles below 15°, 40°<111> or 60°<111>, to the deformed matrix, this one is considered as a nucleus while the other one is not counted as a nucleus. If both of them have no special relationships to deformed matrix, the one with the larger size is counted as a nucleus.

4.2 Nucleation at samples cold rolled to 20%

4.2.1 Experimental details

Four samples were cut from the 20%-sample. Indentation loads of 500 g and 2000 g were used to ensure deformation higher enough to stimulate nucleation. Three of the samples were annealed at 300 °C for 1 h to the beginning of recrystallization. The step size of the EBSD measurement used to characterize the annealed microstructures near indentations at the sample surfaces was 2 µm.

In order to characterize the deformation zone around the indentations, the last sample was not annealed but ground first to reveal the tip of a 500 g indentation and then further ground to reveal the tip of a 2000 g indentation. After each grinding, the sample was mechanical polished using 40 nm oxide polishing suspension and characterized using EBSD with a step size of 0.35 µm.

4.2.2 Nucleation potentials

In total, 36 hardness indentations were done on the 3 annealed 20%-samples. 53 nuclei are detected at 27 indentations based on EBSD maps and an additional 5 nuclei that could not be observed by EBSD are detected around an

additional 4 indentations by ECC. Figure 4.2 is an example where ECC reveals a nucleus that could not be seen by EBSD. 15 indentations stimulate one nucleus, and 8 indentations stimulate two nuclei. Further 8 indentations are found to form 3 or more nuclei. All nuclei have grown into relatively large sizes ranging from tens of micrometers to 300 µm. It should be noticed that no nuclei are detected away from the indentations. This result clearly shows the potentials of indentations to act as nucleation sites, due to the extra driving force provided by the indentation. This agrees with previous investigations [19, 130].

The indentations are classified into two types ($I_{20/2000}$ and $I_{20/500}$) according to the indentation load, as shown in table 4.1. The table reports the total number of indentations and those that have stimulated nucleation. Compared with Type $I_{20/500}$ indentations, Type $I_{20/2000}$ indentations stimulate more nuclei, which is related to the more severe deformation after the higher load.

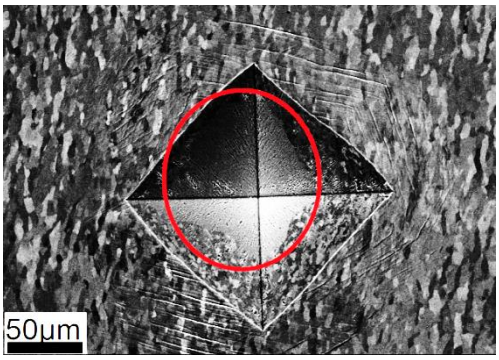

Figure 4.2: An ECC picture showing one nucleus (marked with a red circle) at a 2000g indentation in a 20%-sample after annealing at 300 °C for 1 h. Reproduced from article B.

Table 4.1: Survey of nucleation results for 2000 g and 500 g indentations.

Type	Loads of indenting	Number of indents	Number of indents with nuclei	percentage
$I_{20/2000}$	2000 g	18	18	100%
$I_{20/500}$	500 g	18	13	72%

4.2.3 Orientation relationships between nuclei and their surrounding matrix at the sample surfaces

Whereas much previous work in agreement with the present results have shown preferential nucleation at hardness indentations, far less work has been devoted to orientation relationships between nuclei and matrix. In the present work, the misorientations between the nuclei and their surrounding matrix at 27 indentations stimulating nucleation are analyzed based on EBSD. Table 4.2 summarizes the results. 11 out of 41 (27%) nuclei at Type $I_{20/2000}$ indentations have misorientation angles lower than 15° to their neighboring recovered matrix, while 33% of the nuclei at Type $I_{20/500}$ indentations have misorientation angles lower than 15°. One example at a Type $I_{20/2000}$ indentation is shown in figure 4.3. For this example only some pixels are indexed by EBSD. We can however still, clearly identify these nuclei, which are numbered as N*i* (*i*=1-3). The boundaries between N1 and G1 (the matrix) are composed of both low angle (LABs) and high angle boundaries (HABs). Since some of the boundaries are LABs, N1 is categorized within the group of nuclei with orientations near the matrix (which amounts to 27%).

Table 4.2: Orientation relationships between nuclei and surrounding matrix at two types of indentations.

Type	Number of nuclei	Number of nuclei with misori. ≤ 15°	Number of nuclei with misori. ≥ 15°
$I_{20/2000}$	41	11 (27%)	30 (73%)
$I_{20/500}$	12	4 (33%)	8 (67%)
Total	53	15 (28%)	38 (72%)

The remaining nuclei, i.e. the 73% nuclei around Type $I_{20/2000}$ indentations, and 67% nuclei around Type $I_{20/500}$ indentations only form HABs with the recovered matrix. For example, both nuclei N2 and N3 have only HABs to the surrounding recovered matrix (see figure 4.3). Therefore, one may speculate if these nuclei (as N2 and N3) have formed with a new orientation relative to the matrix.

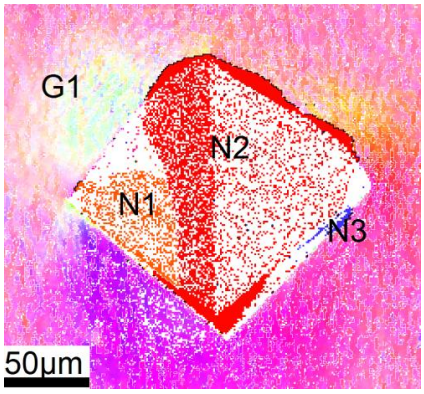

Figure 4.3: An EBSD map (without any noise reduction) showing 3 nuclei at a 2000 g indentation in 20%-sample. Reproduced from article B.

4.2.4 The correlation of nucleation with deformation microstructures near the indentation tips

As always with 2D static investigations, it is impossible to pinpoint the orientation relationship between a nucleus and the matrix in which it forms, because when inspecting the sample, the relevant matrix is consumed by the nucleus [21]. Although a large fraction of the nuclei reported above after some growth has orientations very different from the surrounding matrix, it does not necessarily mean that these nuclei have been formed with new orientations different from those at the nucleation sites in the deformed matrix.

To investigate that further, one grain from the remaining other half of the non-annealed 20%-sample, having the same initial orientation as the example shown in figure 4.3, was chosen to check the deformation microstructures around a 500 g indentation tip and a 2000 g indentation tip in the deformed state. The microstructures within an area of 85×85 μm^2 around both indentation tips were characterized by EBSD. The {111} pole figures for the microstructures at the 500 g and the 2000 g indentation are shown in figure 4.4. A large orientation spread in the deformed matrix around both the 500 g and the 2000 g indentation tips is observed, revealed as grey clouds in figure 4.4. It can be also noticed that the scatter of the deformation matrix around the 2000 g indentation tip is larger than that around the 500 g indentation tip.

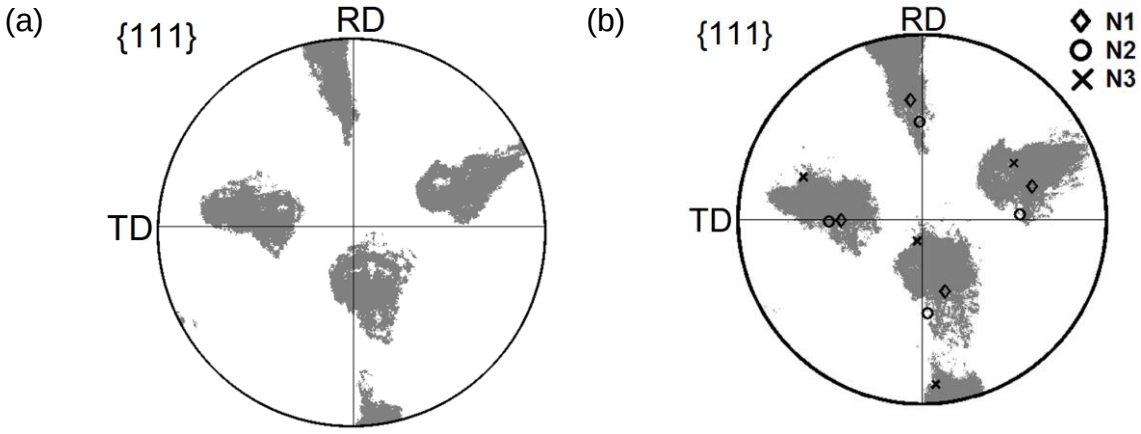

Figure 4.4: (a) and (b) {111} pole figures showing the orientations within an area of 85×85 μm^2 around the tip of a 500 g and a 2000 g indentation in the deformed state of a 20%-sample, respectively. The grey clouds represent the orientations of the deformed matrix. The orientation of the 3 nuclei, N1, N2 and N3 are shown in diamonds, circles and crosses. (b) is reproduced from article B.

The measured orientations around the indentation tips at both the 500 g and the 2000 g indentations are shown in figure 4.5(a) and (b).The figures reveal the largely symmetric distributions of orientations given by the pyramidal shape of the indenter. The orientation distributions near the indentations may also be visualized with respect to the orientation in the matrix away from the indentation, as misorientation to the matrix. This is shown in figure 4.5(c) and (d). In these figures, the matrix away from the indentation has more or less the same orientation and thus appears largely blue i.e. with misorientations below 15°. Most of the indentation zones both after 500 g and 2000 g load are rotated between 10° and 30° away from the matrix, and are thus shown in green in figure 4.5(c) and (d). Small local zones near the tip and along the symmetry axes, however, have misorientations to the matrix above 35°; most pronounced after the 2000 g indentation where a series of misorientation peaks above 40° are seen along a symmetry axis (see figure 4.5(d)). The largest rotation angles are ~50° and ~35° at the 2000 g and 500 g indentations, respectively. Upon annealing, these peaks will provide higher driving force for the formation of

nuclei, and nuclei formed here will readily be surrounded by HABs. Such peaks are therefore expected to be powerful nucleation sites [3].

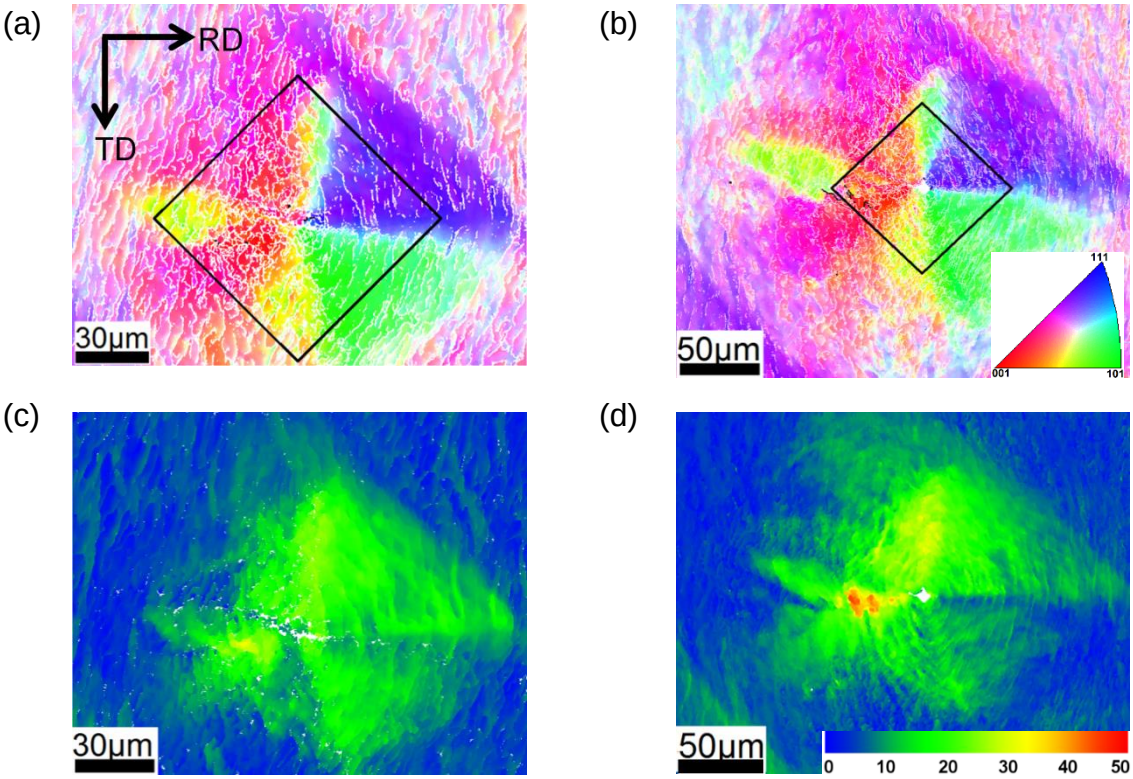

Figure 4.5: The deformation microstructures around a 500 g indentation (a, c) and a 2000 g indentation (b, d) in a 20%-sample. The color in (a) and (b) is defined by inverse pole figure color and the color in (c) and (d) is given by the misorientation angle between each pixel and the orientation in the 20% rolled matrix away from the indentation. The black diamonds show the regions used to calculate the stored energy. Reproduced from article B.

It is clear that the indentations lead to significant extra deformation and consequently extra driving force which has to be considered when studying nucleation. This is investigated in detail for both the 500 g and the 2000 g indentation in the following. The extra driving force in the form of SE introduced by the indentations may be estimated based on the EBSD measurements. Such estimation relies on the measured misorientations across deformation-induced boundaries using following equations [151]:

$$SE = \frac{\Delta}{A}\sum_{i}^{N}\gamma_i\left(\theta_i\right), \tag{4.2}$$

where Δ and *A* are the step size and the area mapped, respectively, *N* is the total number of misorientation segments above 2°, and γ_i is the boundary energy estimated from the Read-Shockley function according to the misorientation angle across boundaries.

This method for estimation of the stored energy is able to give a value for the local stored energy on the scale of individual map pixels, and therefore with a spatial resolution is limited by the EBSD step size. A low cut-off, 2° here, is used to limit the influence from orientation noise in the EBSD data. Contributions from individual boundaries, which are assumed to exist wherever a pixel-to-pixel misorientation larger than the low cut-off, are calculated directly.

For this estimation an area near the tip is used (marked by the diamond in figure 4.5(a) and (b)). For the 500 g indentation, a diamond with size of 120 μm along the diagonals is chosen to almost cover the region with large misorientation (the green area in 4.5(c)). The two diamonds in 4.5(a) and (b) are chosen to be the same for the 500 g and 2000 g indentations to allow a direct comparison of SE at this central indentation zone in the two cases. The calculated results are 0.12 MJ/m^3 and 0.15 MJ/m^3 for the 500 g and 2000 g indentations, respectively. The SE in an area of the same size away from the indentation is only 0.04 MJ/m^3.

The orientations of the nuclei N1-N3 are also plotted in figure 4.4(b) as diamonds, crosses and circles, respectively. When comparing these orientations with the orientation spread at the indentation tip in the deformed state, it is clear that N1 (marked by diamonds) has an orientation well within the deformed orientation spread, while N2 (marked by circles) and N3 (marked by crosses) both are at the outskirts but yet within the orientation spread in the deformed state. It is thus very likely that these 3 nuclei have nucleated from sites near the indentation tip with an orientation already present there, i.e. they form with an orientation as the deformed matrix and grow to meet new areas with different orientations, thereby forming HABs (and as N2 and N3).

Besides the nucleation sites and the orientation relationship between nuclei and matrix, another important aspect is the potentials for growth once the nuclei have formed. The potentials for the growth of the nuclei depend on the misorientations between the nuclei and the surrounding matrix. Figure 4.6 shows the distribution of the maximum misorientation angles between the nuclei, and their surrounding recovered matrix. It can be observed that the misorientation angles for nuclei at type $I_{20/500}$ indentations concentrate in the range of 20°~ 30° and do not exceed 35°, while for nuclei at type $I_{20/2000}$ indentations, the misorientation angles spread widely from 10° to 50°. This is corresponding to the misorientation relationships between the nuclei and the surrounding matrix that would be observed if the nuclei have formed at the misorientation peaks along the symmetry lines (see figure 4.5) and grown into the matrix.

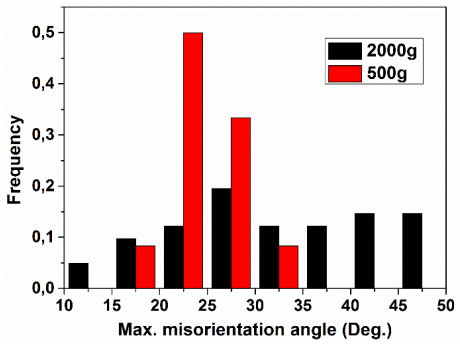

Figure 4.6: Maximum misorientation between nuclei and the surrounding pixels in the recovered matrix. The red and black histograms represent the data for the 500 g and the 2000 g indentations in the 20%-samples, respectively.

4.3 Nucleation at samples cold rolled to 12%

4.3.1 Experimental details

Ten samples sized 6.0 × 4.0 × (0.7~1.3) mm^3 were cut from the 12%-sample. In total, 14 large grains with different orientations (marked A to N) were selected in these samples. Three of the 10 samples only contained Grain N, each of which were indented with two loads, 500 g and 2000 g. The remaining 7 samples containing Grain A-M were indented only with a load of 500 g. For all samples,

the deformation microstructures of each grain (A-M) were characterized far away from indentations.

Table 4.3 reports experimental details for each sample. One sample only containing Grain E was serial sectioned to investigate the deformation microstructures near a hardness indentation. 9 samples were annealed and then characterized using EBSD/ECC to detect nuclei and by EBSD to measure the orientations of the nuclei and the surrounding matrix with a step size of 2 μm.

The results of the 5 samples annealed at 310 °C for 1 h will be discussed in section 4.3.2 to analyze orientations of nucleation at hardness indentations. The results of the sample annealed at 310 °C for 2 min, and serial sectioning results will then be reported in section 4.3.3 to discuss potential nucleation sites. Finally, the nucleation at Grain N will be compared with nucleation in the 20% sample.

Table 4.3 An overview of the indenting and annealing conditions of the 12%-samples.

The number of samples	Original grain(s)	Indent on load (g)	Annealing/ other
1	E	500	310°C/2min
1	E	500	Serial sectioning
5	A-M	500	310°C/1h
3	N	500/2000	300°C/1h

4.3.2 Orientation analysis of nucleation at hardness indentations

It is well acknowledged that the initial orientations of the grains have strong effects on the deformation microstructures and the SEs [47, 59] and it is thus likely also to have marked influence on the driving force for recrystallization near indentations, in particular on the nucleation potentials here. The five samples (500 g) initially containing 13 large grains named Grain A-M were annealed at 310 °C for 1 h. It is thus possible to investigate effects of the orientations of the initial grains on nucleation at hardness indentations.

4.3.2.1 Deformation microstructures far away from indentations

The deformation microstructures of all the 13 grains far away from indentations were first characterized using EBSD. The average orientation of each grain was recorded (see table 4.4). The orientation spreads within the grains were determined based on the EBSD maps and the values are also reported in table 4.4. Similar to previous observations [59], most grains contain extended planar dislocation boundaries, while some grains only reveal cell structures.

Table 4.4 Overview of the nucleation behavior in the 13 grains investigated. The hardness is averaged over all indentations in that grain and the nucleation potentials are given as indents leading to nucleation (in number and pct.). The data refer to surface observations. Ave. ori.: average orientations far away from indentation; Ori. spread: orientation spread far away from indentations; Ave. Hv: average hardness value of each grain (Kgf/mm^2); No.1: the number of indents; No.2: the number of indents with nuclei; %: nucleation percentage. Reproduced from article C.

Grain	Ave. ori.	Ori. spread	Ave. Hv	No. 1	No. 2	%
C	(114) [31-1]	2.2°	27.3	6	6	100%
D	(215) [-120]	1.8°	24.0	2	2	100%
H	(113) [0-31]	1.3°	23.8	6	6	100%
E	(3-1-1) [215]	1.6°	25.2	11	9	82%
I	(137) [-131]	1.7°	26.6	7	5	71%
F	(-5-11) [116]	1.3°	20.3	7	5	71%
B	(126) [-12 31]	1.8°	21.3	3	2	67%
J	(1 1 10) [73-1]	0.9°	18.4	18	2	11%
L	(123) [-301]	1.1°	23.6	9	0	0
A	(001) [310]	1.3°	20.2	7	0	0
M	(001) [-1-40]	0.9°	19.2	9	0	0
K	(51 14) [24-1]	1.7°	19.0	18	0	0
G	(016) [10 6 -1]	0.5°	18.2	5	0	0

Figure 4.7 shows the ECC images at different magnifications revealing the deformation microstructures far away from indentations in Grain E. The structure is subdivided by one set of deformation bands elongated along the along the transverse direction (TD) and the width of each band is in the range of a few micrometers to 15 µm. The microstructural subdivision can be also visualized by the deviation (misorientation) to the average orientation of the

measured area: figure 4.8(a) and (b) are colored according to the misorientation angle and misorientation axis, respectively. It can be seen that within each band, many small color changes are seen corresponding to small variations in orientation. The misorientation angles are rather small; mostly in the range of 0° - 3° and do not exceed 5°. The mean orientation spread of this area is 1.6°. The pole figure (figure 4.8(c)) also reveals the relatively small orientation spread.

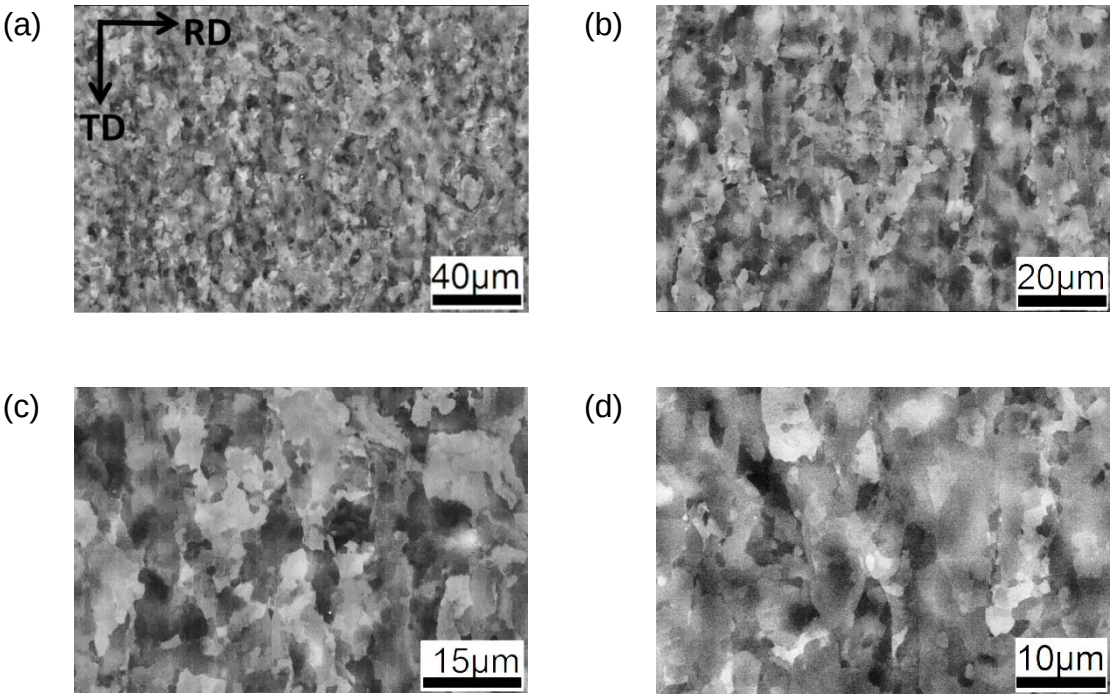

Figure 4.7: ECC images at different magnifications of the deformation microstructures of Grain E far away from indentations.

An example of a grain with a cell structure (Grain A with an orientation near cube orientation) is shown in figure 4.9. Many small color changes are seen corresponding to small orientation changes, which are similar in magnitude to those in Grain E. Together these observations agree well with what has been observed before in aluminum cold rolled to low strains [47]. The orientation spread is larger for Grain C, D, E, I and B than for Grain J, M and G.

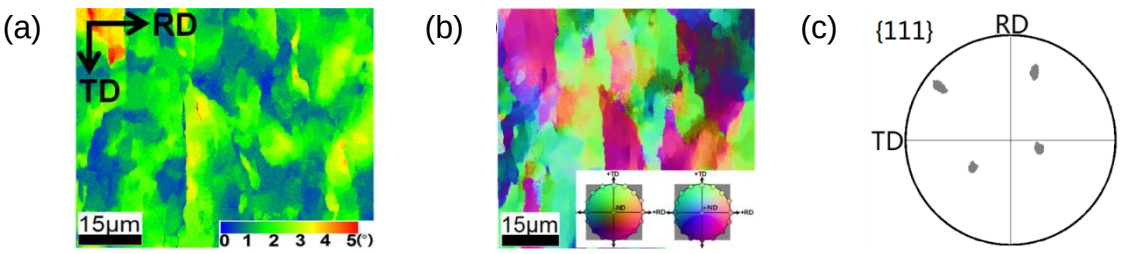

Figure 4.8: (a) and (b) EBSD maps of the deformation microstructures of Grain E far away from indentations. The color of each pixel in the EBSD maps is given by the orientation deviation (misorientation) from the average orientation of this map: (a) misorientation angle and (b) misorientation axis. (c) {111} pole figure showing the orientations within the characterized area. (b) is reproduced from article C.

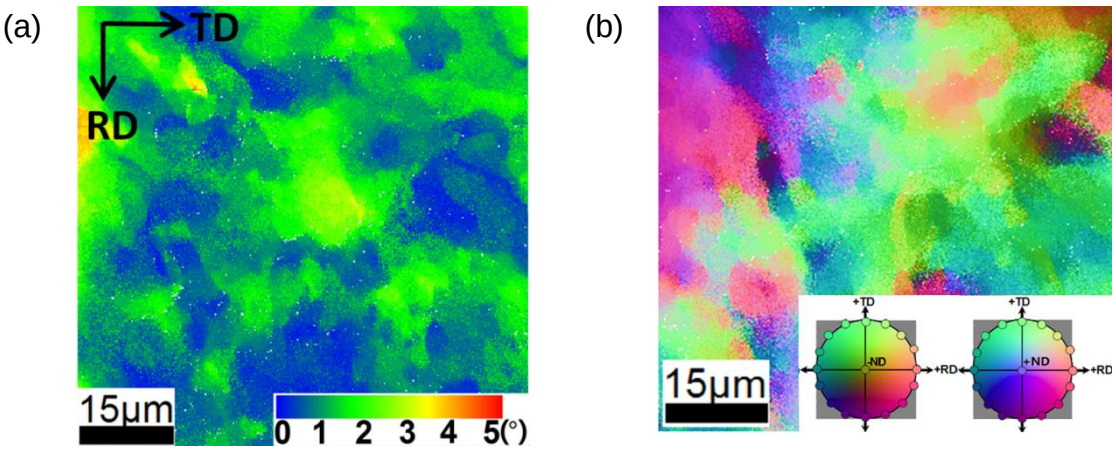

Figure 4.9: EBSD maps of the deformation microstructure of Grain A far away from indentations. The color of each pixel in the EBSD maps is given by the orientation deviation (misorientation) from the average orientation of this map: (a) misorientation angle and (b) misorientation axis. (b) is reproduced from article C.

The initial orientations of the grains are expected to affect the hardness as it will affect the evolution of the deformation microstructures. For the present 13 grains this is validated by relating the measured hardness to the energy stored in the rolled deformation microstructures: The SE within each rolled grain was calculated based on the measured misorientations across the dislocation boundaries using the method described in section 4.2.3 [151], including all boundaries with misorientations ≥ 2°. Figure 4.10 shows the hardness values as a function of the SEs. It can be seen that the grains with higher SEs also have

higher hardness values as expected. The scatter within each grain in the results is likely to be a consequence of the local inhomogeneity within the grain.

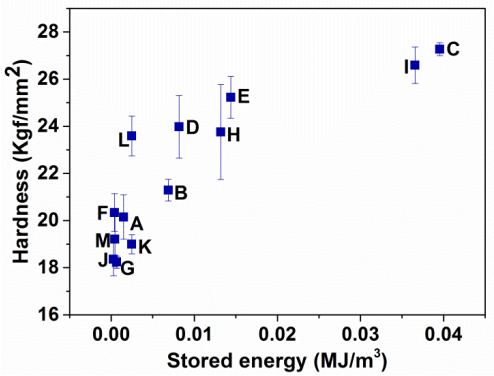

Figure 4.10: The hardness values of all 13 grains as a function of the stored energy in the rolled microstructures measured far away from indentations. Reproduced from article C.

4.3.2.2 Nucleation potentials at indentations in grains of different orientations

In total 108 hardness indentations were done in the 13 grains (A - M) and 37 of them in 8 grains are observed to stimulate nucleation as seen by EBSD maps at the sample surface. Most of the 'nucleating indentations' stimulate one nucleus while 9 indentations stimulate 2 nuclei. No nucleus is detected away from the indentations. Table 4.4 gives an overview of the nucleation observed within all the 13 grains. All grains that do not stimulate nucleation have cell structures, except Grain L. The grains having lower orientation spread, such as Grain J, M and G, have low nucleation probabilities.

4.3.2.3 Orientation relationships between nuclei and the surrounding matrix

The microstructures around the nucleating indentations were analyzed using EBSD and the orientation relationships between nuclei and the surrounding matrix are determined. Table 4.5 reports the details. In total, 24 (53%) nuclei have misorientation angles below 15° to the surrounding recovered matrix (old orientations). The other 21 nuclei (47%) form only HABs to the surrounding

recovered matrix (new orientations). The misorientation angles between the nuclei and the surrounding matrix spread widely from 15° to 45° with most of them up to 30°. 17 of them have a common rotation axis around a <100> axis, 3 around a <111> axis, while one is rotated around a <120> axis.

Table 4.5 Misorientation angles between the nuclei and the surrounding recovered matrix.

Group	Sample No.	Nucleus No.	Misori.
Old orientation	B	N1	12° to 17°
		N2	10° to 22°
	C	N1, N2, N3a, N4b, N5a, N6a	≤ 15°
	D	N1	≤ 15°
	E	N17	12° to 20°
	F	N2	11° to 20°
		N3	14° to 26°
		N4	4° to 26°
	H	N1, N2, N5	≤ 15°
		N3	12° to 28°
		N4	13° to 26°
	I	N1, N2, N5	≤ 15°
		N3b	11° to 21°
	J	N1	≤ 15°
		N2b	10° to 20°
New orientation	C	N3b	15° to 25° <100>
		N4a	18° to 32° <100>
		N5b	15° to 26° <100>
		N6b	22° to 32° <100>
	D	N2	16° to 30° <100>
	E	N3	26° to 36° <100>
		N6	25° to 43° <100>
		N7a	19° to 30° <100>
		N7b	26° to 40° <100>
		N4	17° to 35° <100>
		N5	24° to 40° <100>
		N9	24° to 38° <111>
		N10	17° to 24° <100>
		N18	21° to 45° <111>
	F	N1a	17° to 27° <100>
		N1b	16° to 33° <120>
		N5	21° to 35° <100>
	H	N6	22° to 31° <100>
	I	N3a	16° to 24° <100>
		N4	15° to 35° <100>
	J	N2a	19° to 30° <111>

One example is shown in figure 4.11. The nucleus, numbered as N17 (which has developed at indentation No. 17 in figure 4.1(b)), forms both LABs and HABs to the surrounding matrix. As can be seen in the pole figure, its orientation is at the outskirt but still within the orientation spread of the surrounding matrix. N17 is one of the 24 nuclei which have an orientation similar to the neighboring matrix at the sample surface.

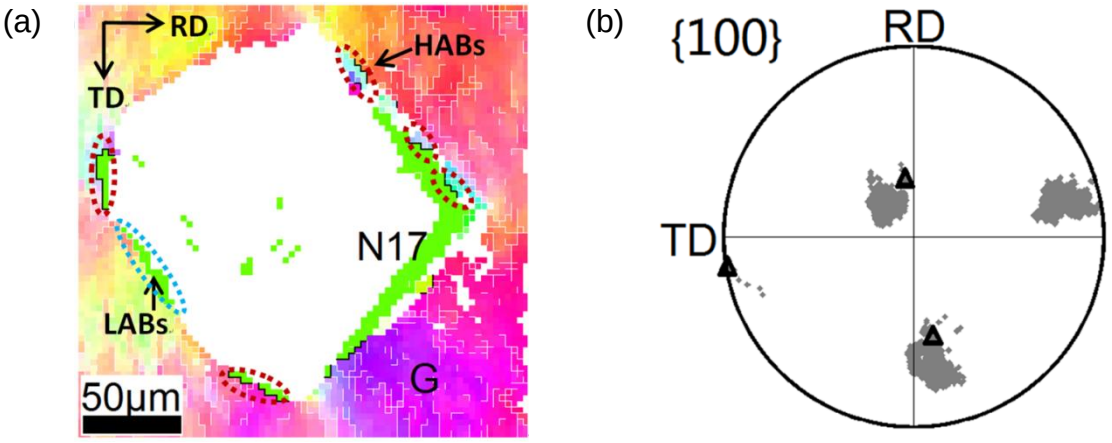

Figure 4.11: (a) EBSD orientation map and (b) {100} pole figure of the recovered matrix and the nucleus N17 (the nucleus formed near indentation No. 17 in Grain E). The grey 'cloud' in the pole figure represents the orientations within the recovered matrix G and the triangles show the orientation of the nucleus N17. The color of each pixel in the map (a) is defined by the crystallographic orientations along the sample normal direction, LABs (2-15°) and HABs (>15°) are shown by thin white and thick black lines, respectively.

An example of a nucleus with only HABs to the surrounding recovered matrix (indentation No. 7 in figure 4.1(b)) is shown in figure 4.12. At this indentation, two nuclei numbered N7a and N7b are observed and both of them are fully surrounded by HABs. The {100} pole figure (figure 4.12(b)) shows that the nuclei are rotated 25° to 40° around a common <100> axis relative to the matrix. Thus these nuclei have orientations different from the matrix at the surface. It can be noticed that the boundaries between N7a and N7b are composed of only LABs. Also the pole figure shows that the 2 nuclei have very similar orientations (see figure 4.12).

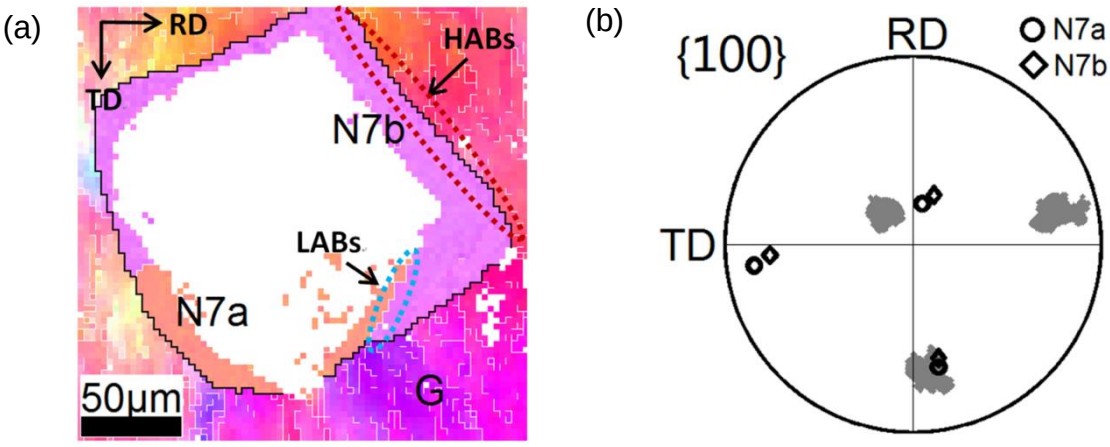

Figure 4.12: (a) EBSD orientation map and (b) {100} pole figure of the recovered matrix and the nuclei N7a and N7b formed at Grain E. The grey 'cloud' in the pole figure represents the orientations within the recovered matrix G and the circles and the diamonds show the orientations of the nuclei N7a and N7b, respectively. The color code in (a) is same as that in figure 4.11(a).

4.3.2.4 Orientation relationships among the nuclei

It is of interest to investigate whether the nuclei developed within one grain but at different indentations have similar or different orientations. This is only relevant to do for grains which stimulated many nuclei i.e. grains C, E, H, I and F.

The orientations of all nuclei observed in Grain E after annealing at 310 °C for 1 h are plotted in a pole figure in figure 4.13. It can be seen that the orientations of the nuclei are not identical, but also not very different. They are clustered within a limited region of the pole figure. The misorientations between all the nuclei are calculated. Of the 10 nuclei formed at Grain E, 7 have at least one other nucleus with an orientation that are misoriented less than 15° to it. Table 4.6 reports the details. These nucleus-nucleus misorientations are small compared with the misorientations between the nuclei and their surrounding recovered matrix. For example, the misorientation angles between N7a and N4, N7b and N5 are only 3.9° and 2.7° respectively, while the misorientations between these nuclei and their surrounding matrix are in the range 17°～40°.

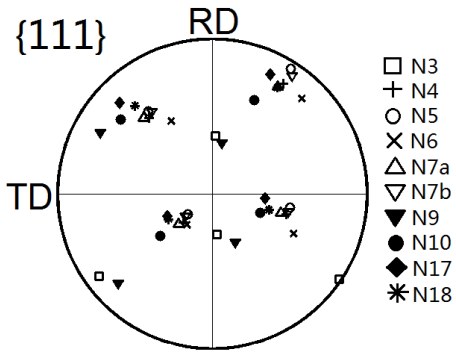

Figure 4.13: The orientation distribution of all nuclei developed near indentations in Grain E after annealing at 310 °C for 1 h. The number refers to the indentation number.

Table 4.6 The orientation relationships among the 1-h nuclei at Grain E

Nucleus (Grain E)	Correlation between nuclei
N3	Non
N6	N4 (12.3°) N7b (12.8°)
N7a	**N4 (3.9°)** N5 (8.9°) N7b (7.4°)
N7b	**N4 (4.4°) N5 (2.7°)** N6 (12.8°) N7a (7.4°)
N4	N5 (6.4°) N6 (12.3°) **N7a (3.9°) N7b (4.4°)**
N5	N4 (6.4°) N6 (8.9°) **N7b (2.7°)**
N9	N18 (6.6°)
N10	Non
N17	Non
N18	N9 (6.6°)

Similarly, the nuclei within grains C and I are also scattered but still far from random, as shown in figure 4.14. The orientations of the nuclei in Grains F and H appeared to be less scattered (see figure 4.15), but this may be an effect of statistics: only 6 nuclei were observed in these grains.

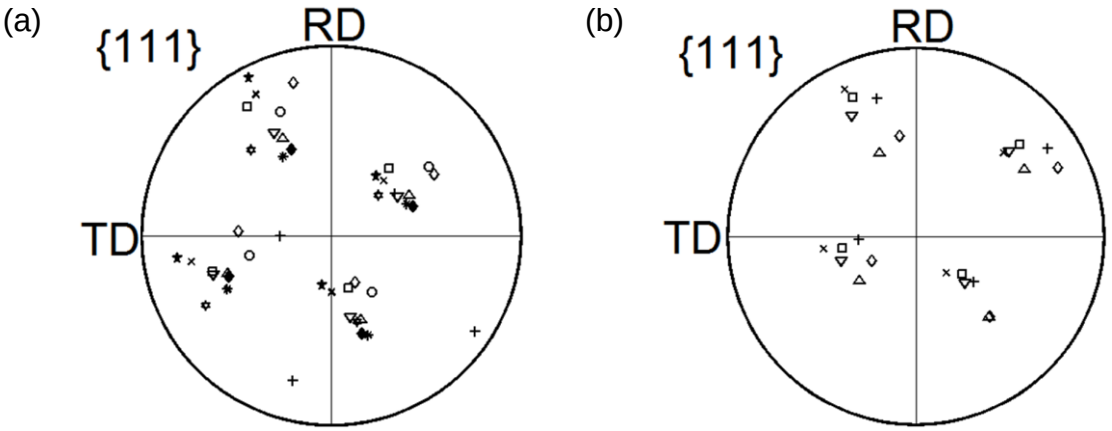

Figure 4.14: Orientation distributions of the nuclei formed at (a) Grain C and (b) Grain I. Different markers in each figure represent different nuclei.

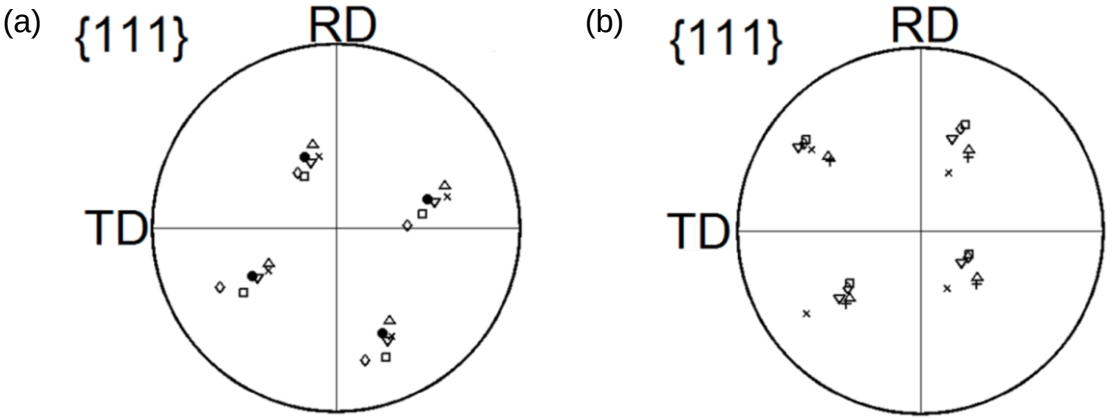

Figure 4.15: Orientation distributions of the nuclei formed at (a) Grain F and (b) Grain H. Different markers in each figure represent different nuclei.

4.3.2.5 Correlation of nucleation potentials to hardness values

The SE in the deformed matrix is known to provide the driving force for nucleation and growth during recrystallization. As shown above it is relatively straightforward to determine the SE at locations far away from the indentations, but as it is the hardness indents that are found to be the preferential nucleation sites, also SEs there are needed. These energies cannot be estimated using 2D measurements because of the complicated 3D deformation volume underneath indentations. Generally one may assume, however, that a large indentation (small hardness value) means that the local volume under the indentation is in a

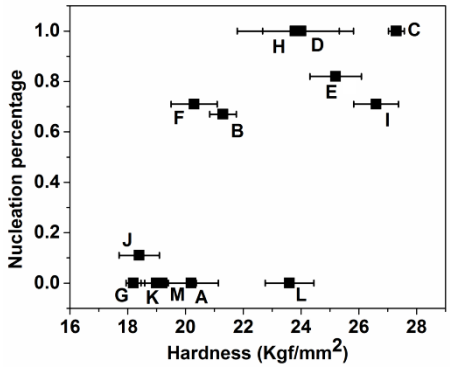

Figure 4.16: The nucleation potential expressed in percentages for all the 13 grains as a function of the average hardness values. Reproduced from article C.

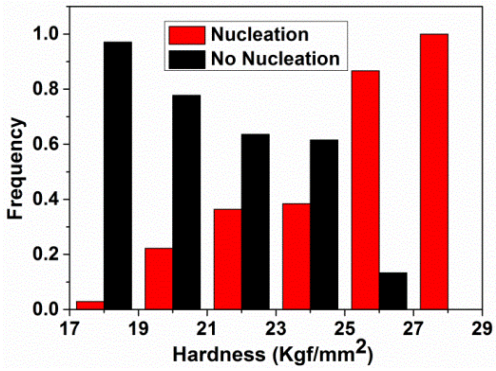

Figure 4.17: Nucleation frequency of indentations of different hardness values as a function of hardness values. The red and black histograms represent the indentations with and without nucleation, respectively. The data is based on 108 indentations, including all indentations at samples annealed at 310 °C for 1 h. Reproduced from article C.

state favorable for the indenting deformation, which in turn may lead to relative lower dislocation densities and thus lower SEs at that site. Based on this assumption, the hardness values are in the following related to the corresponding nucleation probabilities. Figure 4.16 shows the nucleation percentages for all the 13 grains as a function of hardness averaged over all indentations in that grain. Although there is a large scatter, the general trend is that the nucleation potential increases with increasing hardness values. To further investigate the possible relationship between hardness and nucleation potentials, figure 4.17 shows the nucleation percentages at all the hardness

indentations. The figure reveals a clear tendency that indentations with higher hardness stimulate more nuclei and vice versa.

4.3.3 Potential nucleation sites

4.3.3.1 Nucleation after short time annealing

Although some nuclei seen after annealing at 310 °C for 1 h only have HABs to the surrounding matrix, it does not mean that those nuclei have orientations different from the deformed matrix at sites where they form. According to the results of section 4.2, the nuclei might form near indentation tips with pre-existing orientations. To investigate that for the present samples, One sample containing Grain E was annealed at 310 °C for 2 min to further analyze where exactly the nuclei form and what orientations they have.

After annealing, it is observed by ECC that all indentations in the two samples have stimulated one or two nuclei. All the nuclei are in the range of several micronmeters to 30 μm in diameter, which is much smaller than the size of the indentations, and they are all located near the tips of the indentations. Some examples are shown in figure 4.18(a), (c) and (e). They are thus not visible by EBSD on the sample surface. Therefore, the sample was ground and electro polished to reveal areas below the surface, and then the orientations of the nuclei and the surrounding recovered matrix were examined using EBSD as shown in figure 4.18(b), (d) and (f).

In total, 4 small nuclei (to be called 2-min nuclei) numbered as n1, n2a, n2b and n3 (the numbers represent the indentation number, and the lower case n is used to signal that these nuclei developed after the short annealing time as opposed to the capital N for the long annealing time, 1 h), are observed at 3 indentations in this sample as shown in figure 4.18. It is found that all the four nuclei form both LABs and HABs to the recovered matrix and the misorientation angles between the nuclei and their surrounding recovered matrix span a range from 12° to 42°. The presence of misorientation angles below 15° indicates that

all these 2-min nuclei have similar orientations as the surrounding recovered matrix.

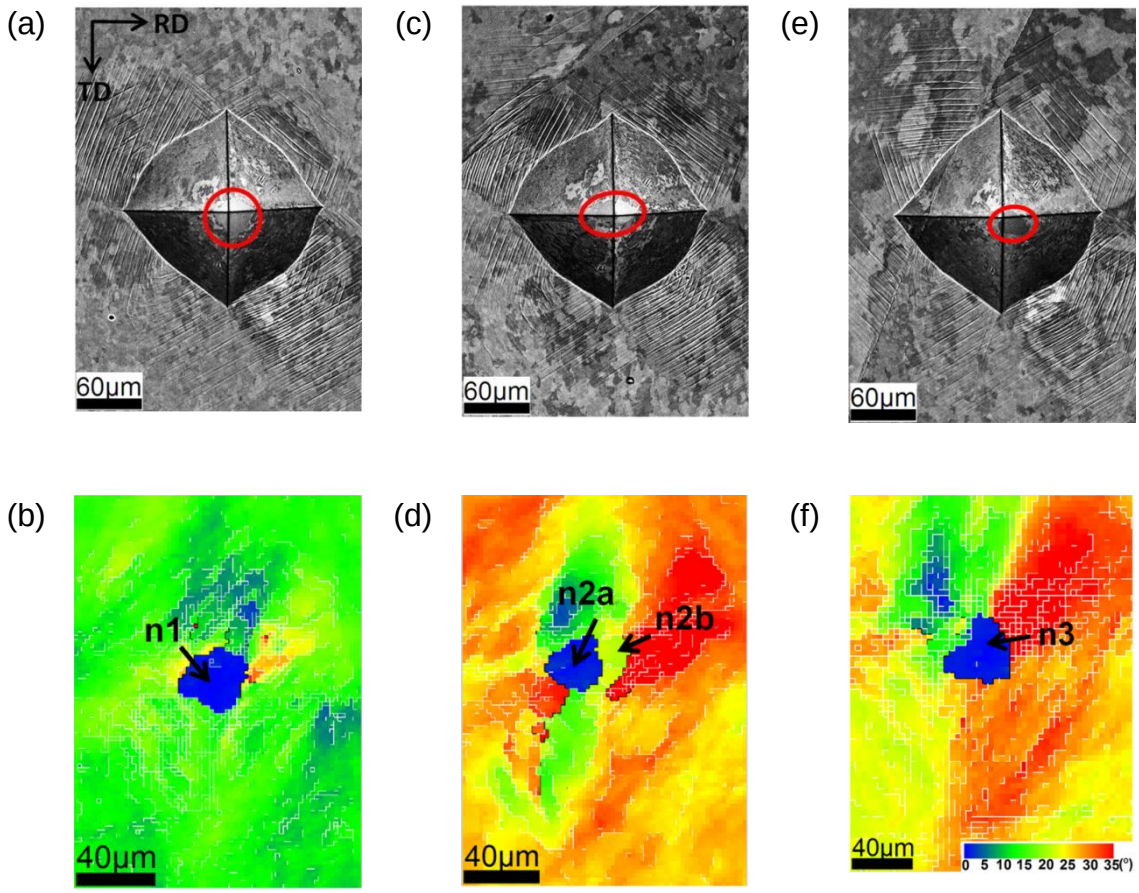

Figure 4.18: ECC images (a), (c) and (e) and EBSD maps (b), (d), and (f) of four nuclei formed near the tips of indentations in Grain E after annealing at 310°C for 2 min. The nuclei are marked by red circles and arrows in the ECC images and EBSD maps, respectively. In the EBSD maps, the white lines represent LABs (≥ 2° and < 15°), while the black lines represent HABs (≥ 15°). The color of each pixel in (b), (c) and (d) is defined by its orientation deviation from the orientation of the nucleus n1, n2a and n3, respectively. Reproduced from article C.

To compare the short and long time annealing, the orientations of all the 1-h and 2-min nuclei are plotted together in figure 4.19. It reveals that nucleus n3 has an orientation similar to nuclei N9 and N18 with a deviation of only 2.9° and 4.8°, respectively. Although the orientations of nuclei n1, n2a and n2b are not the same as any 1-h nuclei, their misorientation angles with nucleus N18 are

still relatively small, 13.9°, 10.5° and 15.9° respectively. Similar to the nucleation at samples cold rolled to 20% reduction, it is likely that the 1-h nuclei may have formed with orientations similar to the matrix at sites near the indentation tips, and have grown to meet new orientations at the surface of the samples.

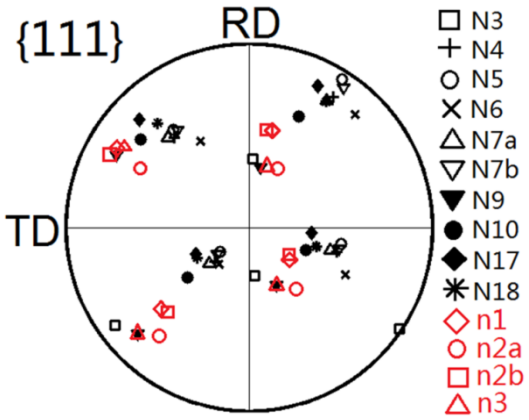

Figure 4.19: The orientation distribution of all 1-h and 2-min nuclei developed near indentations in Grain E. The number refers to the indentation number. The black and red markers represent the 1-h and the 2-min nuclei, respectively. Reproduced from article C.

This hypothesis is tested by looking at orientation relationships between the 2-min nuclei and the matrix far away from them – corresponding to the misorientation relationships that would be observed if they had been annealed to grow to a larger size as the 1-h nuclei. In the EBSD maps of figure 4.18, the color of each pixel is defined by its orientation deviation from the nucleus. It can be observed that the misorientation angles between the nucleus and the recovered matrix 80 µm away from the nucleus are lower than 15° (green in figure 4.18(b)), while in figure 4.18(d) and (f) almost all that misorientation angles are higher than 15° (red and yellow). Therefore, it can be expected from figure 4.18(b) that when the nucleus n1 grows into a size of about 160 µm, the misorientation between the nucleus and the surrounding recovered matrix will be smaller than 15° and LABs will at least partly surround the nucleus, which is similar to nucleus N17. In the same way, the nuclei n2a, n2b and n3 in figure 4.18(d) and (f) will form only HABs to the surrounding matrix, as all the other 1-h

nuclei with orientations different from the surrounding matrix. This is taken as support for the hypothesis.

4.3.3.2 Deformation microstructures near indentations

ECC images at different magnifications were used to characterize the deformation microstructures of Grain E on the sides of indentations, as shown in figure 4.20. It can be observed that the deformation microstructures on the four sides of the indentation are different from each other. This is as expected because the sides of the indenter push the sample against different crystal orientations and the deformation microstructures are thus expected to be different at different sides of the indentations.

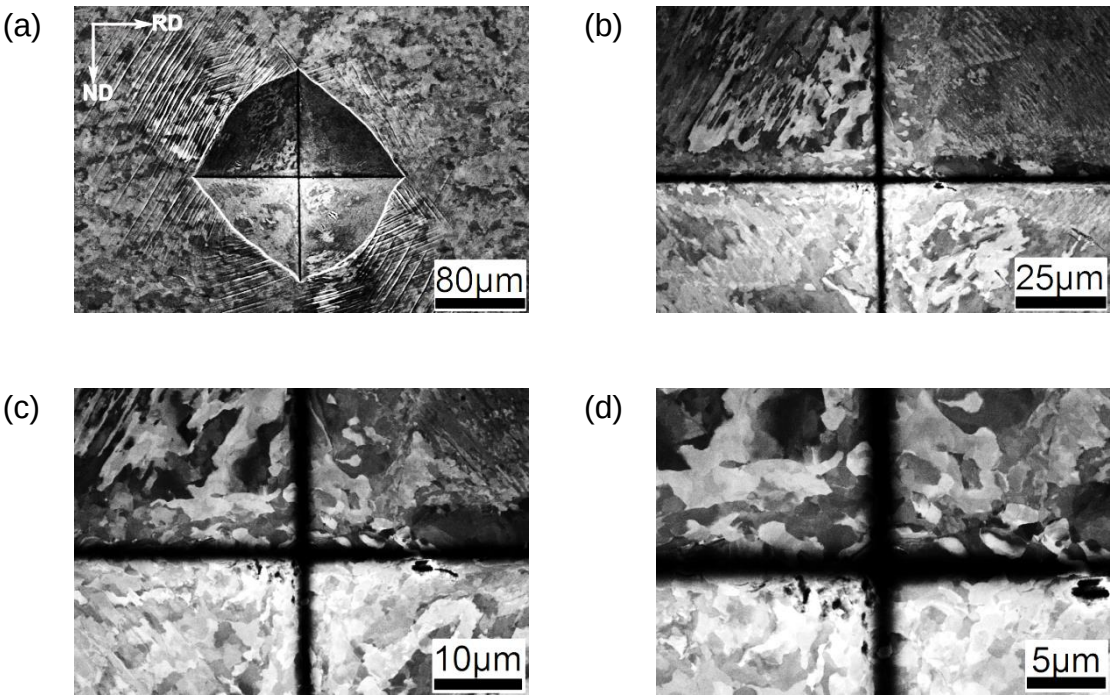

Figure 4.20: Deformation microstructures on the sides of a 500 g indentation in Grain E. In (a) focus is on the sample surface, while in (b), (c) and (d) it is near the tip.

Combined with serial sectioning, EBSD was used to inspect the deformation microstructures near an indentation in Grain E at 4 different depths. The sample surface section (0 μm), two middle sections (9 μm and 24 μm below the sample surface) and the section through the indentation tip (28 μm below the sample

surface) were characterized (see figure 4.21). In figure 4.21, the color of each pixel in the EBSD maps (a_1-d_2) is defined by its orientation deviation (misorientation) from the average orientation of the matrix far away from indentations (figure 4.8). Figures 4.21(a_1) - (d_1) represent misorientation angles and figures (a_2) – (d_2) show misorientation axes.

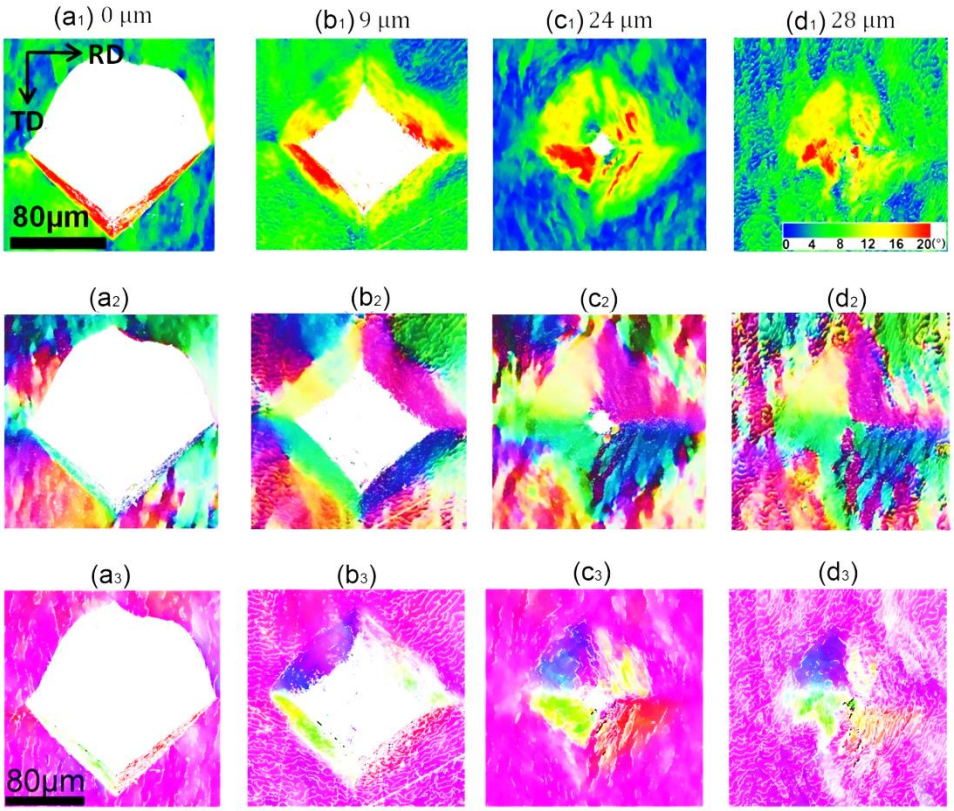

Figure 4.21: The deformation microstructures at an indentation in Grain E at different depth: (a) 0 µm (sample surface), (b) 9 µm, (c) 24 µm and (d) 28 µm (at the tip of the indentation) below the sample surface. The color of each pixel in the EBSD maps (a_1-d_2) is defined by the orientation deviation (misorientation) from the average orientation of the area marked in figure 4.8: (a_1-d_1) misorientation angles and (a_2-d_2) misorientation axes. The color code of the misorientation axis mapping is same as that in figure 4.8. The color of each pixel in maps (a_3-d_3) is defined by the crystallographic orientations along the sample normal direction. LABs and HABs are shown by thin white and thick black lines, respectively. (a_3-d_3) are reproduced from article C.

At the surface the angular orientation deviations are mostly in the range 0-8° (blue and green colors in figure 4.21(a_1)), which is larger than those in the areas

far away from indentations (figure 4.8(a)). Only very close to the indentation, deviation angles as high as 12° are observed at the surface layer. The indented zone under the sample surface (figure 4.21(b_1)-(d_1)) has larger orientation deviations. Like samples cold rolled to 20% reductions, misorientation peaks are observed near the sides of the indentation and near the indentation tip. The misorientation axes of the four different triangles of the indentation are observed to be different (as they appear in different colors in figure 4.21(b_2)-(d_2)). Even within the indented zones, subdivision into deformation bands as those seen far away from the indentations is also observed (see figure 4.21(d_2)). The spacing of the dislocation boundaries within the indentation zone is smallest at the section close to the indentation tip (see figure 4.21(d_3)), and more HABs form there.

4.3.3.3 The potentials of indentation tips as nucleation sites

The detailed analysis of the short-time annealing of Grain E suggests that the nuclei develop preferentially at sites near the indentation tip. This may be explained by the distribution of SE near the tip. As sketched in figure 4.22, the SE has been calculated for Grain E within rings around the tip position, using the same method as in section 4.2.4, and as described in [151]. Figure 4.22(b) clearly reveals that the SE is highest at the tip and decreases with increasing distance. This observed distribution of SEs agrees with a model developed by Nix and Gao [82] and with Swadener's results [83] (see equation (1.3)), in which the dislocation spacing increases, the dislocation density and SE decrease, with increasing distance from the central axis of the indentation. This lead to the highest density of geometrically necessary dislocations at the center of the indentation, which is in good agreement with figure 4.22.

Nucleation by coalesence [10, 11], strain induced boundary migration or subgrain growth [7, 9] would be facilitated by a high SE as well as by a gradient in SE. The latter would mean that areas with high SEs are preferential nucleation sites. In the work by Nix and Gao [82], the indented matrix was a perfect single crystal. The present samples were cold rolled before indenting and it therefore cannot be excluded that the local microstructures developed

during the rolling have an influence on the nucleation potentials at the indentations.

(a) (b)

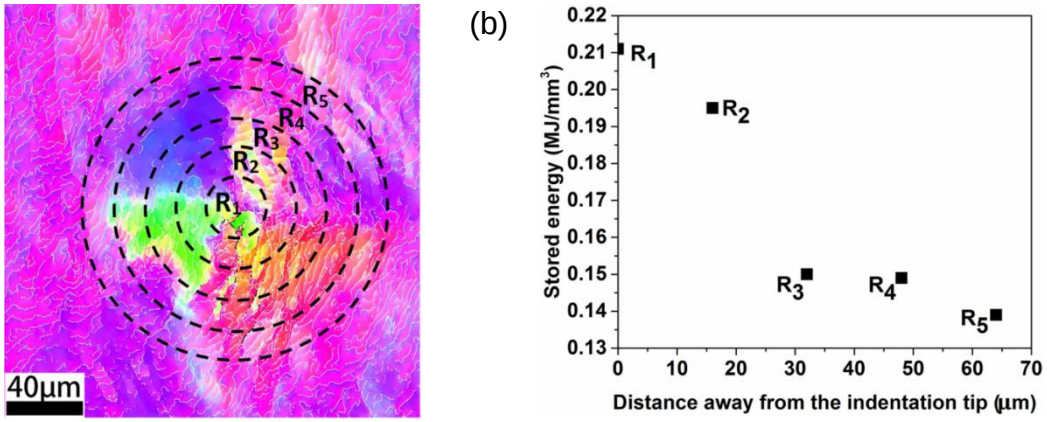

Figure 4.22: (a) EBSD maps (same as figure 4.21(d)) divided into regions, marked as R*i*, (*i*=1-5). (b) Stored energies of the areas in (a) as a function of the distance away from the indentation tip. Reproduced from article C.

4.3.3.4 Orientation relationships between nuclei and the deformed matrix

All the nuclei are observed near the hardness indentations. The nuclei that form at different hardness indentations within a given grain have related orientations. This is similar to what is observed in the 20% sample. Also in the 12% cold rolled sample, it is thus very likely that the orientations of the nuclei are related to the matrix in which they form. As discussed above the areas near the indentation tips appear to be the most potential sites where also the largest misorientations to the matrix are found (see figure 4.21(d)) and where the SE is the largest (see figure 4.22). This agrees with the detailed TEM investigations near Vickers indentation tips [128], which revealed severe deformation at the tips and along the diagonal lines. Upon annealing it has been observed by Granzer that big subgrains preferentially develop within these severely deformed regions [128]. In the present work, the short time annealing revealed nuclei only near the indentation tips (see section 4.3.3.1). It is thus of interest to evaluate possible correlations between the orientations of the nuclei and the orientations present at the areas near the tip. The serial sectioning of the deformed microstructures below an indentation allows for such an analysis.

For this analysis, the area near the indentation tip is divided into 4 parts: I, II, III and IV (see figure 4.23(a)). The orientations here and the orientations of all 1-h and 2-min nuclei found in Grain E are plotted in a <100> pole figure (see figure 4.23(b)-(e)). Figure 4.23(b)-(e) clearly reveals that the orientations of most of the nuclei are found within the orientation spread of region I and IV, and a few at the outskirts of the orientation spread of region III. Following the idea above concerning relationship between nucleation potentials and local SEs, also the SE within the I-IV regions are calculated. The result is 0.14 MJ/m^3, 0.04 MJ/m^3, 0.16 MJ/m^3, and 0.23 MJ/m^3 within the four regions respectively. The SE of region II is very low and no nuclei form there. Region I, III and IV have higher SE. Many nuclei form in region I and IV, while fewer in region III. By comparing the microstructures within regions I, III and IV (see figure 4.23(a)), it is clear that I and IV have banded structures with alternating orientations while region III appears more homogeneous. It is thus suggested that not only the SE but also the morphology of the deformation microstructure affect the nucleation potentials.

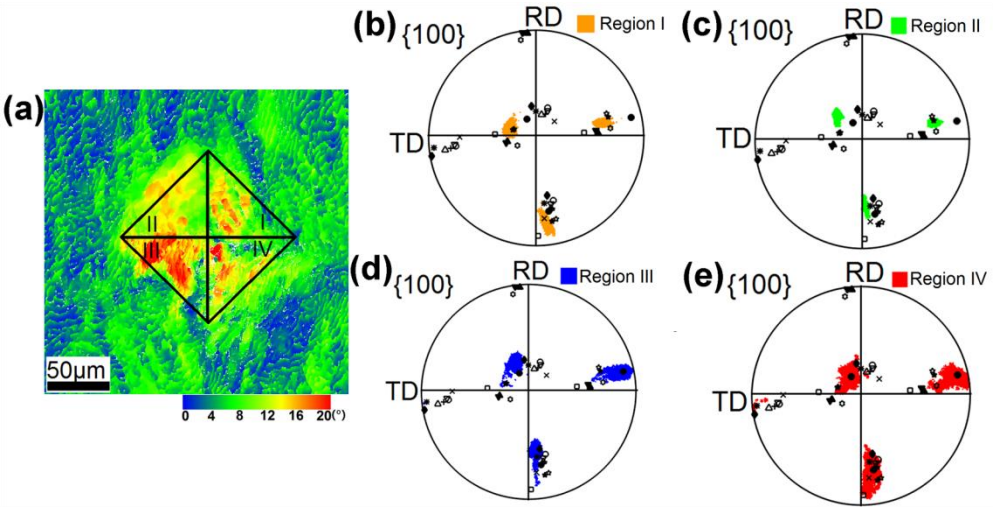

Figure 4.23: (a) EBSD map showing the regions of I, II, III and IV, and (b)-(e) {100} pole figures of all the 1-h and 2-min nuclei within the 4 regions: I - IV, in (a). Reproduced from article C.

The mechanism(s) leading to nucleation cannot directly be quantified from the present work. However as the nuclei appear to have orientations very similar to

those present at the active nucleation sites, conventional mechanisms such as coalescence [10, 11], SIBM [5, 6] or subgrain growth [7, 9] could explain the results. It should be noted that as no original GBs are present near the nuclei, the SIBM mechanism should refer to strain induced *dislocation* boundary migration for the present case.

As most of the nuclei characterized in the present work have grown to quite large sizes (the 1-h nuclei), it cannot be ruled out that possible preferential growth might have affected our results. For the present nuclei, it is however observed that the majority have a nearer 30º <100> than e.g. a 40º <111> misorientation relationship to the matrix far away from the indentation. As the 30º <100> misoriention is not expected to lead to fast boundary migration, preferential growth is however, not considered to be of major concern for the present result.

4.3.4 Effects of deformation amounts on nucleation

Out of the 14 grains in the 12%-samples, Grain N is the only one which was indented with two loads: 500 g and 2000 g. In total, 10 indentations with 2000 g load, termed Type $I_{12/2000}$ indentations, and 11 indentations with 500 g load, termed Type $I_{12/500}$ indentations, were done in Grain N. After annealing at 300 °C for 1 h, only one nucleus is detected at a Type $I_{12/2000}$ indentation (see table 4.7). Like the 20%-samples, also a higher indenting load leads to more nucleation here.

Table 4.7: Deformation modes and corresponding nucleation at 2 types of indentations in Grain N (Type $I_{12/2000}$ and $I_{12/500}$)

Type	Loads of indenting	Number of indents	Number of indents with nuclei	percentage
$I_{12/2000}$	2000 g	10	1	10%
$I_{12/500}$	500 g	11	0	0

As reported in section 4.3.2, of all the 108 indentations in 13 grains in 12%-samples, only 34% stimulate nucleation after annealed at 310 °C for 1 h (see table 4.4). When compared to the 20%-samples in which 31 out of 36 (86%)

indentations lead to nucleation after annealing at 300 °C for 1 h, it is clear that the rolling strain has a significant effect on the nucleation amount at the indentations.

4.4 Summary

The nucleation in weakly rolled aluminum further deformed locally by well distributed hardness indentations has been investigated. Different rolling reductions (12% and 20%), different indenting loads (500 g and 2000 g), different annealing time and temperatures as well as grains with different orientations have been investigated to evaluate effects here-of on nucleation. The results can be summarized as:

1. Indentations lead to substantial additional grain subdivision of the deformed microstructure and large orientation rotations near the indentations. The higher the indentation loads the larger are the subdivision and thus the local SE. It is therefore not surprising that nucleation occurs near the indentations as the SE here is significantly higher than in the surrounding rolled matrix microstructures. No nuclei are observed away from indentations. The higher the indentation load, the more nuclei are observed to form. The amount of rolling reduction also affects nucleation: larger rolling reduction leads to more nucleation at the same annealing condition.
2. Hardness indentations in only some of the investigated grains were observed to stimulate nucleation. The general trend is that grains with higher hardness values are more prone to stimulate nucleation than those with lower hardness values. As the orientations of the grains are known to determine the evolution of the deformation microstructure, grain orientations are also very likely to affect the more complex deformation microstructures underneath hardness indentations, and higher hardness values may lead to higher dislocation densities and thus higher SEs stimulating the nucleation. For the present samples, which are rolled before indentation, it is suggested that besides the local SEs also the morphology of the deformation microstructures may affect the potential for nucleation, and it is found that

banded deformation microstructures stimulate more nuclei than matrix with cell structures.

3. The orientations of the nuclei from different indentations in a given grain are observed not to be randomly distributed, but clustered in limited orientational spaces. The nuclei orientations are related to the orientations present in the complex deformed matrices near the tips of the indentations. Nucleation by mechanisms such as subgrain coalescence, strain induced *dislocation* boundary migration or subgrain growth could thus lead to nuclei as those observed in the present work.
4. When only inspected on the surface, most of the nuclei are observed to have large misorientations to the matrix. However, by local orientation measurements near the indentation tip in the deformed state, it is shown that the orientational spread observed there covers the orientations of the nuclei observed in the annealed state of an identical sample. This underlines the importance of careful 3D or even better 4D (x, y, z and t) experimental investigations of nucleation in samples as the present ones.

Chapter 5

Nucleation at hardness indentations in high purity aluminum – 4D experimental measurements

As mentioned in the previous chapters, electron microscopy studies of nucleation are restricted by the fact that the 3D microstructure cannot be observed, but only the polished sample surfaces. When nucleation takes place in the bulk materials, the nuclei consume the deformed microstructures, making it impossible to quantify what was before nucleation and what happens during nucleation itself. In this chapter, a 4D (x, y, z and t) investigation of nucleation is conducted. Compared with 'after-the-fact' static 2D/3D study, the 4D study can directly explore the evolution of the microstructure during nucleation, avoiding the problem of 'lost evidence' [21].

Based on the results of the 2D investigations in chapter 4, the hypothesis is that the nuclei form at sites near the indentation tips with orientations already present there, and then they grow into new regions of the deformed materials to form high angle boundaries (HABs) to the surrounding matrix. To test this hypothesis and to further characterize the precise nucleation sites, the orientation relationship between the nuclei and the deformed matrix where they form, a 4D (x, y, z and t) investigation of nucleation in samples as the ones described in chapter 4 is conducted.

By combining the 2D results with the possibilities of the 4D differential aperture X-ray microscopy (DAXM) experiment, the following DAXM experimental conditions were selected: ① the 'powerful' grain, Grain E, with a high nucleation probability, ② controlled deformation (12%, 500 g) and annealing at 275 °C for 10 min. These conditions have good potentials for ① nucleation at

the selected hardness indentation and ② only limited growth of the nuclei. It has to be underlined how important it is to have a-priori knowledge about where nucleation is likely to happen and that growth will not be too extreme at the selected annealing condition. The DAXM measurements of 3D volumes of reasonable sizes are extremely time consuming; i.e. only ex-situ experiments are possible. This means that for the present type of experiment, first a selected volume in the deformed state has to be characterized, *which takes days of measuring time;* then the sample is annealed and the same volume is measured again. It is thus clear that if either no nuclei form in the selected volume or one or more nuclei grow to consume a large fraction of the selected volume, the experiment is of very little value.

On the other hand, if one or a few nuclei form and grow to a small size only, it is possible for the first time ever to experimentally quantify exactly where in the deformed microstructure the nuclei form, what crystallographic orientation relationships exist between each nucleus and its parent deformation structural 'element' as well as pinpointing potential nucleation sites. This experiment thus has potentials to give the first direct experimental data on nucleation in the bulk of an opaque sample.

5.1 Experimental methods

The investigation presented in chapter 4 has shown that nucleation preferentially occurs near hardness indentations in grains with higher average hardness. For the present experiment a large grain with {3-1-1} <215> orientation (Grain E in section 4.3.2) was chosen and was deformed using exactly the same experimental conditions as the samples analyzed in section 4.3: cold rolled to 12% reduction in thickness followed by indentations with a load of 500 g. Within this grain, the indentation with the highest hardness of 27.3 Kgf/mm^2 was chosen to facilitate nucleation upon later annealing. To optimize the annealing condition, several samples containing Grain E were annealed at different temperatures (275-310 °C) for various times (2min-1h).

Based on the results of nucleation possibilities and nuclei sizes, the annealing condition for the synchrotron experiment was determine to be 275 °C for 10 min.

The microstructure around the indentation tip was mapped using white-beam DAXM at the beam line 34-ID-E at the Advanced Photon Source (APS) at Argonne National Laboratory, USA [25]. For the DAXM experiments, a focused polychromatic X-ray microbeam with a Lorentzian profile and a full-width half maximum of ~0.5 µm was defined using two non-dispersive Kirkpatrick-Baez (K-B) mirrors. The sample was mounted on a sample holder at a 45° incidence angle to the incident focused microbeam. The Laue diffraction pattern from the whole volume illuminated by the incident microbeam was recorded on a Perkin-Elmer flat panel detector mounted in a 90° reflection geometry, 510.3 mm above the sample. To resolve the diffraction pattern from each voxel within the selected volume at different depths, a Pt-wire of 50 µm diameter was used as a differential aperture and scanned at a distance of ~100µm from the sample surface. The Laue patterns at each depth were reconstructed by ray-tracing using the LaueGo software available at APS beamline 34-ID-E [149]. The reconstructions were conducted to a depth of about 240 µm into the sample with a step size of 1.5 µm. The crystallographic orientations were then indexed based on the depth-resolved Laue patterns (see figure 5.1). The orientation resolution obtained was about 0.01°. By scanning the focused microbeam horizontally and vertically with step size of 1.5 µm and repeating the wire scan at each position, a volume of 243 × 79.5 × 76.5 μm^3 around the selected indentation tip was mapped. This scan took 65 hours.

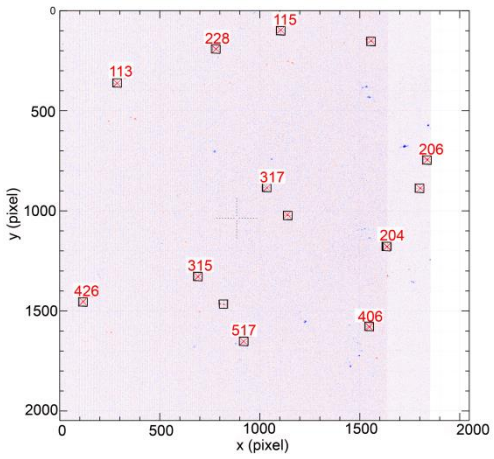

Figure 5.1: An example of a depth-resolved Laue diffraction pattern from a voxel within the deformed volume 75 µm below the sample surface. The indexed diffraction spots are marked by squares and the hkl indexes of the identified diffracting crystallographic planes are given. Reproduced from article D.

The sample was then annealed ex-situ at 275 °C for 10 min in an air furnace to stimulate nucleation, and subsequently characterized again. Finding the exact same volume as that characterized before annealing was facilitated by the use of 3 Pt fiducial marks which were deposited using a focused ion beam instrument prior to the experiment. The marks were placed about 160 µm away from the indentation center. By matching the microstructure and shape of the hardness indent in the remeasured volume before and after remounting, a further refinement to a 1.5 µm position accuracy was achieved.

5.2 Three dimensional deformation microstructures

The deformed volume measured before annealing is shown in figure 5.2(a). The relationships between the laboratory (x, y and z) and the sample (RD, TD and ND) coordinate systems and the mapped sample volume are shown in figure 5.2(b), where the volume characterized is marked by black lines. The grey lines at the top of the sample indicate the orientation of the hardness indentation in relation to the sample coordinate system. It should be noted that the size of the real hardness indentation is larger than the one indicated by the grey lines. In figure 5.2(a), the colors show the crystallographic orientations of the normal direction (ND) within each voxel according to the color legend. The indentation

tip is marked by a big yellow arrow. The sharp changes in color near the indentation surface, especially along the symmetry lines of the indentation, clearly show the orientation changes within deformation microstructures. This is in agreement with the earlier destructive experimental characterization (see chapter 4) and simulations [24, 29]. For the region far away from the indentation, extended planar dislocation boundaries, which are formed during cold rolling, can be observed.

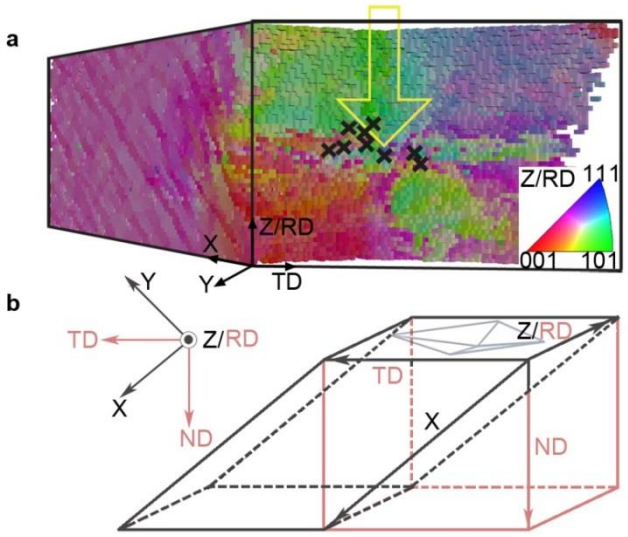

Figure 5.2: (a) The deformed volume measured before annealing and (b) the relationships between the laboratory and sample coordinate systems and the mapped sample volume. The color of each voxel is inverse pole figure color as shown in the color code.

The deformation microstructures can be better visualized by plotting the orientation deviation of each voxel to the average orientation of the whole deformed volume, as shown in figure 5.3(a) (misorientation angle) and 5.3(b) (misorientation axis). It is clear that the deformation microstructure is inhomogeneous (see figure 5.3(a)). Some regions have high misorientations to the average orientation, up to 35°, while other regions have misorientations less than 5° to the average orientation. As discussed in chapter 4, during indenting, the 4 sides of the indentation are pushed towards different crystal orientations

and thus the 4 sides are rotated around different axes, as is clearly seen in figure 5.3(b).

The 3D deformation microstructures can be analyzed in detail slice by slice. Figure 5.4(a) and (b) show the deformation microstructures of the TD-ND section through the indentation tip. It can be seen that the voxels close to the indentation surface have higher misorientation to the average orientation of the whole deformed volume than the voxels far away, especially the voxels exactly on the indentation tip. The extended planar dislocation boundaries can be observed clearly in this section (see figure 5.3(b) and 5.4(b)).

(a)

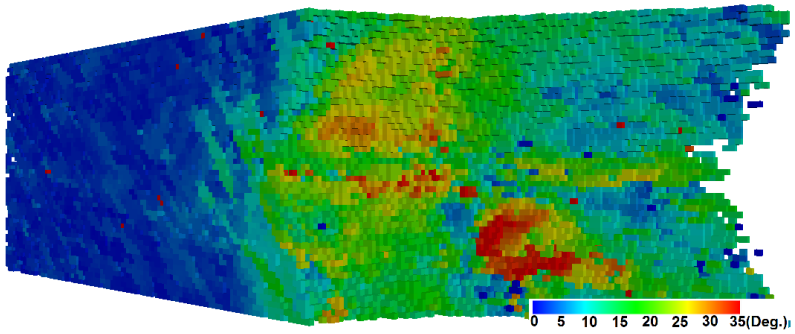

(b)

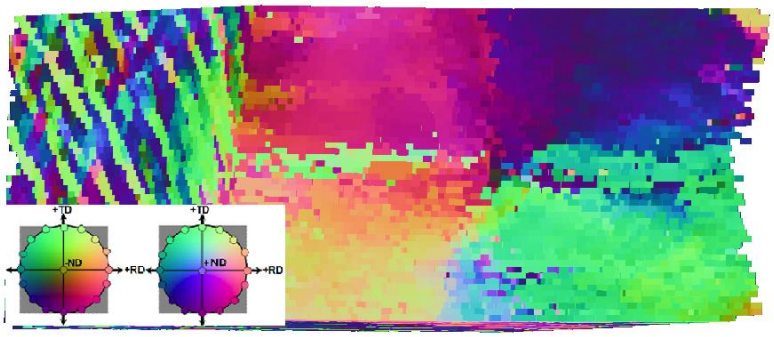

Figure 5.3: The deformation volume measured before annealing. The color of each voxel is defined by the crystallographic orientation deviation to the average orientation of the entire measured volume: (a) misorientation angle and (b) misorientation axis. The coordinate system is same as in figure 5.2.

(a) (b)

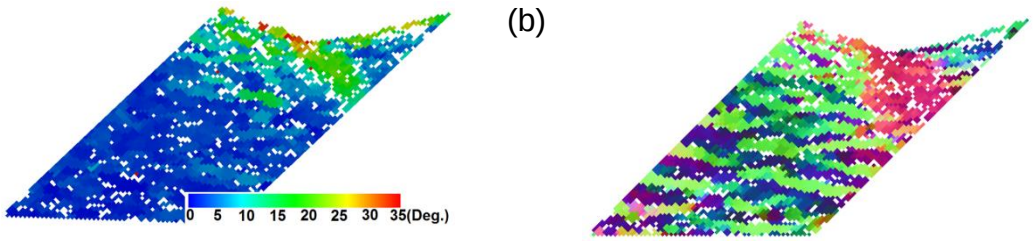

Figure 5.4: The deformation microstructure of the TD-ND section through the hardness indentation tip. The color codes of each voxel in (a) and (b) are the same as that in figure 5.3(a) and (b) respectively.

5.3 Nucleation

In total, 12 nuclei are observed within the selected gauge volume after annealing at 275 °C for 10 min. Figure 5.5(a) shows the annealed volume and figure 5.5(b) and (c) show all the 12 nuclei together with the indentation surface. It is clear that all the nuclei are very close to the indentation surface and no nuclei are observed far away from the indentation. Two of the nuclei are twin related, one of which has grown out of the volume we measured. Another nucleus grew to a very large size. These three nuclei are not analyzed further in the following, as it is not possible to identify where exactly these nuclei formed. The volumes of the remaining 9 nuclei are in the range of 6 voxels to 2055 voxels, i.e. from few micrometers to tens of micrometers in size.

(a)

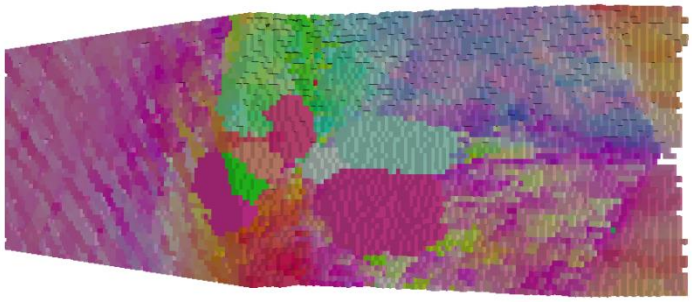

(b) (c)

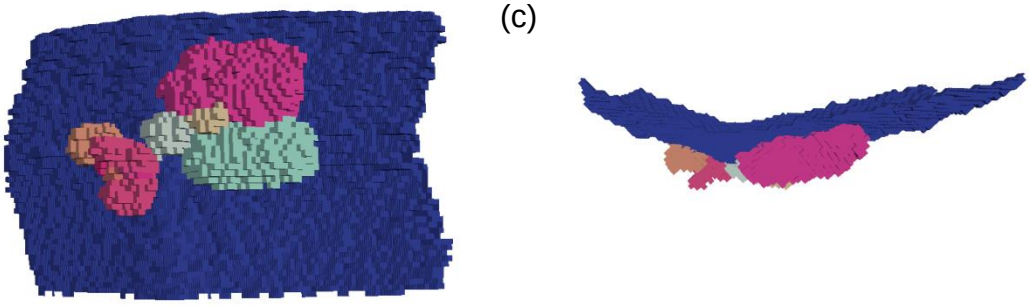

Figure 5.5: (a) The annealed volume measured after annealing; (b) and (c) all nuclei formed after annealing and the indentation surface (the blue shell): (b) bottom-top-view and (c) side view. The voxels in the blue shell do not belong to the measured voxels but are the voxels just adjacent to and above the indentation surface.

5.4 Orientation relationship between nuclei and the deformed matrix

The orientation relationship between each nucleus and the deformed matrix consumed by the nucleus can be analyzed by plotting a pole figure showing the orientation of the nucleus and the orientations present in the same volume before the sample was annealed. Two examples are shown in figure 5.6: one for a big nucleus consisting of 1177 voxels and one for a small nucleus consisting of 227 voxels. The orientations of the nuclei are shown by diamonds and the orientations of the deformed matrix in the corresponding volumes are shown by red dots. To allow for the slight uncertainty in sample position when remounting the sample after furnace annealing, voxels in a ‘cloud’ of approximately 1.5 µm around the nucleus are included in the analysis. The orientations within the cloud are shown by green dots in figure 5.6. It can be seen that the orientations of the two nuclei are within the distribution of orientations present in the deformed matrix in the same volume before annealing. The orientations of all the 9 nuclei that formed during the present experiment are plotted in one pole figure (see figure 5.7) together with orientations of the whole measured deformed volume. It can be noticed that most of orientations of the nuclei are exactly within the orientation spread of the deformed matrix. In only one case, the orientation of nucleus No. 4 (consisting

of 207 voxels) is on the outskirts but still within the orientation spread of the deformed matrix. All the 9 nuclei can thus be considered to form with orientations already present in the deformed matrix.

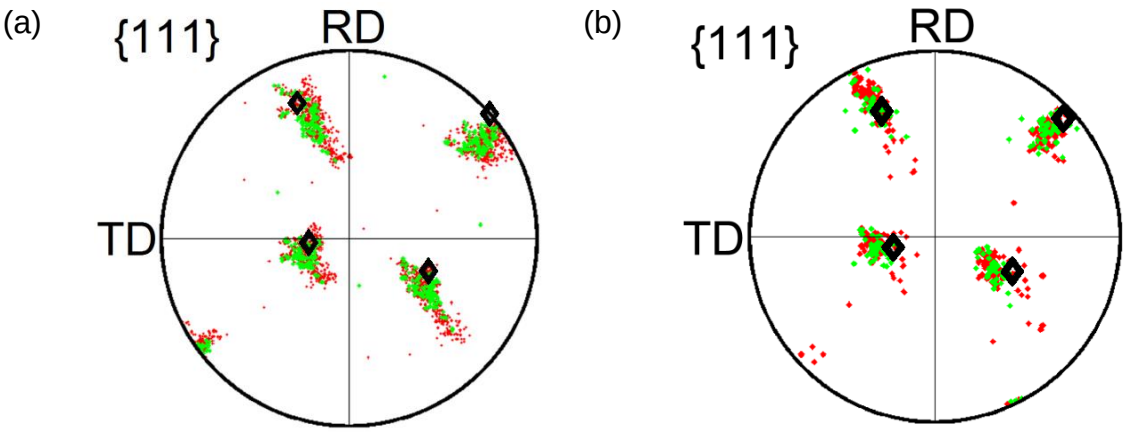

Figure 5.6: {111} pole figures showing the orientation relationships between nuclei and the matrix in the corresponding volumes in the deformed state before annealing: (a) nucleus No.1 and (b) nucleus No.3. The nucleus orientation is shown by large black diamond shaped markers. Red dots show the orientations in the deformed state for voxels identified as belonging to the nucleus after annealing, and green dots show voxels belonging to the 'cloud' around the nucleus volume, included to allow for the possible small sample misalignment when remounting the sample after the annealing. (b) is reproduced from article D.

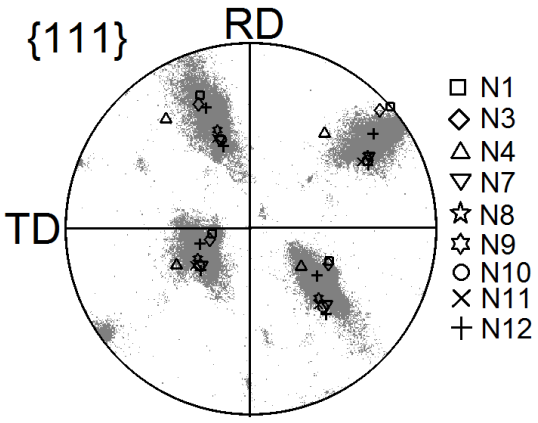

Figure 5.7: {111} pole figure showing the orientation relationship between the remaining 9 nuclei and the whole deformed matrix measured before annealing.

The grey dots represent the orientation distribution of the whole deformed matrix and the other markers show the nuclei orientations, as given in the legend.

It should be noted that no correlation is found between the sizes of the nuclei and their orientations within the deformed orientational scatter. For example, the nucleus with an orientation towards the outskirts of the deformed orientational scatter is not bigger or smaller than nuclei with orientations well within the orientational scatter.

5.5 Nucleation sites

Either 3D characterization of the deformed microstructure *or* of the annealed microstructure could have been obtained by serial section experiments combined with EBSD characterization in the SEM. The novelty of the present experiment is that now *the deformed and the annealed* microstructures are characterized within the exact same sample volume. It is thus possible to precisely relate the nucleation to the microstructure in the deformed state and use this to get information about nucleation sites.

According to the position relationship of the two measured volumes before and after annealing, the deformed volume consumed by each nucleus was extracted, as shown in figure 5.8. The misorientation between each nucleus and each voxel within the deformed matrix consumed by the nucleus is calculated. Following the hypothesis of the classical nucleation theories, it is assumed that the nuclei form with orientations similar to the deformed matrix. The voxels in the consumed deformed matrix having misorientations below 2° to the nucleus are thus considered to be the embryonic volume of the nucleus.

An example is shown in figure 5.9. Here the microstructure is visualized in the TD-ND plane slice-by-slice in the annealed and deformed state. The successive sections are 1.5 µm apart in the rolling direction. The nucleus is marked in blue. The color of each voxel represents its misorientation to the nucleus, as shown in the color legend (In the annealed state, another 2 nuclei are seen in yellow

and grey — those are not visualized and analyzed in detail in this figure). By inspecting the section in the deformed state, it is clear that 3 voxels marked by an arrow in the middle slice have orientations similar (< 2°) to the nucleus and such ‘identical orientations’ cannot be found anywhere else. All other voxels have other orientations. It is thus reasonable to assume that the embryonic volume leading to this nucleus is those 3 voxels marked by an arrow in the deformed state and by yellow crosses in the sections of the annealed state.

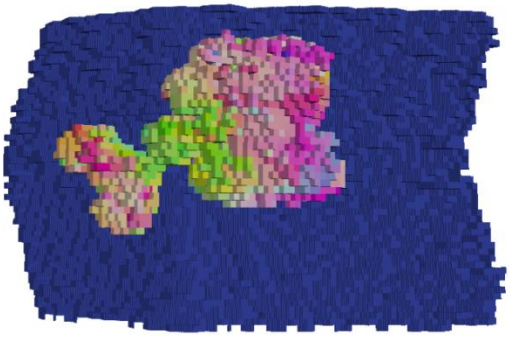

Figure 5.8: The deformed matrix consumed by the nuclei together with the indentation surface.

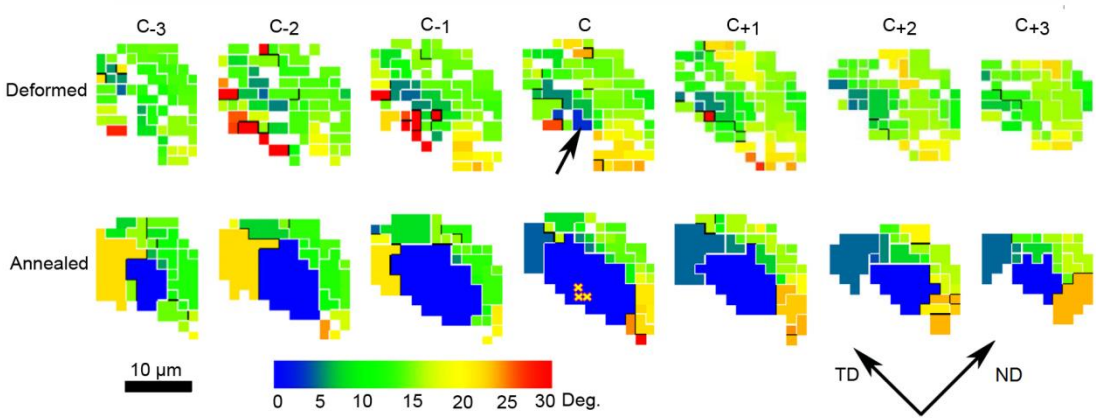

Figure 5.9: Successive sections, 1.5 µm apart along the rolling direction. The nucleus is shown in blue and all other voxels are colored according to the misorientation angle to the nucleus orientation. The white and black lines show misorientations in the range 2-15° and above 15°, respectively. The embryonic volume of the nucleus is marked by an arrow and yellow crosses in the sections showing the deformed and annealed state respectively. Reproduced from article D.

With this method, the embryonic volumes of the remaining 8 nuclei are obtained. All the other 8 nuclei follow the same pattern, i.e. for each nucleus there are a few, and only a few, adjacent voxels in the deformed state with an orientation similar (< 2°) to that of the nucleus.

The embryonic volumes, which are suggested to be the nucleation sites, of the 9 identified nuclei are shown together with the surface of the deformed volume in figure 5.10. It can be seen that all the 9 nuclei form near the indentation tip, and more specifically along the symmetry lines in the indentation zone formed by the ridges of the diamond shaped indenter.

(a) (b)

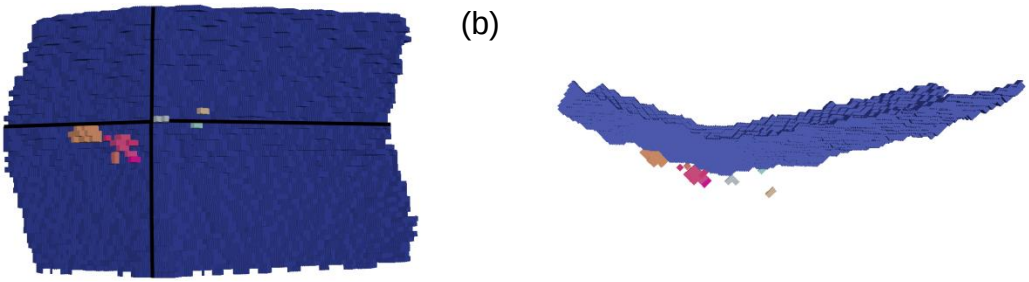

Figure 5.10: The embryonic volumes of the remaining 9 nuclei together with the indentation surface: (a) bottom-top-view and (b) side view. The black lines in (a) represent the two diagonal lines of the indentation. (b) is reproduced from article D.

An example of a nucleus (the grey voxels) and its nucleation site (the red voxels) is given in figure 5.11(a), which shows their relative positions to the indentation surface (the blue voxels). It can be observed that the nucleation site lies exactly on the indentation surface and the embryo of the nucleus consists of 3 voxels. Figure 5.11(b) visually shows that the nucleus and its nucleation site are situated centrally at the intersection of the two diagonal lines in the center of the indentation. The nucleus has grown from this small embryo along the indentation surface and into the bulk. After the annealing, it has a size of 17 µm in diameter.

(a) (b)

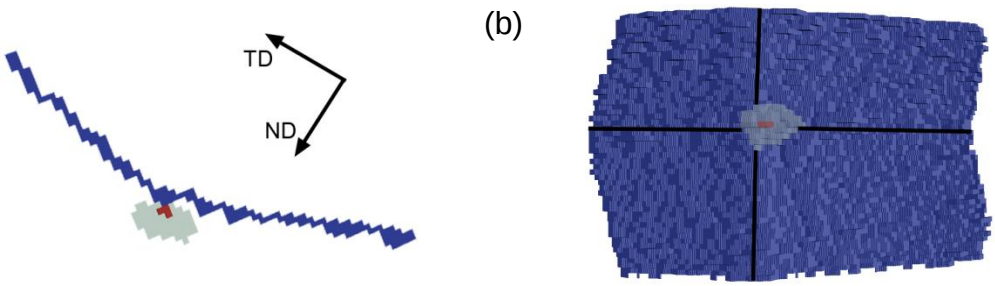

Figure 5.11: (a) A transverse section (TD-ND) of the indentation surface (the blue voxels), a nucleus (the grey voxels) and its embryonic volume (the red voxels) and (b) the relative position of this nucleus, its embryonic volume and the indentation tip (the bottom-to-top view).

5.6 Correlation of nucleation sites with stored energy

The above analysis leads to a precise pinpointing of nucleation sites, which are marked in figure 5.10. To understand why these sites are the active ones, the local SE contained in the dislocation boundaries in the deformed matrix is calculated using the method suggested in [152].

Instead of the calculation method calculating SE of an area in chapter 4, here a new calculation method providing a value directly for each volume voxel is used. For this analysis, the local SE was calculated using the following equation [152]:

$$E = \frac{3Gb}{2\Delta}\theta_{KAM}. \quad (4.1)$$

where b is the Burgers vector, G is the shear modulus, Δ is the step size (1.5 µm for the present volume) and θ_{KAM} is the average misorientation calculated as kernel average misorientation (KAM), which is defined for a given voxel as the average misorientation of that voxel with all its 26 immediate neighbors. For the KAM calculation, a low cut-off angle of 0.2° was used, which is the critical angle used for detecting recrystallization nuclei (determined based on trials and error). No high cut-off angle was used, as all boundaries in the volume are dislocation boundaries.

Compared to the method of calculating SE in chapter 4, this method has the advantage of being able to give a value for local SE on the scale of individual

voxel, and therefore with a spatial resolution limited by the step size, 1.5 µm. Another advantage is that it provides a value directly for each voxel, and thus in a format that can be easily visualized as a map. However, it should be noted that the average misorientation calculated for each voxel based on the misorientation to all neighbor voxels within the kernel, typically including voxels that are not in fact separated by real boundaries.

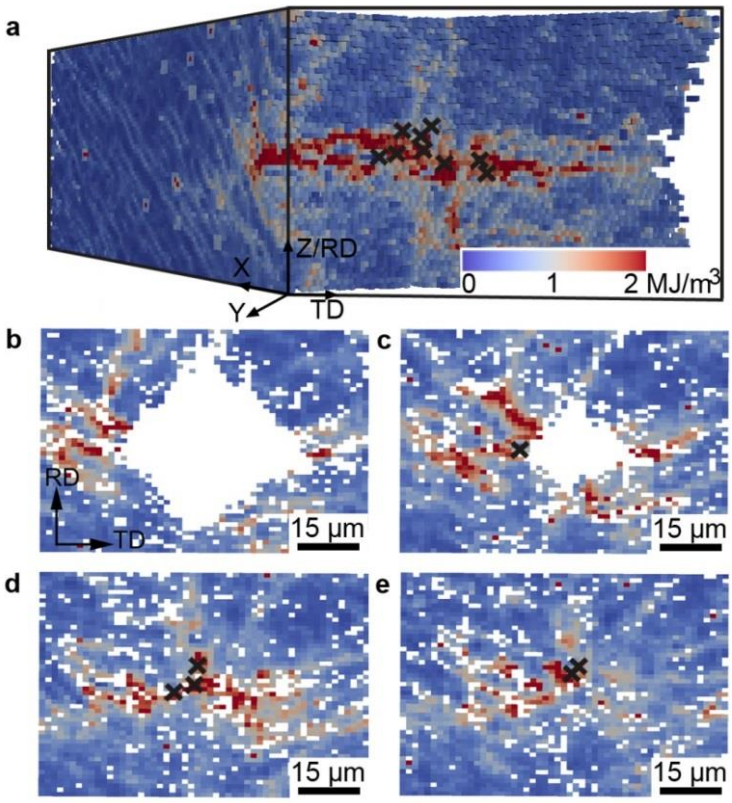

Figure 5.12: Distribution of stored energy in the deformed state. (a) is a 3D map of the stored energy (the magnitudes are indicated by the color legend). The crosses mark the positions of the identified embryonic volumes. (b), (c), (d) and (e) show sections near the indentation tip: (b) 8.5 µm above, (c) 4.3 µm above, (d) exactly at, and (e) 3.2 µm below the tip. Reproduced from article D.

The distribution of SE is visualized in figure 5.12. The crosses mark the nucleation sites. It can be seen that the voxels with relatively high SE are distributed mainly along the diagonal lines and near the indentation tip. Figures 5.12(c)-(e) are sections through some of the nucleation sites. The results underline that nuclei preferentially form at locations with high SEs.

5.7 Activation of embryonic volumes

The measured deformed volume also allows a detailed analysis of why the initial embryonic volumes at high SE sites continue to grow in the deformed microstructure, i.e. grow to become the observed nuclei. It is well accepted that HABs (e.g. ≥ 10°) migrate faster than low angle boundaries (LABs) [1, 153]. It is thus of interest to analyze the fraction of HABs surrounding the 9 nuclei by using the present 4D data (3D plus time). The misorientations between the voxels identified as the embryonic volume for each nucleus and its surrounding voxels are calculated and it is found that 46% of the boundary segments surrounding these embryonic volumes are HABs (≥ 10°). Another 9 volumes of the same size are chosen far away from indentations to investigate their boundary segments and only 0.05% of the segments are HABs (≥ 10°). It is thus suggested that the observed 9 nuclei developed because of this advantage of fast migrating boundaries surrounding the initial embryonic volumes.

The present data also allows a detailed analysis of the continued growth of the embryonic volumes. The misorientations between the nuclei and the deformed matrix ‘eaten’ by the nuclei are calculated. Figure 5.13(a) is an example for nucleus No.1. The black histograms represent the misorientations between nucleus No.1 and its consumed deformed matrix, while the red histograms show the misorientations between nucleus No.1 and the surrounding recovered matrix. It can be seen that both histograms are mainly in the range of 5°-20° but the black one has less low misorientations (≤5°). This is the case for all the 9 nuclei.

In Figure 5.13(b), the misorientations between the nuclei and the deformed matrix ‘eaten’ by the nuclei are shown for the 2 large (No.1 and 10) and the 3 smallest nuclei (No. 3, 4 and 9). It can be seen that for both groups more than 63% of the misorientations are above 10°, while 13% and 5% are below 5° for the 3 small and the 2 large nuclei, respectively. The nuclei that have grown the least in the present experiments thus have more than twice the frequency of boundaries with misorientations of 5° or less, i.e. are partly surrounded by low angle boundaries, which are believed to migrate very slowly [154].

(a) 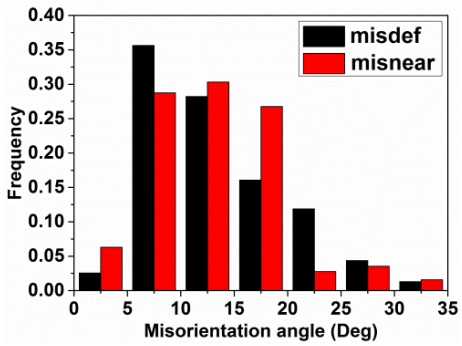

(b) 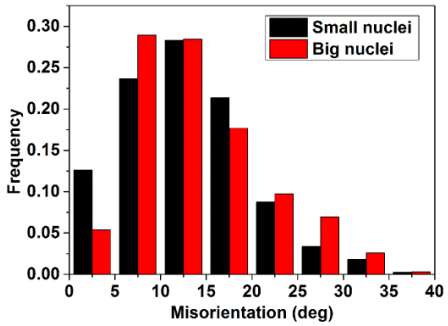

Figure 5.13: (a) The distribution of misorientations between nucleus No.1 and the deformed matrix eaten by it (the black histogram) and misorientations between nucleus No.1 and its surrounding recovered matrix. (b) The distribution of misorientations between nuclei and the deformed matrix 'consumed' by the nuclei. In figure b, the misorientations for the two largest nuclei are shown in red and in black for the three smallest nuclei. The figure shows some preference for larger misorientations for the two large nuclei. (b) is reproduced from article D.

5.8 Summary

The 4D investigation of nucleation highlights the unique capability of the DAXM technique for direct studies of nucleation. The technique is unique because it is both non-destructive and has a spatial resolution allowing a detailed investigation of the deformed microstructure. For a 12% cold rolled aluminum sample further deformed by a hardness indentation, it is found using this technique that:

1. With the 4D data set, the nucleation sites are determined. It is found that the nuclei form mainly along the diagonal lines and near the indentation tip. It is determined unambiguously that the nuclei form with orientations already present in the matrix. Nucleation mechanisms such as subgrain growth, subgrain coalescence and strain induced *dislocation* boundary migration can explain the nucleation in the present work.
2. With the detailed 3D deformation microstructure, the local SE for each volume voxel is estimated. By correlating the distribution of the SEs with the nucleation sites, it is found that the nucleation preferentially happen at locations with high SEs.

3. The misorientation analysis shows that the embryonic volumes of the nuclei are partly surrounded by HABs (>10°) before and during annealing. It is thus suggested that the viable 9 nuclei develop because of the advantage of fast migrating HABs. It has also shown that boundaries between nuclei and the deformed matrix of less than 5° hinder the growth of nuclei.

Chapter 6
Conclusions and outlook

The objective of this study was to explore nucleation of recrystallization at selected sites in face-centered-cubic metals. Two types of specially selected samples were included: high purity columnar-grained nickel deformed by cold rolling and high purity aluminum deformed by cold rolling followed by Vickers hardness indentations. These samples were selected to allow some control over where nucleation is expected to occur. Various experimental techniques were used for the characterization, namely, optical microscopy, scanning electron microscopy-electron backscattering diffraction and electron channeling contrast as well as differential aperture X-ray microscopy using X-rays from a synchrotron source. The main conclusions and suggestions for future work are given in the following.

In the columnar-grained nickel samples cold rolled to 50% reduction, the general observation of triple junctions (TJs) and grain boundaries (GBs) being very potential nucleation sites is confirmed. In the present sample 16% of the TJs stimulate nucleation and 74% of the nuclei form at TJs while 26% form at GBs. No nuclei are detected within the grain interior. A focal point of the present work is orientation relationship between nuclei and matrix. Based on surface observation, it is found that some nuclei have similar orientations to the surrounding matrix with misorientations lower than 15°. It is concluded that these nuclei may form by subgrain growth or SIBM. Some nuclei form $\sum 3$ boundaries to one of their surrounding matrix grains and may form by twinning. Only a few nuclei (12.1%) have orientations different from the surrounding matrix.

With the aim of investigating which TJs are the most potential nucleation sites, hardness tests at the TJs were used to investigate possible correlations

between hardness values and the number of nuclei at TJs sites. It is concluded that the *differences in hardness* between the grains at nucleating TJs are larger than that at TJs that do not stimulate nucleation. Reasons for this may be related to the driving force: nucleation by SIBM would be facilitated by the difference in stored energy (SE) (here taken proportional to the hardness), which will drive the boundary towards the higher SE regions.

In the series of aluminum samples weakly rolled (20% and 12%) and further deformed locally by Vickers hardness indentations, the hardness indentations as expected lead to large additional grain subdivision near indentation tips leading to higher SE here. The higher the indentation loads, the larger the subdivision and additional SE are. All nuclei form around the indentations and no nuclei are observed far away from indentations, which are as expected because the SEs at indentations are significantly higher than in the surrounding rolled matrix microstructures.

Unique to the present work was that many hardness indentations were done within each original grain and that many original grains of different crystallographic orientations were investigated. A clear correlation between grain orientation and nucleation potential is found: grains with higher SE in the rolled microstructures and thus higher average hardness values have higher nucleation probabilities. Scatter within the original grains is observed, but the nucleation percentages at all the hardness indentations reveal a clear tendency that indentations with higher hardness values have higher nucleation potentials. The scatter is concluded to be a consequence of the inhomogeneity of deformation microstructures within the original grains. It is suggested that besides the local SEs and thus hardness, the morphology of the deformation microstructures affect the potential for nucleation, and it is shown that grain with an interior cell deformation microstructure is less likely to stimulate nucleation than grains that are subdivided by extended dislocation boundaries

The orientations of the nuclei from different indentations in a given grain are observed not to be randomly distributed, but clustered in limited orientation

spaces. When inspected on the surface, most of the nuclei form only high angle boundaries to the matrix. By local orientation measurements near the indentation tips in the deformed state, it is however shown that the orientation spread observed there, covers the orientations of the nuclei observed in the annealed state of an identical sample. Potential nucleation mechanisms include subgrain coalescence, strain induced *dislocation* boundary migration and subgrain growth.

Whereas, the above results were obtained by the electron microscopy, the nucleation at hardness indentations was also investigated non-destructively by the DAXM technique in the present work. The DAXM is the only technique that at present can characterize the microstructures and crystallographic orientations in the bulk with sufficient spatial resolution. By first characterizing the deformation microstructure within a selected gauge volume near a hardness indentation, then annealing the sample and measuring the same volume again, nucleation was directly related to the local deformation microstructure in the bulk of the sample. It is found that nuclei preferentially form at areas of high SEs and grow because of an advantage of fast migrating boundaries surrounding the initial embryonic volumes. All nuclei are found to have crystallographic orientations as the embryonic volumes in the deformed state. It is also revealed that boundaries between nuclei and the deformed matrix of less than 5° hinder subsequent growth of the nuclei.

The DAXM observation on nucleation in the opaque bulk metals has been a central part of the work. It allows nucleation of recrystallization to be directly related to deformation microstructures, which makes it possible to investigate the microstructure evolution of each voxel during annealing and thus the orientation relationships between nuclei and the deformed matrix where they form. It demonstrates the possibilities for obtaining direct information on active nucleation sites and nucleation mechanisms – information absolutely necessary to analyze the effects of deformation-induced microstructural variations on nucleation, and to advance the understanding and modeling of nucleation of recrystallization.

More modeling work using e.g. crystal plasticity FEM could be done to predict the local deformation microstructure after indentation to understand the formation of local deformation microstructure at different indentation sides. The simulation result can be compared with the present experimental data, such as local SEs, local changes in orientation. By combining experimental and theoretical (modeling) results, an ultimate goal could be to study the effects of deformation-induced *local* microstructural variations on nucleation, to establish theories for active nucleation mechanisms, and to successfully predict recrystallization microstructures (e.g. grain sizes and textures).

Abbreviation

Abbreviation	Full name
BSE	Backscattered electron
CCD	Charge-coupled device
CB	Cell block
DDW	Dense dislocation wall
DAXM	Differential-aperture X-ray microscopy
ECC	Electron channeling contrast
EBSD	Electron backscattered diffraction
GNB	Geometrically necessary boundary
GB	Grain boundary
HAB	High angle boundary
IDB	Incidental dislocation boundary
IPF	Inverse pole figure
LAB	Low angle boundary
LEDS	Low energy dislocation structure
ND	Normal direction
RD	Rolling direction
SEM	Scanning electron microscopy
SE	Stored energy
SIBM	Strain induced boundary migration
TEM	Transmission electron microscopy
TD	Transverse Direction
TJ	Triple junction

Reference

[1] Humphreys, F.J. & Hatherly M. 2004 *Recrystallization and related annealing phenomena.* Pergamon Press Oxford.

[2] Haessner, F. 1978 *Recrystallization of metallic materials.* Riederer Verlag, Stuttgart.

[3] Doherty, R. D. *et al.* 1997 Current issues in recrystallization: a review. *Mater. Sci. Eng. A* **238,** 219-274.

[4] Gruber, J., Miller, H. M. & Hoffmann, T. D. 2009 Misorientation texture development during grain growth. Part I: simulation and experiment. *Acta* Mater*.* **57,** 6102-6112.

[5] Beck, P. A. & Sperry, P. R. 1950 Strain induced grain boundary migration in high purity aluminum. *J. Appl. Phys.* **21,** 150-152.

[6] Bailey, J. E. & Hirsch, P. B. 1962 The recrystallization process in some polycrystalline metals. *Proc. Roy. Soc. A* **267,** 11-30.

[7] Cahn, R. W. 1950 A new theory of recrystallization nuclei. *Proc. Phys. Soc. A* **63,** 323-326.

[8] Beck, P. A. 1949 The formation of recrystallization nuclei. *J. Appl. Phys.* **20,** 633-634.

[9] Cottrell, A. H. 1953 The theory of dislocations. *Progr. Met. Phys.* **4,** 205-264.

[10] Hu, H. 1962 Direct observations on the annealing of a Si-Fe crystal in the electron microscope. *Trans. Metall. AIME* **224,** 75-84.

[11] Li, J. C. M. 1962 Possibility of subgrain rotation during recrystallization. *J. Appl. Phys.* **33,** 2958-2965.

[12] Albou, A. *et al.* 2010 Direct correlation of deformation microstructures recrystallization nucleation in aluminum. *Scripta Mater.* **62,** 469-472.

[13] Wu, G. L. & Juul Jensen, D. 2007 Orientations of recrystallization nuclei developed in columnar-grained Ni at triple junctions and a high-angle grain boundary. *Acta Mater.* **55,** 4955-4964.

[14] Vandermeer, R. A. & Gordon, P. 1959 Edge-nucleated, growth controlled recrystallization in aluminum. *Trans. Metall. AIME* **215,** 577-588.

[15] Leslie, W. C., Michalak, J. T. & Aul, F. W. 1963 The annealing of cold-worked iron. In: *Iron and Its Dilute Solid Solutions* pp.119-216 (Eds. Spencer C. W. and Werner F. E. Interscience, New York).

[16] Humphreys, F. J. 1977 The nucleation of recrystallization at second phase particles in deformed aluminum. *Acta Metall.* **25,** 1323-1344.

[17] Weiland, H., Rouns, T. N. & Liu, J. 1994 The role of particle stimulated nucleation during recrystallization of an aluminum-manganese alloy. *Z. Metallk.* **85,** 592-597.

[18] Quinta da Fonseca, J. & Ko, L. 2015 The kinetics of deformation and the development of substructure in the particle deformation zone. 36th Risoe International Symposium on Effect of Deformation Induced Structural Variations on Annealing Mechanisms, *IOP Conf. Ser. Mater. Sci. Eng.* **89,** 012012.

[19] Eylon, D., Rosen, A. & Niedzwiedz, S. 1969 Recrystallization of aluminum single crystals after point deformation. *Acta Metall.* **17,** 1013-1019.

[20] Fan, G. H., Zhang, Y. B., Driver, J. H. & Juul Jensen, D. 2014 Oriented growth during recrystallization revisited in three dimensions. *Scripta Mater.* **72-73,** 9-12.

[21] Duggan, B. 1996 The problem of lost evidence. Term discussed at the 11st ICOTOM conference, Xian, China.

[22] Wu, G. L., Godfrey, A., Juul Jensen, D. & Liu, Q. 2005 Deformation strain inhomogeneity in columnar grain nickel. *Scripta Mater.* **53,** 565-570.

[23] Wu, G. L., Godfrey, A., Winther, G., Juul Jensen, D. & Liu, Q. 2011 Evolution of orientations and deformation structures within individual grains in cold rolled columnar grained nickel. *Acta Mater.* **59,** 5451-5461.

[24] Zaafarani, N., Raabe, D., Roters, F. & Zaefferer, S. 2008 On the origin of deformation-induced rotation patterns below nanoindents. *Acta Mater.* **56,** 31-42.

[25] Larson, B. C., Yang, W., Ice, G. E., Budai, J. D. & Tischler, J. Z. Three-dimensional X-ray structural microscopy with submicrometer resolution. *Nature* **415,** 887-890 (2002).

[26] Cahn, J. W. 1996 The time cone method for nucleation and growth kinetics on a finite domain. *Mat. Res. Soc. Symp. Proc.* **398,** 425-437.

[27] Rios, P. R. & Villa, E. 2009 Transformation kinetics for inhomogeneous nucleation. *Acta Mater.* **57,** 1199-1208.

[28] Budai, J. D. *et al.* 1997 Controlling the size, structure and orientation of semiconductor nanocrystals using metastable phase recrystallization. *Nature* **390,** 384-386.

[29] Kiener, D., Pippan, R., Motz, C. & Kreuzer, H. 2006 Microstructural evolution of the deformed volume beneath microindents in tungsten and copper. *Acta Mater.* **54,** 2801-2811.

[30] Levine, L. E. *et al.* 2006 X-ray microbeam measurements of individual dislocation cell elastic strains in deformed single-crystal copper. *Nature Materials* **5,** 619-622.

[31] Doherty, R. D. 1974 The deformed state and nucleation of recrystallization. *Met. Sci.* **8,** 132-142.

[32] Bay, B., Hansen, N. & Kuhlmann-Wilsdorf D. 1989 Deformation structures in lightly rolled pure aluminum. *Mater. Sci. Eng. A* **113,** 385-397.

[33] Kocks, U. F. & Canova G. R. 1981 How many slip systems, and which? *Proceeding of the 2nd Risoe International Symposium on deformation of polycrystals mechanisms and microstructures.* 35-44.

[34] Humphreys, F. J. & Kalu, P. N. 1990 The plasticity of particle-containing polycrystals. *Acta Metall.* **38,** 917-930.

[35] Bay, B., Hansen, N., Hughes, D. A. & Kuhlmann-Wilsdorf, D. 1992 Overview No. 96 evolution of F.C.C. deformation structures in polyslip. *Acta Metall.* **40,** 205-219.

[36] Taylor, G. I. 1938 Plastic strain in metals. *J. Inst. Met.* **62,** 307-324.

[37] Malin, A. S. & Hatherly, M. 1979 Microstructure of cold-rolled copper. *Met. Sci.* **13,** 463-472.

[38] Hughes, D. A. & Hansen, N. 1991 Microstructural evolution in nickel during rolling and torsion. *Mater. Sci. Tech.* **7,** 544-553.

[39] Hansen, N. 1990 Cold deformation microstructures. *Mater. Sci. Tech.* **6,** 1039-1047.

[40] Bay, B. & Hansen, N. 1980 The deformation structure at grain boundaries in aluminum of commercial purity and in an aluminum-alumina alloy. *Proceeding of the 1st Risoe International Symposium on recrystallization and grain growth of multi-phase and particle containing materials.* 51-56.

[41] Bay, B. & Hansen, N. 1981 Microstructures in cold-rolled polycrystalline aluminum. *Proceeding of the 2nd Risoe International Symposium on deformation of polycrystals mechanisms and microstructures.* 137-144.

[42] Hansen, N. & Ralph, B. 1982 The strain and grain-size dependence of the follow-stress of copper. *Acta Metall.* **30,** 411-417.

[43] Kuhlmann-Wilsdorf, D. & Hansen, N. 1991 Geometrically necessary, incidental and subgrain boundaries. *Scripta Mater.* **25,** 1557-1562.

[44] Hughes, D. A. & Nix, W. D. 1989 Strain hardening and substructural evolution in Ni-Co Solid Solutions at Large Strains. *Mater. Sci. Eng. A* **122,** 153-172.

[45] Hughes, D. A. & Hansen, N. 1993 Microstructural evolution in nickel during rolling from intermediate to large strains. *Metall. Trans.* **24A,** 2021-2037.

[46] Rosen, G. I., Juul Jensen, D., Hughes, D. A. & Hansen, N. 1995 Microstructure and local crystallography of cold rolled aluminum. *Acta Metall.* **43,** 2563-2579.

[47] Liu, Q., Juul Jensen, D. & Hansen, N. 1998 Effect of grain orientation on deformation structure in cold-rolled polycrystalline aluminum. *Acta Metall.* **46,** 5819-5938.

[48] Pantleon, W. 2004 Stage IV work-hardening related to disorientations in dislocation structures. *Mater. Sci. Eng. A* **387-389,** 257-261.

[49] Hatherly, M. 1982 Deformation at high strains. *Proceeding of the 6th international conference on strength of metals and alloys.* 1181-1195.

[50] Hansen, N. & Mehl, R. F. 2001 New discoveries in deformed metals. *Metall. Mater. Trans. A* **32,** 2917-2935.

[51] Liu, Q., Huang, X., Lloyd, D. J. & Hansen, N. 2002 Microstructure and strength of commercial purity aluminum (AA 1200) cold-rolled to large strains. *Acta Mater.* **50,** 3789-3802.

[52] Hansen, N. & Kuhlmann-Wilsdorf, D. 1986 Low energy dislocation structures due to unidirectional deformation at low temperatures. *Mater. Sci. Eng.* **81,** 141-161.

[53] Kuhlmann-Wilsdorf, D. 1987 LEDS- properties and effects of low-energy dislocation-structures. *Mater. Sci. Eng.* **86,** 53-66.

[54] Nabarro, F. R. N. 1952 The mathematical theory of stationary dislocations. *Adv. Phys.* **1,** 269-394.

[55] Barlow, C. Y. & Hansen, N 1989 Deformation structures in aluminum containing small particles. *Acta Metall.* **37,** 1313-1320.

[56] Bay, B., Hansen, N. & Kuhlmann-Wilsdorf, D. 1992 Microstructural evolution in rolled aluminum. *Mater. Sci.* Eng. A **158,** 139-146.

[57] Hansen, N. & Huang, X. 1998 Microstructure and flow stress of polycrystals and single crystals. *Acta Mater.* **46,** 1827-1836.

[58] Huang, X. & Hansen N. 1997 Grain orientation dependence of microstructure in aluminum deformed in tension. *Scripta Mater.* **37,** 1-7.

[59] Winther, G., Huang, X. & Hansen, N. 2000 Crystallographic and macroscopic orientation of planar dislocation boundaries-correlation with grain orientation. *Acta Mater.* **48,** 2187-2198.

[60] Driver, J. H., Juul Jensen, D. & Hansen, N. 1994 Large strain deformation structures in aluminum crystals with rolling texture orientations. *Acta Metall.* **42,** 3105-3144.

[61] Buque, C., Holste, C. & Schwab, A. 1999 Orientation-dependent dislocation structure and cyclic plasticity of polycrystalline nickel. *Proceeding of the 20th Risoe International Symposium on deformation-induced microstructures: analysis and relation to properties.* 277-282.

[62] Huang, X. 1998 Grain orientation effect on microstructure in tensile strained copper. *Scripta Mater.* **38,** 1697-1703.

[63] Huang, X. & Winther, G. 2007 Dislocation structures. Part I. Grain orientation dependence. *Philos. Mag.* **87,** 5189-5214.

[64] Winther, G. & Huang, X. 2007 Dislocation structures. Part II. Slip system dependence. *Philos. Mag.* **87,** 5215-5235.

[65] Hansen, N., Huang, X. & Winther, G. 2011 Effect of grain boundaries and grain orientation on structure and properties. *Metall. Mater. Trans. A* **42A,** 613-625.

[66] Barlow, C. Y. J., Bay, B. & Hansen, N. 1985 A comparative investigation of surface relief structures and dislocation microstructures in cold-rolled aluminum. *Philos. Mag.* **51,** 253-275.

[67] Randle, V., Hansen, N. & Juul Jensen, D. 1996 The deformation behaviour of grain boundary regions polycrystalline aluminum. *Philos. Mag.* **73,** 265-282.

[68] Faivre, P. & Doherty, R. D. 1979 Nucleation of recrystallization in compressed aluminum-studies by electron-microscopy and kikuchi diffraction. *J. Mater. Sci.* **14,** 879-919.

[69] Ralph, B. & Hansen, N. 1981 Microstructural evidence of additive strengthening. Microstructures in cold-rolled polycrystalline aluminum. *Proceeding of the 2nd Risoe International Symposium on deformation of polycrystals mechanisms and microstructures.* 473-478.

[70] Kamma, C. & Hornbogen E. 1976 The effect of carbide particle size on the initiation of recrystallization of hypo-eutectoid steel. *J. Mater. Sci.* **11,** 2340-2344.

[71] Nourbakhsh, S. & Nutting, J. 1980 High-strain deformation of an aluminum-4-percent copper alloy in the supersaturated and aged conditions. *Acta Metall.* **28,** 357-365.

[72] Ashby, M. F. 1970 The deformation of plastically non-homogeneous Materials. *Phil. Mag.* **21,** 399-424.

[73] Humphreys, F. J. & Stewart, A. T. 1972 Dislocation generation at SiO2 particles in an α-brass matrix on plastic deformation. *Surf. Sci.* **31,** 389-421.

[74] Humphreys, F. J. & Ardakani, M. G. 1994 The deformation of particle-containing aluminum single crystals. *Acta metal.* **42,** 749-761.

[75] Ferry, M. & Humphreys, F. J. 1996 The deformation and recrystallization of particle-containing {011}<100> aluminum crystals. *Acta mater.* **44,** 3089-3103.

[76] Habiby, F. & Humphreys, F. J. 1994 The effect of particle stimulated nucleation on the recrystallization texture of an Al-Si alloy. **30,** 787-790.

[77] Engler, O., Kong, X. W. & Lucke, K. Development of microstructure and texture during rolling of single-phase and two-phase cube-oriented Al-Cu single crystals. *Scripta Mater.* **41,** 493-503.

[78] Engler, O., Kong, X. W. & Lucke, K. Influence of precipitates on the microstructure and texture during the rolling of Al-Cu and Al-Mn single crystals with rolling texture orientations. *Phil. Mag. A* **81,** 543-570.

[79] Humphreys, F. J. & Kalu, P. N. 1990 The plasticity of particle-containing polycrystals. *Acta Metall.* **38,** 917-930.

[80] Humphreys, F. J. 1979 Local lattice rotations at second phase particles in deformed metals. *Acta, Metall.* **27,** 1801-1814.

[81] Fleck, N. A., Muller, G. M., Ashby, M. F. & Hutchinson J. W. 1994 Strain gradient plasticity: theory and experiment. *Acta metal.* **42,** 475-487.

[82] Nix, W. D. & Gao, H. 1998 Indentation size effects in crystalline materials: A law for strain gradient plasticity. *J. Mech. Phys. Solids* **46,** 411-425.

[83] Swadener, J. G., George, E. P. & Pharr, G. M. 2002 The correlation of the indentation size effect measured with indenters of various shapes. *J. Mech. Phys. Solids* **50,** 681-694.

[84] Wang, Y., Raabe, D., Kluber, C. & Roters, F. 2004 Orientation dependence of nanoindentation pile-up patterns and of nanoindentation microtextures in copper single crystals. *Acta mater.* **52,** 2229-2238.

[85] Zaafarani, N., Raabe, D., Singh, R. N., Roters, F. & Zaefferer, S. 2006 Three-dimensional investigation of the texture and microstructure below a nanoindent in a Cu single crystal using 3D EBSD and crystal plasticity finite element simulations. *Acta Mater.* **54,** 1863-1876.

[86] Demir, E., Raabe, D., Zaafarani, N. & Zaefferer, S. 2009 Investigation of the indentation size effect through the measurement of the geometrically

necessary dislocations beneath small indents of different depths using EBSD tomography. *Acta Mater.* **57,** 559-569.

[87] Yang, W. *et al.* 2004 Differential-aperture X-ray structural microscopy: a submicron-resolution three-dimensional probe of local microstructure and strain. *Micron* **35,** 431-439.

[88] Rester, M., Motz, C. & Pippan, R. 2007 Microstructural investigation of the volume beneath nanoindentations in copper. *Acta Mater.* **55,** 6427-6435.

[89] Doherty, R. D. & Cahn, R. W. 1972 Nucleation of new grains in recrystallization of cold-worked metals. *J. Less-Common Met.* **28,** 279-296.

[90] Beck, P. A. & Sperry, P. R. 1950 Strain induced grain boundary migration in high purity aluminum. 21, 150-152.

[91] Bellier, S. P. & Doherty, R. D. 1977 The structure of deformed aluminum and its recrystallization-investigations with transmission Kossel diffraction. *Acta Metall.* **25,** 521-538.

[92] Bailey, J. E. & Hirsch, P. B. 1962 The recrystallization process in some polycrystalline metals. *Proc. Roy. Soc. A* **267,** 11-30.

[93] Beck, P. A. 1949 The formation of recrystallization nuclei. *J. Appl. Phys.* **20,** 633-634.

[94] Gleiter, H. 1969 The mechanism of grain boundary migration. *Acta Metall.* **17,** 565-573.

[95] Fujita, H. 1961 Direct observation of subgrain-growth of cold-worked aluminum by means of electron microscopy. *J. Phys. Soc. Jpn.* **16,** 397-406.

[96] Varma, S. K. & Willits, B. L. 1984 Subgrain growth in aluminum during static annealing. *Metall. Trans. A* **15A,** 1502-1503.

[97] Walter, J. L. & Koch, E. F. 1963 substructures and recrystallization of deformed (100) ｛001｝-oriented crystals of high-purity silicon-iron. *Acta Metall.* **11,** 923-940.

[98] Ferry, M. & Humphreys, F. J. 1996 Discontinuous subgrain growth in deformed and annealed (110) ｛001｝ aluminum single crystals. *Acta Mater.* **44,** 1293-1308.

[99] Huang, Y. & Humphreys, F. J. 2000 Subgrain growth and low angle boundary mobility in aluminum crystals of orientation (110) {001}. *Acta Mater.* **48,** 2017-2030.

[100] Huang, Y. & Humphreys, F. J. 2001 Measurements of subgrain growth in a single-phase aluminum alloy by high resolution EBSD. *Mater. Charact.* **47,** 235-240.

[101] Hu, H. 1962 Direct observations on the annealing of a Si-Fe crystal in the electron microscope. *Trans. Metall. Soc. AIME* **224,** 75-84.

[102] Bay, B. 1970 Subgrain growth on annealing of thin foil of cold-rolled aluminum. J. Mater. Sci. 5, 617-620.

[103] Estulin, G. V. & Demkin, Y. I. 1962 Recrystallization of molybdenum. *Met. Sci. Heat Treat.* **4,** 273-275.

[104] Jones, A. R., Ralph, B. & Hansen, N 1979 Subgrain coalescence and the nucleation of recrystallization at grain boundaries in aluminum. *Proc. R. Soc. Lond. A.* **368,** 345-357.

[105] Li, J. C. M. 1965 *Recrystallization, Grain Growth and Textures*. American Society for Metals, Metals Park, Ohio, 45-97.

[106] Kreisler, A. & Doherty, R. D. 1978 Structure of well-defined deformation bands and formation of recrystallization nuclei in aluminum. *Met. Sci.* **12,** 551-560.

[107] Doherty, R. D. 1978 Nucleation. In: Recrystallization of metallic materials (Eds. Hassner, F., Stuttgart: Riederer). 23-62.

[108] Burgers, W. G. & Louwerse, P. C. 1931 Uber den zusammenhang zwischen deformationsvorgang und rekristallisationstextur bei aluminum. *Zeitschrift fur physik.* **67,** 605-678.

[109] Ridha, A. A. & Hutchinson, W. B. Recrystallisation mechanisms and the origin of cube texture in copper. *Acta Metall.* **30,** 1929-1939.

[110] Duggan, B. J., Sindel, M., Kohlhoff, G. D. & Lucke, K. Oriented nucleation, oriented growth and twinning in cube texture formation. *Acta Metall.* **38,** 103-111.

[111] Inokuti, Y. & Doherty, R. D. 1977 Transmission kossel study of the structure of cold-rolled iron and its nucleation behavior. *Texture of crystalline solids* **2,** 143-168.

[112] Skjervold, S. R. & Ryum, N. 1996 Orientation relationships in a partially recrystallized polycrystalline Al-Si Alloy. *Acta Mater.* **44,** 3407-3419.

[113] Sabin, T. J., Winther, G. & Juul Jensen, D. 2003 Orientation relationships between recrystallization nuclei at triple junctions and deformed structures. *Acta Mater.* **51,** 3999-4011.

[114] West, S. S., Winther, G. & Juul Jensen, D. 2010 Analysis of Orientation Relations between Deformed Grains and Recrystallization Nuclei. Metall. *Mater. Trans. A* **42,** 1400-1408.

[115] Haasen, P. 1993 How are new orientations generated during primary recrystallization. *Metall. Trans. B* **24,** 225-239.

[116] Haasen, P. 1993 How are new orientations generated during primary recrystallization. *Metall. Trans. A* **24,** 1001-1015.

[117] Humphreys, F. J. & Ferry, M. 1996 On the role of twinning in the recrystallization of aluminum. *Scripta Mater.* **35,** 99-105.

[118] Field, D. P., Bradford, L. T., Nowell, M. M. & Lillo, T. M. 2007 The role of annealing twins during recrystallization of Cu. *Acta Mater.* **55,** 4233-4241.

[119] Berger, A., Wilbrandt, P. J., Ernst, F., Klement, U., Haasen, P. 1988 On the generation of new orientations during recrystallization: Recent results on the recrystallization of tensile-deformed fcc single crystals, *Prog. Mater. Sci.* **32,** 1-95.

[120] Gottstein, G. 1984 Annealing texture development by multiple by multiple twinning in fcc crystals, *Acta Metall.* **32,** 1117-1138.

[121] Humphreys, F. J., Ferry, M. Johnson, C. & Paillard, P. 1995 Particle-Stimulated nucleation-recent developments. Proceedings of the 16th Risø International Symposium on microstructural and crystallographic aspects of recrystallization. 87-104.

[122] Burke, J. E. & Turnbull, D. 1952 Recrystallization and grain growth. *Prog. Met. Phys.* **3,** 220-292.

[123] Bay, B. & Hansen, N. 1979 Initial stages of recrystallization in aluminum of commercial purity. *Metall. Trans. A.* **10A,** 279-288.

[124] Doherty, R. D. & Martin, J. W. 1963 Effect of a dispersed second phase on recrystallization of aluminum-copper alloys. *J. Inst. Met.* **91,** 332-338.

[125] Chopra, O. K. & Niessen, P. Recrystallization in internally oxidized Cu-Ag-Al alloys. *J. Mater. Sci.* **9,** 279-288.

[126] Sandstrom, R. 1977 Subgrain growth occurring by boundary migration. *Acta Metall.* **25,** 905-911.

[127] Hansen, N. 1975 Accelerated and delayed recrystallization in dispersion-hardened products. *Mem. Sci. Rev. Met.* **72,** 189-203.

[128] Granzer, F. & Haase, G. 1961 Elektronenmikroskopische untersuchungen zur keimbildung bei der rekristallisation. *Z. Phys.* **162,** 468-482.

[129] Cahn, R. W. 1949 Recrystallization of single crystals after plastic bending. *J. Inst. Met.* **76,** 121-143.

[130] Xie, G., Wang, L., Zhang, J. & Lou, L. H. 2012 Orientational dependence of recrystallization in an Ni-base single-crystal superalloy. *Scripta Mater.* **66,** 378-381.

[131] Zambaldi, C., Roters, F., Raabe, D. & Glatzel, U. 2007 Modeling and experiments on the indentation deformation and recrystallization of a single-crystal nickel-base superalloy. *Mater. Sci. Eng. A* **454-455,** 433-440.

[132] Humphreys, F. J. 2000 Particle stimulated nucleation of recrystallization at silica particles in nickel. *Scripta Mater.* **43,** 591-596.

[133] Jack. D. B., Koken, E. & Underhill, R. 1989 A study of induced recrystallization in an aluminum alloy using electron backscattered patterns. Proceeding of the 10th Risø International Symposium on materials architecture. 403-408.

[134] Ardakani, M. G. & Humphreys, F. J. 1994 The annealing behavior of deformed particle-containing aluminum single-crystals. *Acta Metall.* **42,** 763-780.

[135] Xu, C. L., Zhang, Y. B., Wu, G. L., Liu, Q. & Juul Jensen, D. 2015 Nucleation at hardness indentations in cold rolled Al. 36th Risoe International

Symposium on Effect of Deformation Induced Structural Variations on Annealing Mechanisms, *IOP Conf. Ser. Mater. Sci. Eng.* **89,** 012054.

[136] Inoko, F., Fujita, T. & Akizono, K. Recrystallization of aluminum bicrystals with a Pi-2 radian (211) twist grain boundary. *Scripta Metall.* **21,** 1399-1404.

[137] Inoko, F., Okada, T., Tagami, M. & Kashihara, K. 1999 Relation between deformed microstructures and <111> (FCC) and <011> (BCC) rotation recrystallization mechanisms. *Proceeding of the 20th Risø International Symposium on Materials Science: Deformation-induced microstructures: analysis and relation to properties*. 375-380.

[138] Driver, J. H., Paul, H., Glez, J-C. & Maurice, C. 2000 Relations between deformation substructure and nucleation in FCC crystals. *Proceeding of the 21st Risø International Symposium on recrystallization – fundamental aspects and relations to deformation microstructure*. 35-48.

[139] Huang, X., Wert, J. A., Poulsen, H. F., Krieger Lassen, N. C. & Inoko, F. 2000 Relations between deformation substructure and nucleation in FCC crystals. *Proceeding of the 21st Risø International Symposium on recrystallization – fundamental aspects and relations to deformation microstructure*. 359-370.

[140] Miszczyk, M., Paul, H., Driver, J.H. & Maurice C. 2015 new orientation formation and growth during primary recrystallization in stable single crystals of three face-centered cubic metals. *Acta Mater.* **83,** 120-136.

[141] Humphreys, F. J. 2004 Characterisation of fine-scale microstructures by electron backscatter diffraction (EBSD). *Scripta Mater.* **51,** 771-776.

[142] Dingley, D. 2004 Progressive steps in the development of electron backscatter diffraction and orientation imaging microscopy. *J. Micro.* **213,** 214-224.

[143] Chen, D., Kuo, J. C. & Wu, W. T. 2011 Effect of microscopic parameters on EBSD spatial resolution. *Ultramicroscopy,* **111,** 1488-1494.

[144] Day, A. P. *et al.* 2001 *Channel 5 User Mannual, HKL Technology A/S,* Denmark.

[145] Newbury, D. E. *et al.* 1986 Electron Channeling Contrast in the SEM. In: *Advanced scanning electron microscopy and X-ray Microanalysis* (Eds. Newbury, D. E. *et al.* Plenum Press, New York). 87-145.

[146] Schwab, A. *et al.* 1996 Application of electron channeling contrast to the investigation of strain localization effects in cyclically deformed fcc crystals. *Phil. Mag.*, **74,** 449-454.

[147] Ice, G. E. & Larson, B. C. 2000 3D x-ray crystal microscope. *Adv. Eng. Mater.* **2,** 643-646.

[148] Liu, W. *et al.* https://www1.aps.anl.gov/Sectors-33-34.

[149] Tishchler, J. Z. 2014 Reconstructing 2D and 3D X-ray orientation map from white beam Laue. In: *Strain and Dislocation Gradients from Diffraction* Ch. 10 (Eds. Barabash R. and Ice G. Imperial College Press, London).

[150] Mishin, O.V., Bay, B, Winther, G. & Juul Jensen, D. 2004 The effect of roll gap geometry on microstructure in cold-rolled aluminum. *Acta Mater.* **52,** 5761-5770.

[151] Godfrey, A., Cao, W. Q., Hansen, N. & Liu, Q. 2005 Stored energy, microstructure, and flow stress of deformed metals. *Metall. Mater. Trans. A* **36A.** 2371-2378.

[152] Godfrey, A., Mishin, O. V. & Yu, T. 2015 Characterization and influence of deformation microstructure heterogeneity on recrystallization. 36th Risø International Symposium on effects of deformation induced structural variations on annealing mechanisms, *IOP Conf. Ser. Mater. Sci. Eng.* **89,** 012003.

[153] Schmidt, S. *et al.* 2004 Watching the growth of bulk grains during recrystallization of deformed metals. *Science* **305,** 229-232.

[154] Juul Jensen, D. 1995 Growth rates and misorientation relationships between growing nuclei/grains and the surrounding deformed matrix during recrystallization. *Acta Metall.* **43,** 4117-4129.

DTU Vindenergi er et institut under Danmarks Tekniske Universitet med en unik integration af forskning, uddannelse, innovation og offentlige/private konsulentopgaver inden for vindenergi. Vores aktiviteter bidrager til nye muligheder og teknologier inden for udnyttelse af vindenergi, både globalt og nationalt. Forskningen har fokus på specifikke tekniske og videnskabelige områder, der er centrale for udvikling, innovation og brug af vindenergi, og som danner grundlaget for højt kvalificerede uddannelser på universitetet.

Vi har mere end 240 ansatte og heraf er ca. 60 ph.d. studerende. Forskningen tager udgangspunkt i ni forskningsprogrammer, der er organiseret i tre hovedgrupper: vindenergisystemer, vindmølleteknologi og grundlag for vindenergi.

Danmarks Tekniske Universitet
DTU Vindenergi
Nils Koppels Allé
Bygning 403
2800 Kgs. Lyngby
Telefon 45 25 25 25

info@vindenergi.dtu.dk
www.vindenergi.dtu.dk